2021
Volume 4
Issue 1
ISSN: 2578-2010

APPLIED CHEMICAL ENGINEERING

Volume 4 Issue 1 https://systems.enpress-publisher.com/index.php/ACE

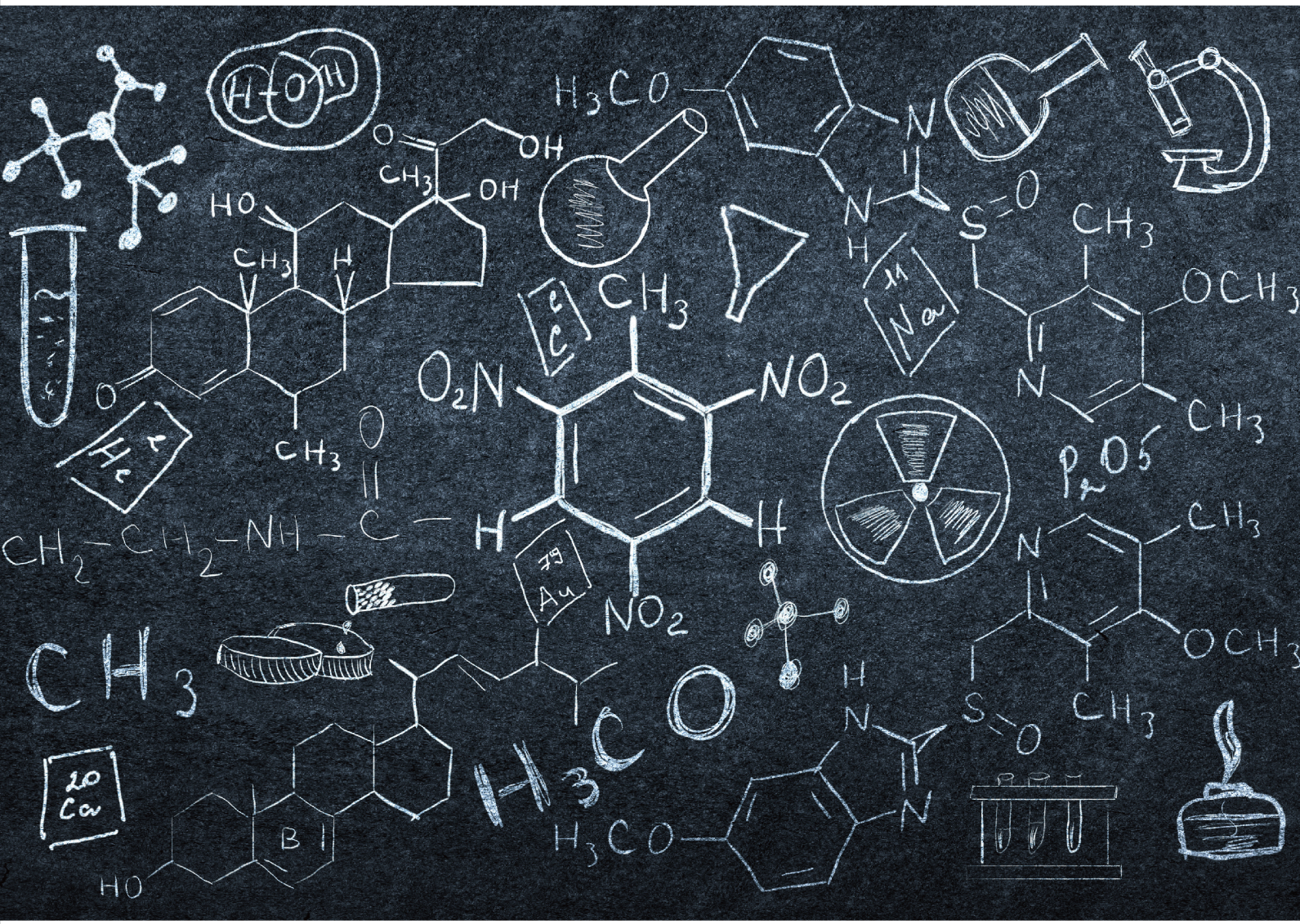

ISSN 2578-2010

ACE

EnPress Publisher

Editorial Board

Editor-in-Chief

Associate Editor

Editorial Board Member

Volume 4 Issue 1 • 2021

Applied Chemical Engineering

EnPress Publisher

2021 | Volume 4 | Issue 1

Applied Chemical Engineering

https://systems.enpress-publisher.com/index.php/ACE

Contents

Original Research Article

1 **Optimization of electrodialysis unit for partial desalination: Batch and continuous operation**
H. M. Abdel-Ghafar, E. A. Abdel-Aal, D. El-Sayed, J. Hoinkis

9 **Study on the physical properties of Cu_2ZnSnS_4 thin films deposited by pneumatic spray pyrolysis technique**
Maykel Courel, Miriam M. Nicolás, Osvaldo Vigil-Galán

15 **Optimization of oscillated gas-liquid separator for simultaneous heavy metals determination in water sample**
Wameath S. Abdul-Majeed

23 **The role of dysprosium ions as a dopant on linear and nonlinear optical dispersion parameters in a-Se thin film**
Fathy A. Abdel-Wahab, Heba Abdel Maksoud

33 **Synthesis and characterization of polyurethane and its nanocomposite adhesive derived from biobased isocyanate and polyol**
Swarnalata Sahoo, Smita Mohanty, Sanjay Kumar Nayak

41 **Polyaniline modified silica gel coupled with green solvent as eco favourable mobile phase in thin layer chromatographic analysis of organic dyes**
Mahfoozurrahman Khan, Ali Mohammad, Qasim Ullah, Faiz Mohammad

Applied Chemical Engineering (2021) Volume 4 Issue 1
doi: 10.24294/ace.v4i1.479

ORIGINAL RESEARCH ARTICLE

Optimization of electrodialysis unit for partial desalination: Batch and continuous operation

H. M. Abdel-Ghafar[1*], E. A. Abdel-Aal[1], D. El-Sayed[1], J. Hoinkis[2]

[1] *Central Metallurgical Research and Development Institute (CMRDI), Cairo, Egypt. E-mail: hamdy.maamoun@yahoo.com*

[2] *Karlsruhe University of Applied Sciences (HSKA), Germany*

ABSTRACT

In recently few years, application of membrane technologies in sea water desalination is increased compared to other desalination technologies. Electrodialysis membrane technology is still limited in seawater desalination due to the high operation cost and its limitations for high salty water. Electrodialysis desalination cost is proportional to the amount of salt, which must be carried out through the membrane. Seawater desalination with high salt content of NaCl (42 g/L) was applied using IonTech electrodialysis unit. Partial desalination process was studied in two separate experiments, batch and continuous operation. Operation parameters like voltage applied, electrolyte concentration and time of desalination were studied under batch mode process. Continuous operation process was carried out to confirm the partial desalination process of electrodialysis. The limited current density is determined, 1.49 A/m^2 and 1.15 A/m^2 for theoretical and experimental, respectively. The specific energy consumption was calculated, 7.15 kWh/m^3.

Keywords: Electrodialysis; Partial Desalination; Potential Difference; Energy Consumption

ARTICLE INFO

Received: 10 February 2021
Accepted: 30 March 2021
Available online: 7 April 2021

1. Introduction

Scarcity of utilizable fresh water is obstacle for most countries around the world. Therefore, some special processes are needed to desalinate salty water of the oceans and seas[1]. Suitable desalinating methods for water treatment of seawater can be effective to overcome the fresh water scarcity. Electrodialysis (ED) is one of these methods which have been used for many years. The basic principles of ED have been reviewed in the literature[2].

Seawater desalination using electrodialysis was studied by Sadrzadeh and Mohammadi[3]. To evaluate effects of operation parameters, a L9 orthogonal array (four factors in three levels) was employed. Temperature, voltage applied, flow rate and feed concentration effects on separation percentage of ions have been studied. Maximum percentage of salts removal was obtained at the highest voltage applied (9 V), lowest feed concentration (10 g/L), high temperature level (55 °C) and lowest flow rate level (0.07 mL/s). It was found that, feed concentration is the most influential factor on ED performance (its contribution percentage was calculated to be 82.4%)[3].

The desalination efficiency of an electrodialysis unit is dependent on variable and fixed parameters. These variable and fixed parameters are like applied voltage, feed and permeate concentration, type and concentration of electrolyte, flow rate, ED stack construction, current density, membrane permselectivity and recovery rates[4]. For highly efficient

operation conditions of electrodialysis, the process has to be optimized in terms of overall costs considering operating parameters, component design and properties[4].

Electrodialysis offers the high practical advantage of much higher recovery in many applications due to the lowest quantity of dissolved species in the feed stream than the fluid[5-10]. The efficiency of electrodialysis recovery depends on the ionic solids and fouling potential from organics and particles in the feed water[11,12].

Current efficiency in ED is a measure of how effective ions are transported across the ion exchange membranes for a given applied current. Typically, in commercial stack membranes, current efficiencies higher than 80% are desirable to minimize energy operating costs. Low current efficiencies indicate water splitting in the dilute or concentrate streams, shunt currents between the electrodes, or back-diffusion of ions from the concentrate to the dilute could be occurring[11].

The most application of electrodialysis has historically been the desalination of brackish water as an alternative to RO for potable water production and seawater concentration for salt production (primarily in Japan)[7].

Galama *et al*.[13] study the suitability of ED for seawater desalination and energy losses has been quantified. They found that, combining ED with BWRO in a hybrid system does not lead to a reduction in energy consumption compared to ED as standalone technique, when the applied current density becomes lower than 50 A/m^2. At low applied current density (10 A/m^2), ED can perform desalination energetically cheaper at lower operational costs than SWRO.

The combination of electrodialysis (ED) and brackish water reverse osmosis (BWRO) is presented as a promising and economic desalination strategy that could lead to a desalination cost reduction compared to seawater reverse osmosis (SWRO)[14]. Water recoveries for seawater desalination using ED were reported from 50 to 60 %[15,16] and with ED reversal, it is expected higher water recoveries can be obtained[17].

This study aims to evaluate the facilities of partial desalination for sea water using a pilot scale of electrodialysis system with low energy consumption. Optimum operation conditions of electrodialysis system were determined with operation in batch and continuous mode. Limiting current density and energy consumption for the electrodialysis system were determined.

2. Experimental procedure

2.1 Materials

A commercial salt (sodium chloride supplied by Al-Malahat Egyptian Company) was used in all experiments to produce a simulated solution of sea water qualities. The purpose of these was to study the effects of voltage, flow rate and feed concentration on ED pilot scale in batch and continuous mode.

2.2 Electrodialysis system

A pilot scale of electrodialysis unit (ION-LYZER-40-2040, IONTECH Co., China) was supplied and used in this work as shown in **Figure 1**. It contains three compartments, compartment 1 containing 10 L of untreated feed water (dilute), compartment 2 containing 10 L of saline solution of known concentration (electrolyte) and compartment 3 containing 10 L of sea water (concentrate). **Table 1** shows the specifications and operation conditions of electrodialysis unit.

Table 1. Specifications and operation conditions of electrodialysis unit

Item	Specifications
ED stack	40 IONSEP-HC (20*40 cm） 40 pairs of IONSEP-HC/MC membrane and spacer in the size of 20*40 cm; noble metal electrode; fasteners
IGBT high frequency Switching power supply	DC Output 50V, 10A, AC Input 220V,50/60HZ
Magnetic transfer pumps	Q = 1.2 m^3/h, Head = 5 m
Electrode water pump	Q = 1.2 m^3/h, Head = 5 m
Storage Tanks	Electrode, feed and dilute water tank
Pressure Gauges	Oil-filled
Flow rate for concentrated & diluted solutions	300–600 L/h
Flow rate for electrode solution	100–300 L/h

For ED batch mode operation, 10 L from the feed water source of ED is placed in the dilute

compartment for the desired electrodialysis time interval at the required potential difference. Conductivity (µS/cm), TDS (mg/L) and salinity were measured instantly during desalination process using HANA Electrod.

For ED continuous operation mode, two external transfer feed pumps were used, one for diluted stream and the other for concentrated stream.

Table 2. Iontech membrane parameters

Conditions	Data
Membrane area (per sheet)	20*40 cm^2
Number of cell pair	40
Width (between anion and cation exchange membrane)	0.8 mm
Surface membrane resistance	5.5 Ωcm^2

Figure 1. Electrodialysis unit (IONLYZER-40-2040, IONTECH Co., China).

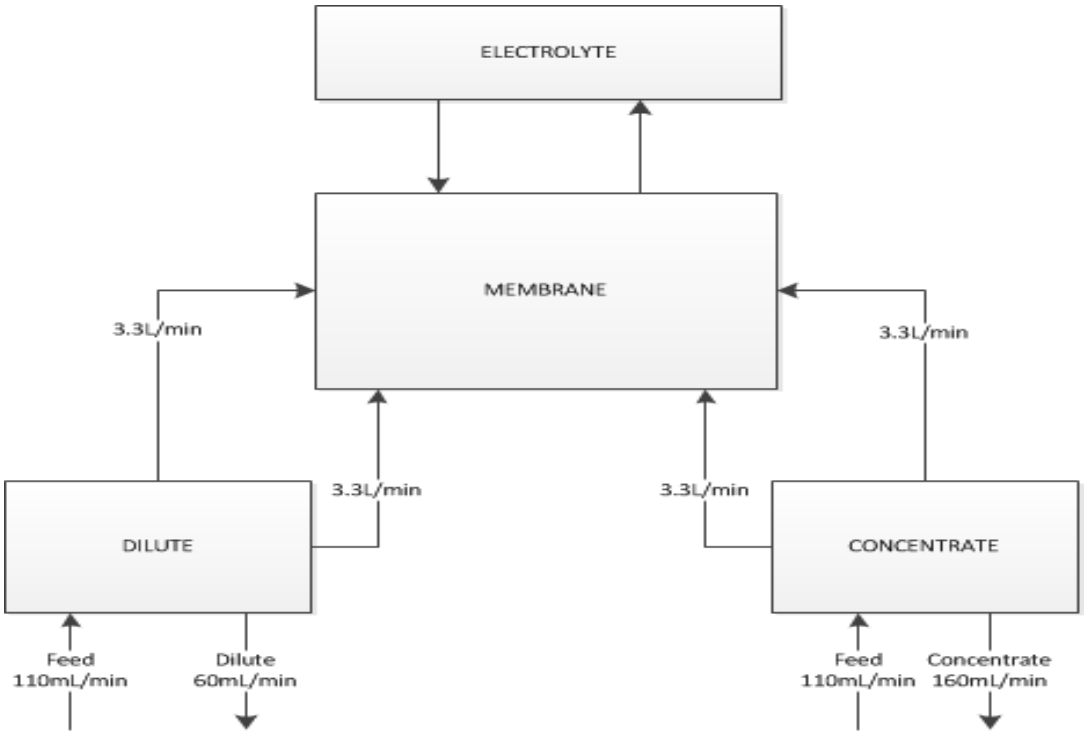

Figure 2. Schematic diagram of continuous operation mode.

The external feed pumps were set at constant feed flow rate with the same of discharged outlet with continuous circulation of electrodialysis pumps (diluted, concentrated and electrolyte). The difference in diluted and concentrated discharge is due to high polarization on ED membranes. A schematic diagram of the continuous operation mode was shown in **Figure 2**.

2.3 Analytical methods

Concentration of NaCl in the dilute and concentrate compartments was measured at various operating conditions. In all experiments, a conductivity-meter (HANA-HI 2550) was used to measure the amount of salts as Total Dissolved Salts (TDS) and conductivity in water. Water conductivity directly depends on its salt content.

2.4 Procedure

In this study, desalination efficiency of ED operation in batch and continuous mode was determined by measuring of conductivity, TDS and salinity. The quality characteristic was TDS Removal Efficiency (%) which was calculated as follow:

$$Removal\ Effecieny, \% = \frac{C_o - C}{C_o} \times 100 \qquad (1)$$

where C_0 and C are feed and dilute concentrations (mg/L), respectively.

3. Results and discussion

3.1 Batch mode operation

A synthetic solution of commercial sodium chloride salt—supplied from Al-Malahat Egyptian Company—was prepared with concentration 42 g/L. The prepared synthetic solutions were simulated to Red Sea water sample. Different parameters of electrodialysis unit operation were studied for optimize batch mode operation conditions. Applied voltage, electrolyte type and concentration, retention time, circulation rate and removal efficiency have been studied.

3.1.1 Effect of applied potential difference

A series of experiments was carried out at different applied potential differences ranged from 6.0 to 18.0 volt to determine ions removal efficiency. The following conditions are kept constant as: total electrodialysis time was 60 min, type of electrolyte was sodium chloride (NaCl) and concentration of electrolyte was 0.5 M.

The effect of potential difference and time on Removal Efficiency of Red Sea water sample was studied. The obtained results are given in **Figure 3**. High TDS removal efficiency was achieved with applying 15 V potential differences. The results reveal that, with increase in the applied potential difference, conductivity values decrease with time which means high salts removal efficiency. Decreasing of TDS (mg/L) means high salts removal efficiency. The best (optimum) applied potential difference is 15.0 volt.

3.1.2 Effect of electrolyte concentration

A series of experiments was carried out at different electrolyte concentrations ranged from 0.1 M to 0.7 M of NaCl solutions to determine ions removal efficiency. The following conditions are kept constant as: potential difference was 15 Volt, total electrodialysis time was 60 min and type of electrolyte was Sodium chloride (NaCl).

The obtained results are given in **Figure 4**. It was concluded that, with increase in electrolyte concentration, low conductivity values obtained (high removal efficiency). The difference in the concentration values with respect to removal efficiency is sharp in case of Red Sea water as it contains high salinity. From these results, it was concluded that the best electrolyte concentration is 0.5 M NaCl solution at the applied conditions. Choose sodium chloride to be the electrolyte for ED, because it is a cheap source for electrolyte operation.

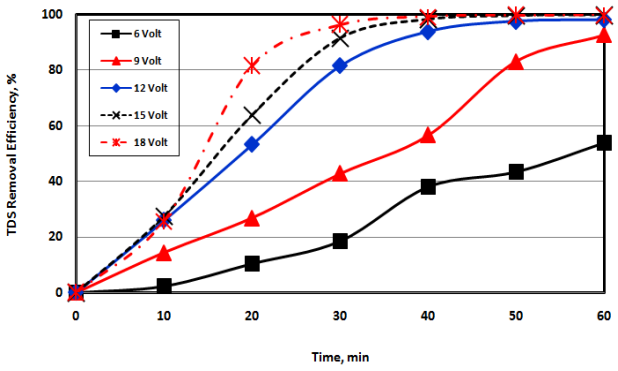

Figure 3. Effect of potential difference and time on TDS removal efficiency.

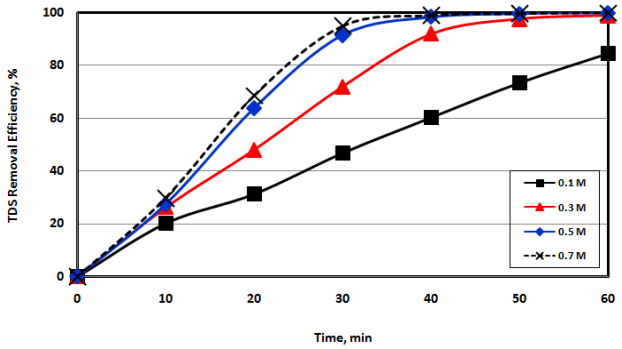

Figure 4. Effect of NaCl electrolyte concentration and time on TDS removal efficiency.

3.1.3 Effect of electrodialysis time on chloride concentration

The behaviour of each ion most probably follows that of Total Dissolved Salts (TDS). Chlorides ions were taken as an example of ions removed during electrodialysis as they are the major ions in the Red Sea water composition. The obtained results are given in **Figure 5**. The applied potential difference is 15 Volt and 0.5 M sodium chloride electrolyte concentration. The results reveal that, chloride ions have a removal efficiency (RE) of about 92% in the first 20 minutes. The achieved chloride ions removal efficiency was almost constant at about 99.7% ± 0.1% after about 30 minutes.

From the previous work, the best operating conditions for electrodialysis unit with batch mode were concluded and represented in **Table 3**.

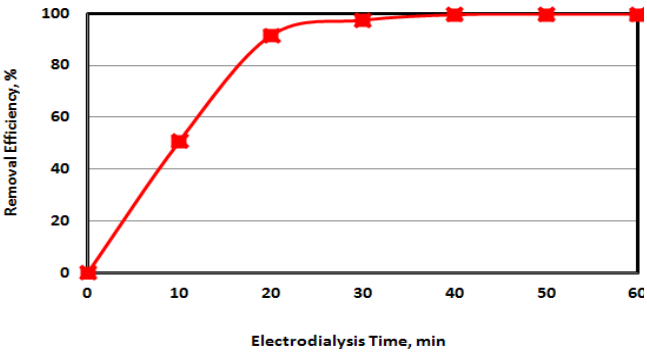

Figure 5. Effect of electrodialysis time on chloride removal efficiency.

TDS and current passed were plotted as a function of time at the optimum operation conditions as shown in **Figure 6**.

3.1.4 Morphology analysis

A sample from concentrated stream of the Electrodialysis was taken (highly concentrated) and evaporated till dryness. Then the precipitate was characterized and analyzed using SEM and EDX. The obtained results are shown in **Figure 7** and **Figure 8** and **Table 4**. **Figure 7** shows that the crystallized solids have needle-like shape with length of about 3 to 5 Microns and width of 0.1 to 0.3 Microns. In addition, **Figure 8** shows the EDX analysis of the precipitated solids. It shows that chloride ions are the main anions. Divalent cations like Mg^{2+} and Ca^{2+} have low contents compared with monovalent cations such as Na^{+} and K^{+}.

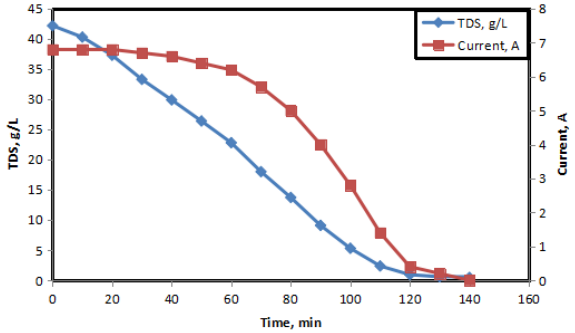

Figure 6. TDS (g/L) and current (A) as a function of time at optimum operation conditions.

Table 3. Optimum operating conditions of ED system with batch mode for sea water sample

Parameters	Value
Applied potential difference, Volt	15
Electrodialysis retention time, min	30
Type of electrolyte	Sodium chloride
Electrolyte concentration, M	0.5
Flow rate of electrolyte, L/min	6.6 (Fully opened)
Flow rate of diluted and concentrated streams, L/min	3.3

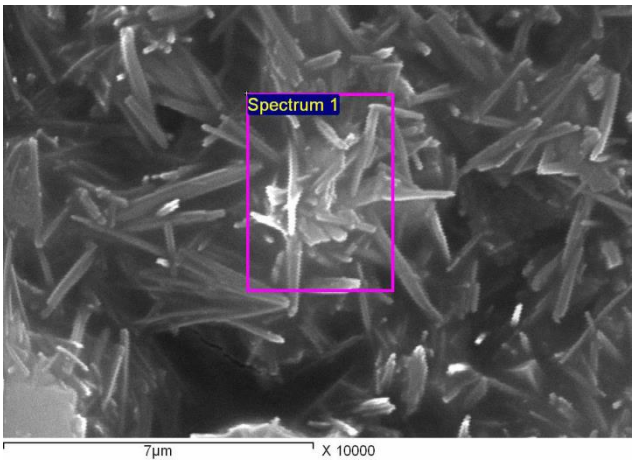

Figure 7. SEM photomicrograph of crystallized salts from electrodialysis.

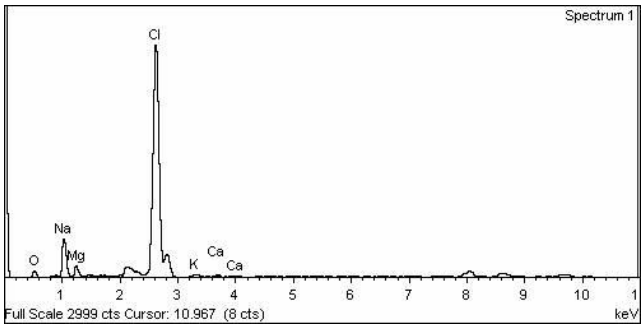

Figure 8. EDX analysis of crystallized salts from electrodialysis concentrated stream.

Table 4. EDX analysis of crystallized salts from concentrated sea water

Ions	Weight (%)
Cl^-	53.5
O^{2-}	21.1
Na^+	18.9
Mg^{2+}	5.1
K^+	0.8
Ca^{2+}	0.6
Total	100.0

3.1.5 Limiting current density

The limiting current density, i_{lim}, can be determined theoretically according to the following equation[6]:

$$i_{lim} = k\frac{CzF}{T_m - T_s} \quad (2)$$

where, C is the concentration of the diluate, z the electrochemical valence of the ions in the solution, F Faraday constant, T_m and T_s the ion transport numbers in the membrane and the solution, respectively. The coefficient k in the equation is the mass transfer coefficient, representing the influence of the hydrodynamics, flow channel geometry, spacer design, etc. Limiting current density is proportional to the ion concentration in the diluate and the mass transfer coefficient, which are related to the cell geometry and the feed solution flow velocity[6].

According to this relationship, the limiting current density can be calculated as follow:

$$i_{lim} = 1.55 \times 10^{-5}\frac{0.5\times1\times96487}{0.95-0.45} \quad (3)$$

So, i_{lim} = 1.49 A/m^2.

The limiting current density can be determined from the relationship between the current and corresponding potential, or from the measurement of the cell resistance and the pH value in the diluate cell as a function of the current density[6–18].

In this study the limiting current was determined by measuring the potential and the cell resistance as a function of the applied current. **Figure 9** shows the curve used for the determination of the limiting current from the experimental result obtained with a batch mode operation. The started dilute solution used was 42 g/L of NaCl and the concentration of the electrolyte was 0.5 M of NaCl with a linear feed velocity 6.6 L/min. From the curve in **Figure 9**, the experimental limiting current density was 1.15 A/m^2.

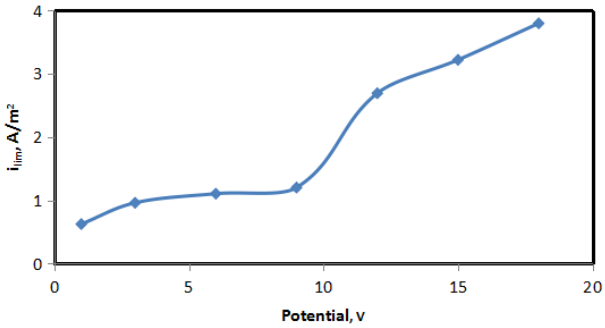

Figure 9. Current-voltage curve for the determination of limiting current density.

3.1.6 Energy consumption

In this work, partial desalination using electrodialysis was applied, started with feed solution concentration 42 g/L and desalinated water 4 g/L with desalination efficiency 91%. Power and energy consumption for this pre-desalination step was calculated according to the following equations:

$$I = i_{lim} \times A \quad (4)$$

$$P = I^2 \times R \quad (5)$$

$$E_{spec.} = \frac{P}{Flow} \quad (6)$$

where, i_{lim} is the experimental limiting current density (1.15 A/m^2), A is the total effective membrane area of ED stack (2.08 m^2), I is the total applied current (A), R is the membrane resistance (5.5 Ω/cm^2) and flow is the dilute electrodialysis stream flow (4.4 × 10^{-3} m^3/h). The calculated power consumption, P was 13.38 W and the calculated specific energy consumption, $E_{spec.}$ was 7.15 kWh/m^3. The results of this work is promising, according to W.S. Walker *et al.*[19], the specific energy consumption is proportional to the applied voltage and the ionic concentration that is separated. So, for treatment of a concentrate solution of 15000 mg/L at a moderate voltage applications (e.g., 1.0 V/cell-pair), the specific energy consumption of ED would be approximately 7.0

kWh/m^3 (including electric and hydraulic energy consumption), which is less than many thermal desalination alternatives (e.g., 20-30 kW h/m^3).

In this work study case, the specific energy consumption was7.15 kW h/m^3, which is comparable with the total energy consumption estimated for industrial plant was equal to 6.8–8.7 kW h/m^3 of desalinated water[20].

3.2 Continuous mode operation

In the following, the main operating conditions and the results of the use of ED as an applied technique for ions removal from Red Sea water is given. A schematic diagram of the continuous operation mode was shown in **Figure 2**. In the beginning, the ED conditions are operated batch wise under the following conditions: potential difference was 15 Volt, TDS of Red Sea water sample was 42000 ppm, type of electrolyte was Sodium chloride (NaCl) and electrolyte concentration was 0.5 M.

The obtained results are given in **Figure 10**. The results reveal that, with increase in electrodialysis time, the conductivity values decreased. This means the removal efficiency of salts is increased. From these results, it was concluded that the best electrodialysis retention time for the continuous batch mode operation is 105 minutes that gives the required TDS from 3.84 g/L for the Dilute solution and 64.9 g/L for the Concentrate solution.

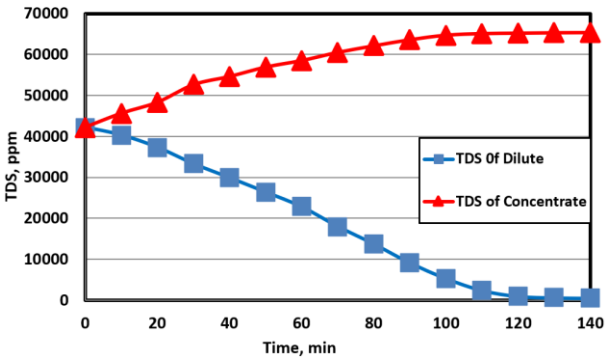

Figure 10. Effect of time on TDS of dilute and concentrate of ED.

Based on the previous test and using 105 minutes as the best retention time, the continuous preliminary feeding and discharge rates are calculated. The optimum operating conditions for electrodialysis unit with a continuous mode are represented in **Table 5**.

Table 5. The optimum operating conditions for electrodialysis unit with a continuous mode

Parameters	Value
Applied potential difference, Volt	15
Electrodialysis retention time, min	105
Type of electrolyte	NaCl
Electrolyte concentration, M	0.5
Flow rate of electrolyte, L/min (circulation)	6.6 (Fully opened)
Flow rate of diluted stream, L/min (circulation)	3.3
Flow rate of concentrated stream, L/min (circulation)	3.3
Initial feeding rate of saline water to Dilute tank, ml/min	110
Initial feeding rate of saline water to Concentrate tank, ml/min	110
Initial discharging rate of produced water from Dilute tank, ml/min	60
Initial discharging rate of saline water from Concentrate tank, ml/min	160
Initial feeding rate of saline water to Dilute tank, ml/min	110
Initial feeding rate of saline water to Concentrate tank, ml/min	110

4. Conclusion

The following parameters were studied using Electrodialysis system with determination of removal efficiency: concentration of saline water, retention time, applied voltage, concentration of sodium chloride electrolyte.

The optimum Electrodialysis parameters of batch mode were determined as 15 Volt applied potential difference, 30 minutes retention time with circulation. 0.5 M sodium chloride as electrolyte solution. The produced water was fed to Reverse Osmosis system. The tests are still continuing. Moreover, salts after evaporation of concentrated solution of Electrodialysis system were characterized and chemically analyzed.

The limited current density is determined, 1.49 A/m^2 and 1.15 A/m^2 for theoretical and experimental, respectively. The specific energy consumption was calculated, 7.15 kWh/m^3.

Conflict of interest

The authors declare that they have no conflict of interest.

Acknowledgements

The authors would like to acknowledge the Science and Technology Development Fund (STDF), Egypt for granting the fund of the Project ID: 5085 under the Program of GERF. The Project Title is: Development of Water Desalination using Hybrid System.

References

1. Mohammadi T, Kaviani A. Water shortage and seawater desalination by electrodialysis. Desalination 2003; 158: 267–270.
2. Winston Ho WS, Sirkar KK. Membrane handbook. Champan & Hall; 1992.
3. Sadrzadeh M, Mohammadi T. Seawater desalination using electrodialysis. Desalination 2008; 221: 440–447.
4. Lee H, Sarfert F, Strathmann H. Designing of an electrodialysis desalination plant. Desalination 2002; 142: 267–286.
5. Davis TA. Electrodialysis. In: Porter MC (editors). Handbook of industrial membrane technology. NJ: Noyes Publications; 1990.
6. Strathmann H. Electrodialysis. In: Winston Ho WS, Sirkar KK (editors). Membrane handbook. NY: Van Nostrand Reinhold; 1992.
7. Mulder M. Basic principles of membrane Technology. Kluwer, Dordrecht; 1996.
8. Sata T. Ion Exchange Membranes: Preparation, Characterization, Modification and Application. London: Royal Society of Chemistry; 2004.
9. Strathmann H. Ion-Exchange membrane separation processes. NY: Elsevier; 2004.
10. http://cape.uwaterloo.ca/che100projects/sea/ed.html.
11. American Water Works Association. Electrodialysis and electrodialysis reversal. American Water Works Association, Denver; 1995.
12. Shaffer L, Mintz M. Electrodialysis. In: Spiegler K, Laird A (editors). Principles of Desalination. 2nd ed. NY: Academic Pres; 1980.
13. Galama AH, Saakes M, Bruning H, *et al*. Seawater pre-desalination with electrodialysis. Desalination 2014; 342: 61–69.
14. Post JW, Huiting H, Cornelissen ER, *et al*. Pre-desalination with electro-membranes for SWRO. Desalination. Water Treat 2011; 31: 296–304.
15. Thampy SK, Narayanan PK, Harkare WP. Seawater desalination by electrodialysis. Part II: A novel approach to combat scaling in seawater desalination by electrodialysis. Desalination 1988; 69: 261–273.
16. Seto T, Ehara L, Komori R, *et al*. Seawater desalination by electrodialysis. Desalination 1978; 25: 1–7.
17. Allison RP. High water recovery with electrodialysis reversal. AWWA Membrane Technology Conference Proceedings, Baltimore, MD (USA); 1993. p. 665–673.
18. Choi JH, Lee HJ, Moon SH. Effects of electrolytes on the transport phenomena in a cation-exchange membrane. Journal of Colloid and Interface Science 2001; 238: 188–195.
19. Walker WS, Kim Y, Lawler DF. Treatment of model in land brackish groundwater reverse osmosis concentrate with electrodialysis—Part II: Sensitivity to voltage application and membranes. Desalination 2014; 345: 128–135.
20. Turek M. Cost effective electrodialytic seawater desalination. Desalination 2002; 153: 371–376.

Applied Chemical Engineering (2021) Volume 4 Issue 1
doi:10.24294/ace.v4i1.652

ORIGINAL RESEARCH ARTICLE

Study on the physical properties of Cu_2ZnSnS_4 thin films deposited by pneumatic spray pyrolysis technique

Maykel Courel[1*], Miriam M. Nicolás[2], Osvaldo Vigil-Galán[1]

[1] *Instituto de Energías Renovables, Universidad Nacional Autónoma de México, Temixco, Morelos 62580, Mexico.*
E-mail: maykelcourel@gmail.com

[2] *Escuela Superior de Física y Matemáticas-Instituto Politécnico Nacional (IPN), C.P. 07738, CDMX, México*

ABSTRACT

The acquisition of new materials for the manufacturing of high efficiency and low-cost photovoltaic devices has currently become a challenge. Thin films of CuInGaSe and CdTe have been widely used in solar cell of second generation, achieving efficiencies about 20 %; however, the low abundance of In and Te as well as the toxicity of Cd is the primary obstacles to their industrial production. Compounds such as Cu_2ZnSnS_4, $Cu_2ZnSnSe_4$ and $Cu_2ZnSn(SSe)_4$ have emerged as an important and less costly alternative for efficient energy conversion in the future. In addition, these compounds have the required characteristics to be used as an absorber material in solar cells (band-gap close to 1.4 eV, an absorption coefficient greater than 10^4 cm^{-1} and a p-type conductivity). In this work, we present a study of the structural, compositional, morphological and optical properties of Cu_2ZnSnS_4 thin films deposited by spray pyrolysis technique as well as their dependence on temperature.

Keywords: CZTS; Thin Films; Solar Cells; Structural; Morphological; Compositional and Optical Properties

ARTICLE INFO

Received: 6 March 2021
Accepted: 20 April 2021
Available online: 27 April 2021

1. Introduction

Currently, solar cells have not yet been able to replace fossil fuels. To obtain a greater contribution of photovoltaic energy in the energy market, it is necessary to reduce production costs as well as increase the efficiency of the cells. Within the field of photovoltaics, solar cells of second generation have reduced production costs. Among the most used materials, CdTe and CuInGaSe have been able to achieve efficiencies greater than 18%[1]. However, the shortage of In and Te and the high toxicity of Cd have been major obstacles to industrial production. For this reason, it is necessary to search for new materials with adequate physical properties for their application in photovoltaics. An alternative that has been studied is the kesterite compound Cu_2ZnSnS_4 (CZTS), which meets the requirements to be used as an absorber, that is, a band gap of 1.4 eV, p-type conductivity, in addition to having an absorption coefficient greater than 10^4 cm^{-1}[2–6].

Different deposition techniques have been considered to CZTS thin films deposition for solar cells application. In particular, thermal evaporateion[7], co-evaporation[8], magnetron sputtering[9,10], screen printed[11], sol gel[12], electrodeposition[13], photochemical deposition[14], and spray pyrolysis[15–20] are among the most used ones. These techniques offer an easy and cheap route for thin film processing. Particularly, spray pyrolysis constitutes an easy, economical and versatile technique which is potentially attractive to reduce cost of solar cell

processing. In regardless of the deposition method used to obtain the kesterite, it has been shown that film compositions must meet certain non-stoichiometric conditions to achieve high efficiencies in cells (Cu/(Zn+Sn) ≈ 0.85 and Zn/Sn ≈ 1.25)[21]. Therefore, this consideration must be taken into account for the deposition of the films.

In this work, a study of the dependence of the structural, morphological and optical properties of CZTS thin films deposited by the chemical spray pyrolysis method as a function of temperature is presented. In addition, the relationship of these properties with the Cu/(Zn+Sn) and Zn/Sn compositional ratios will be presented.

2. Experimental details

CZTS films were deposited by the chemical spray pyrolysis method. The method consists of mixing different reagents in a solution and then spraying it. The substrate is placed on heated plate where the reaction is carried out. The temperature of the heated plate is controlled by a thermocouple. Once the substrate is heated, the solution is sprayed with the help of a compressor using air as carrier gas. The temperature of the substrate stands out as one of the most important parameters to be taken into account.

2.1 Solution preparation

For the deposition of CZTS films by means of the chemical spray pyrolysis technique, the precursor salts $(CH_3COO)_2Zn$ * $2H_2O$, $CuCl_2$, $SnCl_4$ * H_2O and thiourea were considered. All the salts are dissolved in 50 ml of deionized water. The masses of the salts to be diluted were calculated to obtain the optimal composition ratios[21], resulting: 132.8 mg of Cu, 107.6 mg of Zn, 87.9 mg of Sn and 134.7 mg of S. 50% of the solution is extracted of each salt, adding 100ml of deionized water, obtaining in this way a 200ml solution, which is the one used for the deposition.

2.2 Thin film deposition

A flow rate of 5 ml/min, a pressure of 10 Psi, with a separation distance between the nozzle and the substrate of approximately 30 cm and a temperature range of 400–440 °C were considered. More specifically, we worked with 400 °C, 420 °C and 440 °C. All films were deposited under the same growth conditions mentioned above, with a deposition time of 20 minutes for each sample.

2.3 Characterization

CZTS thin films processed by spray pyrolysis were submitted to the following characterizations: X-ray diffraction (X'PertPRO-MRD (PW3050/65) diffractometer from Panalytical using CoKα radiation), Transmittance (Lambda 35 UV/VIS Perkin–Elmer) and SEM and EDS by Jeol JSM-7800F with an accelerating voltage of 30 keV. By means of these characterizations, it is possible to find the type of structure, the atomic composition as well as the band gap.

3. Results

3.1 X-RAY Diffraction Results

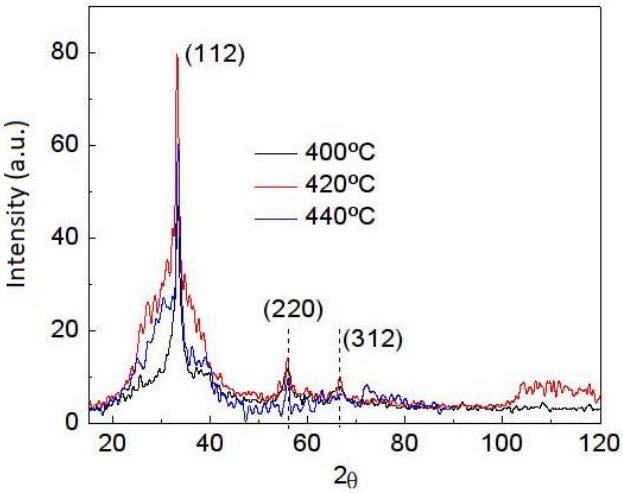

Figure1. XRD patterns of CZTS compound where the contribution of 3 planes can be observed.

Figure 1 shows the results of X-ray diffraction for films grown at temperatures of 400 °C, 420 °C and 440 °C. The measurements were made with the help of a cobalt source (Kα). We know from Bragg's law on X-ray diffraction that[4]:

$$d \sin\theta = \lambda \quad (1)$$

With the help of equation 1 we can find the interplanar distances (d). Taking into account that the CZTS compound has an orthorhombic structure with lattice parameters: $a = b = 5.427$Å and $c = 10.848$Å, with the help of equation (2), the Miller indices of the planes (h, k, l) can be calculated.

$$\frac{1}{d^2} = \frac{h^2+k^2}{a^2} + \frac{l^2}{c^2} \quad (2)$$

Table 1. Miller indices

2θ	Miller indices
33.3	(112)
55.7	(220)
66.8	(312)

The results for different temperatures are shown in **Table 1**. The main planes that contribute to X-ray diffraction are (112), (220) and (312) which can be attributed to the compound CZTS[17,22]. Although the film grown at 420 °C showed a greater contribution to the diffraction of the plane (112) in **Figure 1**, the film grown at 400 °C has a better crystalline quality. As an important result, **Figure 1** showed that the grown films are not amorphous with the formation of the CZTS compound, which will be corroborated by the optical absorption measurements. Degradation in both peak intensity and crystalline quality is observed from **Figure 1** when temperature is increased from 420 to 440 °C, which could be a result of re-evaporation of some elements such as Sn and S under a relatively higher growth temperature.

3.2 EDS and SEM results

3.2.1 Film deposited at 400 °C

For this case, a sulfur composition (S) of 29.6% is obtained, which is lower than the required for the compound stoichiometry, while Cu/(Zn+Sn) and Zn/Sn compositional ratios were:

$$\frac{C_u}{Z_n+S_n} \sim 0.85 \quad (3)$$

$$\frac{Z_n}{S_n} \sim 1.03 \quad (4)$$

It is also important to highlight the fact that compositions close to the stoichiometric are obtained for the temperature of 400 °C. Despite Cu-poor samples are obtained, the condition of Zn-rich samples is not fulfilling which could result in the formation of poor crystalline quality as previously demonstrated[22]. Therefore, for this temperature the optimum compositions relationships were not achieved.

3.2.2 Film deposited at 420 °C

At this temperature, 39% sulfur composition was achieved, while Cu/(Zn+Sn) and Zn/Sn compositional ratios were:

$$\frac{C_u}{Z_n+S_n} \sim 0.84 \quad (5)$$

$$\frac{Z_n}{S_n} \sim 1.16 \quad (6)$$

It is important to note that an increase in the composition of S was obtained with respect to the film deposited at 400 °C. Also, compositional ratios close to optimal ones were obtained; therefore, 420 °C could be more suitable as the substrate temperature for depositing CZTS films in order to be applied in solar cells.

3.2.3 Film deposited at 440 °C

With the increase of the temperature to 440 °C, it is obtained that the concentration of S decreased to 35.1%, for which more losses of this element are obtained with respect to the film deposited at 420 °C, which could be a result of sulfur losses for higher temperatures. In addition, Cu/(Zn+Sn) and Zn/Sn compositional ratios are found to be out of the optimum as shown below:

$$\frac{C_u}{Z_n+S_n} \sim 0.61 \quad (7)$$

$$\frac{Z_n}{S_n} \sim 1.1 \quad (8)$$

In particular, it is observed that for this temperature the sample is much poorer in Cu than the value corresponding to the optimum.

Figure 2 shows the comparison of the morphology of the three films that were deposited at 400 °C, 420 °C and 440 °C. The morphology is highly dependent on temperature. The film deposited at 400 °C illustrates the formation of some porous, while increasing the temperature favors the formation of clusters bigger in size.

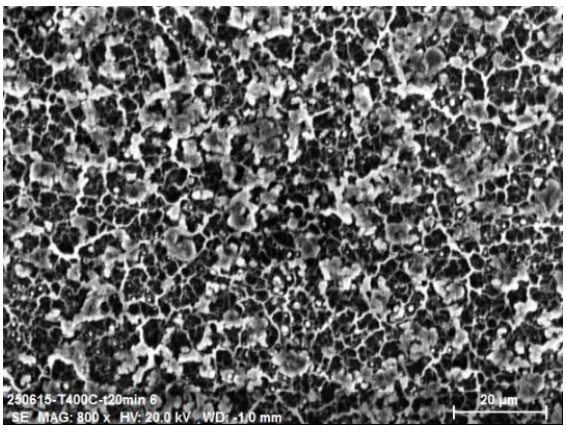

a

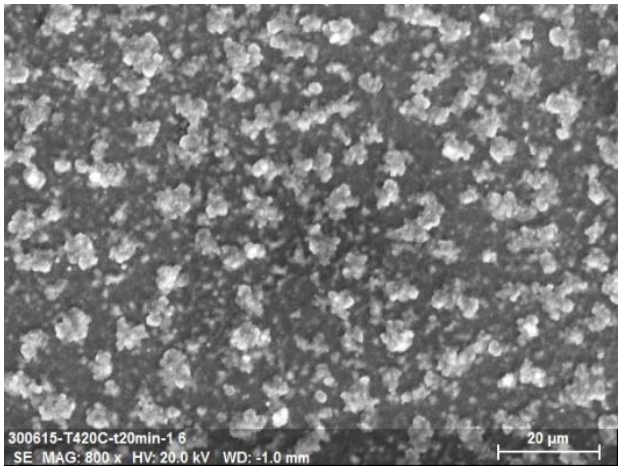

b

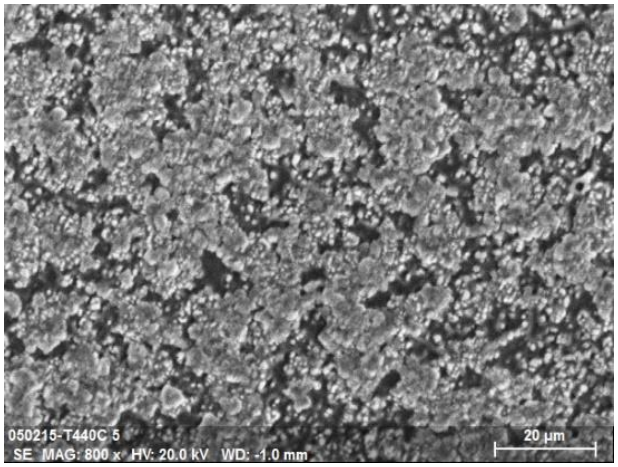

c

Figure 2. Morphological comparison (800x) of the films at 400 °C (**a**), 420 °C (**b**) and 440 °C (**c**).

3.3 Transmittance

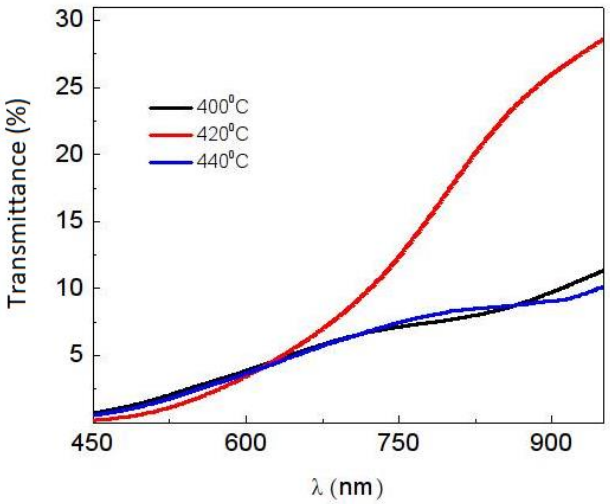

Figure 3. Transmittance of thin films deposited at temperatures of 400 °C, 420 °C, 440 °C.

Figure 3 shows results of the measured transmittances of the films. The transmittance value in all cases was less than 30%, which confirms the potential of the Cu_2ZnSnS_4 material as an absorber. **Figure 4** shows the band gap calculated from the derivative of transmittance. The possible contributions of secondary phases to absorption are illustrated for samples deposited under 400 and 440 °C. For the substrate temperature of 420 °C, a greater contribution of the CZTS material is obtained which corroborates the results obtained in composition and XRD.

4. Discussion

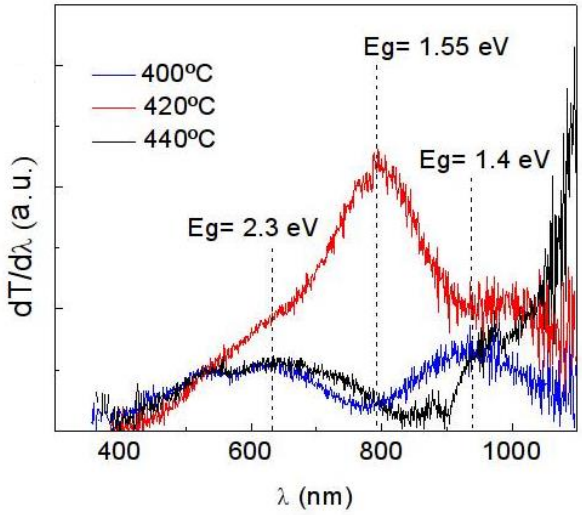

Figure 4. Derivative of transmittance measurements as a function of wavelength for band-gap estimation.

From XRD, EDS and transmittance results, it is found that sample deposited under a substrate temperature of 420 °C is more adequate for solar cell applications. When depositing the CZTS compound starting from precursors containing the four salts (Cu, S, Sn, Zn), in addition to forming the desired compound Cu_2ZnSnS_4, other secondary phases can be formed, which lower the efficiency of the cells. The formation of secondary phases can explain the other contributions to absorption obtained in **Figure 4**. In particular, a band gap value close to 2.3 eV is commonly associated with secondary phases of Cu-S compounds[23]. Therefore, the film grown at 420 °C has a lower contribution of secondary phases. The Cu_2ZnSnS_4 must have an atomic composition of 50% in Sulfur, but because there are some losses due to its high volatility, this composition is always less than 50% unless samples were submitted to a post-thermal annealing under S atmosphere. Therefore, according to the SEM study,

the most optimal film is the one that was grown at a temperature of 420 °C and not only because of the percentage of sulfur but also because of Cu/(Zn+Sn) and Zn/Sn compositional ratios that correspond to an optimized efficiency for this compound as previously demonstrated. On the other hand, the higher the uniformity of the film is, the greater the efficiency of the cell is. According to **Figure 2**, the uniformity increases when the temperature is higher; therefore, for the temperature of 440 °C there are fewer holes (**Figure 2c**) than with the temperature 400 °C (**Figure 2a**) and 420 °C (**Figure 2b**). However, it was already discussed that for this temperature (440 °C), sample is very Cu-poor and therefore the Cu/(Zn+Sn) and Zn/Sn compositional ratios are out of the optimum which will reduce solar cell efficiency. In addition, the samples showed a transmittance of less than 30% which, due to being an absorbing material, it is expected to have a low transmittance (see **Figure 3**). Among the three temperatures, the 420 °C has a better behavior in the transmittance with the wavelength since the derivative (see **Figure 4**) has a peak that corresponds to a band gap of 1.5 eV corresponding to the CZTS[23,24].

5. Conclusions

In this work, a study of the structural, compositional, morphological and optical properties of CZTS films deposited under different substrate temperatures was presented, demonstrating the high dependence of these properties with substrate temperature. It was shown that when working with 4 elements to form the compound Cu_2ZnSnS_4, there is a high probability of the formation of secondary phases. Therefore, it is necessary to study the conditions under which these secondary phases are minimized, since the lower the contribution of these phases, the greater the efficiency of the solar cell. The results showed that the film deposited at a temperature of 420 °C has better properties to be applied in solar cells (band gap of 1.5 eV, a composition of sulfur of 39% as well as Cu/(Zn+Sn) and Zn/Sn compositional ratios close to the optimum).

Conflict of interest

The authors declare that they have no conflict of interest.

Acknowledgements

O. Vigil thanks support from COFAA and EDI of IPN.

References

1. Green MA, Emery K, Hishikawa Y, *et al.* Solar cell efficiency tables (version 43). Progress in Photovoltaics: Research and Applications 2013; 22(1): 1–9.
2. Lee YS, Gershon T, Gunawan O, *et al.* $Cu_2ZnSnSe_4$ thin-film solar cells by thermal co-evaporation with 11.6% efficiency and improved minority carrier diffusion length. Advanced Energy Materials 2014; 5(7): 1401372.
3. Gunawan O, Todorov TK, Mitzi DB. Loss mechanisms in hydrazine-processed $Cu_2ZnSn(Se, S)_4$ solar cells. Applied Physics Letters 2010; 97(23): 233506.
4. Siebentritt S. Why are kesterite solar cells not 20% efficient? Thin Solid Films 2013; 535: 1–4.
5. Gokmen T, Gunawan O, Todorov TK, *et al.* Band tailing and efficiency limitation in kesterite solar cells. Applied Physics Letters 2013; 103: 103506.
6. Polizzotti A, Repins IL, Noufi R, *et al.* The state and future prospects of kesterite photovoltaics. Energy & Environmental Science 2013; 6: 3171–3182.
7. Tanaka T, Kawasaki D, Nishio M, *et al.* Fabrication of Cu_2ZnSnS_4 thin films by co-evaporation. Physical Status Solidi (C) 2006; 3(8): 2844–2847.
8. Babu GS, Kumar YBK, Bhaskar PU, *et al.* Effect of Cu/(Zn+ Sn) ratio on the properties of co-evaporated Cu2ZnSnSe4 thin films. Solar Energy Materials and Solar Cells 2010; 94: 221–226.
9. Fairbrother A, Fontané X, Izquierdo-Roca V, *et al.* Single-step sulfo-selenization method to synthesize $Cu_2ZnSn(SySe1-y)_4$ absorbers from metallic stack precursors. ChemPhysChem 2013; 14(9): 1836–1843.
10. Katagiri H, Jimbo K, Shwe Maw WIN, *et al.* Development of CZTS based thin film solar cells. Thin Solid Films 2009; 517(7): 2455–2460.
11. Zhou Z, Wang Y, Xu D, *et al.* Fabrication of Cu_2ZnSnS_4 screen printed layers for solar cells. Solar Energy Materials & Solar Cells 2010; 94: 2042–2045.
12. Moritake N, Fukui Y, Oonuki M, *et al.* Preparation of Cu_2ZnSnS_4 thin film solar cells under non-vacuum condition. Physica Status Solidi C 2009; 6: 1233–1236.
13. Scragg JJ, Dale PJ, Peter LM, *et al*. New routes to sustainable photovoltaics: evaluation of Cu_2ZnSnS_4 as an alternative absorber material. Physica Status Solidi B 2008; 245(9): 1772–1778.
14. Moriya K, Watabe J, Tanaka K, *et al.* Characterization of Cu_2ZnSnS_4 thin films prepared by photo-chemical deposition. Physica Status Solidi C 2006; 3(8): 2848–2852.
15. Courel M, Valencia-Resendiz E, Pulgarín-Agudelo

FA, *et al.* Determination of minority carrier diffusion length of sprayed-Cu_2ZnSnS_4 thin films. Solid State Electron 2016; 118: 1–3.
16. Courel M, Valencia-Resendiz E, Arvizu JA, *et al.* Solar Energy Materials and Solar Cells 2017; 159: 151–158.
17. Courel M, Andrade-Arvizu JA, Guillén-Cervantes A, *et al.* Optimization of physical properties of spray-deposited Cu_2ZnSnS_4 thin films for solar cell applications. Materials & Design 2017; 114: 515–520.
18. Nakayama N, Ito K. Sprayed films of stannite Cu_2ZnSnS_4. Applied Surface Science 1996; 92: 171–175.
19. Kamoun N, Bouzouita H. Fabrication and characterization of Cu_2ZnSnS_4 thin films deposited by spray pyrolysis technique. Thin Solid Films 2007; 515: 5949–5952.
20. Madarász J, Bombicz P, Okuya M, *et al.* Thermal decomposition of thiourea complexes of Cu(I), Zn(II), and Sn(II) chlorides as precursors for the spray pyrolysis deposition of sulfide thin films. Solid State Ionics 2001; 141-142: 439–446.
21. Katagiri H, Jimbo K, Tahara M, *et al.* The influence of the composition ratio on CZTS-based thin film solar cells. Materials Research Society Symposium Proceedings 2009; 1165: M01–M04.
22. Courel M, Picquart M, Arce-Plaza A, *et al.* Study on the impact of stoichiometric and optimal compositional ratios on physical properties of Cu2ZnSnS4 thin films deposited by spray pyrolysis. Materials Research Express 2018; 5: 015513.
23. Vigil-Galan O, Courel M, Espindola-Rodriguez M, *et al.* Toward a high Cu_2ZnSnS_4 solar cell efficiency processed by spray pyrolysis method. Journal of Renewable and Sustainable Energy 2013; 5: 053137.
24. Kumar YBK, Bhaskar PU, Babu GS, *et al.* Effect of copper salt and thiourea concentrations on the formation of Cu2ZnSnS4 thin films by spray pyrolysis. Physica Status Solidi (A) 2010; 207 (1): 149–156.

Applied Chemical Engineering (2021) Volume 4 Issue 1
doi:10.24294/ace.v4i1.516

ORIGINAL RESEARCH ARTICLE

Optimization of oscillated gas-liquid separator for simultaneous heavy metals determination in water sample

Wameath S. Abdul-Majeed*

Department of Chemical and Petrochemical Engineering, University of Nizwa, PC616, Nizwa, Oman; E-mail: wameath@unizwa.edu.om

ABSTRACT

A technique has been developed to detect and determine multi heavy metals simultaneously in a water sample. Hydride generating technique was implemented to convert the analyte which present in the water sample (liquid phase) into another form with an improved separation coefficient, called "derivative". This process occurred without changing the original chemical structure. Derivatives were separated from the liquid phase by applying custom made gas-liquid separator (GLS), operated with oscillation. Separated species then transferred into a die-electric barrier discharge (DBD) plasma atomizer where a fragmentation of the analyte into free atoms is occurred. The generated atoms were detected by emission spectroscopy. The presented technique was applied for detection of individual and multi heavy metals simultaneously in water sample and proved useful in terms of reducing the effect of the hydrogen generated, through the process, on suppressing the atoms signal in the DBD atomizer.

Keywords: Gas-Liquid Separation; Heavy Metals Detection and Determination; Species Derivatization, DBD Plasma Atomizer

ARTICLE INFO

Received: 16 March 2021
Accepted: 30 April 2021
Available online: 6 May 2021

1. Introduction

Heavy metals are mostly dangerous to humans and other creatures since they can cause significant effects on the body functions, leading to death in considerable number of cases. Heavy metals content in wastewater discharges is considered the most important reason for contamination of natural water bodies. Hence, and for the sake of controlling wastewater disposal, instant sample analysis is required to detect heavy metals, qualitatively and quantitatively, in their different forms with high resolution. This kind of highly accurate analysis can be achieved by coupling two powerful techniques; the first technique achieves separation of various forms of the element of interest, whilst the second technique conducts determination of the metal to low detection limits.

Methods for heavy metals determination are known of two routines. Changes in the chemical properties of such a media are measured due to interactions from external heavy metal species, in the first routine. The second routine is based on applying spectrometric analysis to monitor changes in species structure upon emerging thermal radiation from different sources (e.g. quartz cell or plasma source).

In our previous work[1], a miniaturized dielectric barrier discharge (DBD) microplasma chip was developed as a radiation source for mercury determination in water samples based on $SnCl_2$ as a derivatizing agent. Same system was used in this research applying sodium and potassium hydroborates as derivatizing agents for single and multi heavy

metals simultaneously.

In theory, the efficiency of the hydride generation process (E_{HG}) is represented by the fraction of analyte transported in the form of hydride to the atomizer, as represented by the following formula[2]:

$$E_{HG} = \frac{N_0}{c_0 V_s} \quad (1)$$

Where:

N_0: total number of analyte atoms supplied in the form of hydride to the atomizer;

c_0: analyte concentration in the sample;

V_s: volume of the sample.

Alternatively, the efficiency can be defined for each individual step as follows:

$$E_r = \frac{N_{released}}{c_0 V_s} \quad (2)$$

E_r: hydride release efficiency;

$N_{released}$: total number of analyte atoms released from the liquid sample in the form of hydride.

$$E_t = \frac{N_0}{N_{released}} \quad (3)$$

E_t: hydride transport efficiency, which represents the fraction of the released hydride that would transport to the atomizer.

Thus, individual stages efficiencies are related by the following formula:

$$E_{HG} = E_t \times E_r \quad (4)$$

Accordingly, any disruption that could occur in any of the two stages might lead to disturbing the recorded signal.

Typically, the purge gas (e.g. Argon) is applied to strip the hydride out of the sample solution as well as transporting the released hydride to the atomizer.

Derivatization of the examined analytes has been conducted in this study by applying the hydride generation technique, which is a reaction between the acidified water sample (contains the examined analytes) and the reducing agent (sodium tetrehydroborate, $NaBH_4$). In addition to the generated hydrides, a huge quantity of hydrogen gas is also generated as a result of $NaBH_4$ decomposition. Stoichiometrically, four moles of the hydrogen gas are produced upon decomposing one mole of sodium tetrahydroborate, as illustrated by the following reaction formula[3]:

$$BH_4^- + 3H_2O + H^+ \rightarrow H_3BO_3 + 4H_2$$

It should be noted that the generated hydrogen gas gives rise to the formation of aerosol in the gas liquid separator which consequently disturbs the system performance.

Although the generated hydrogen is considered advantageous for plasma reaction into such extent, it was reported in literature and observed experimentally in this study that a presence of extra hydrogen gas in a DBD plasma reactor affect the plasma stability and result in extinguishing the plasma in some severe cases as illustrated in **Figure 1**, which shows a comparison between the recorded signals in the beginning of the HG reaction and after 2 minutes duration due to hydrogen effect. In this experiment, mercury vapour generation was conducted by using 0.5% m/v $NaBH_4$ stabilized in 0.14% m/v NaOH as a reducing agent. 100 µg/L mercury solution acidified with (1% v/v) HcL was injected to the system with aid of argon gas as a carrier.

Due to its lighter weight, the probability of hydrogen molecule transfer to the atomizer is larger than the generated hydrides, which consequently lead to plasma instability. Chaudhary *et al.*[4] observed this behaviour in their atmospheric pressure cold plasma generator and reported that extra amount of hydrogen lead to destabilize and completely extinguish the plasma. They stated a probable reason for the hydrogen effect on plasma is the ability to alter the electron energy and electron energy distribution function; thus, it would change the population of the reactive species in the discharge.

Although the case described in **Figure 1** represents the derivatization reaction of mercury by using low concentration of $NaBH_4$ (only 0.5% m/v); the disturbance occurred to the spectrum is obviously massive. This case becomes more obvious when using higher concentrations of $NaBH_4$ that is required to derivatize other heavy metals individually or simultaneously. According to the results of the current optimization study, the minimum concentration of $NaBH_4$ that is required to implement the detection of seven heavy metals (simultaneously) was found to be 1.5% m/v, which means possibility of higher hydrogen liberation compared with the previous case of mercury.

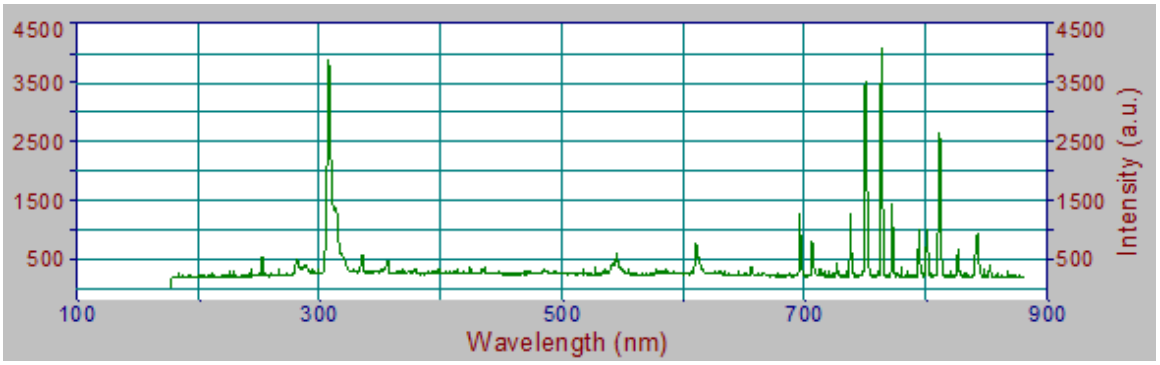

Figure 1. a) Recorded spectrum in the beginning of the reaction.

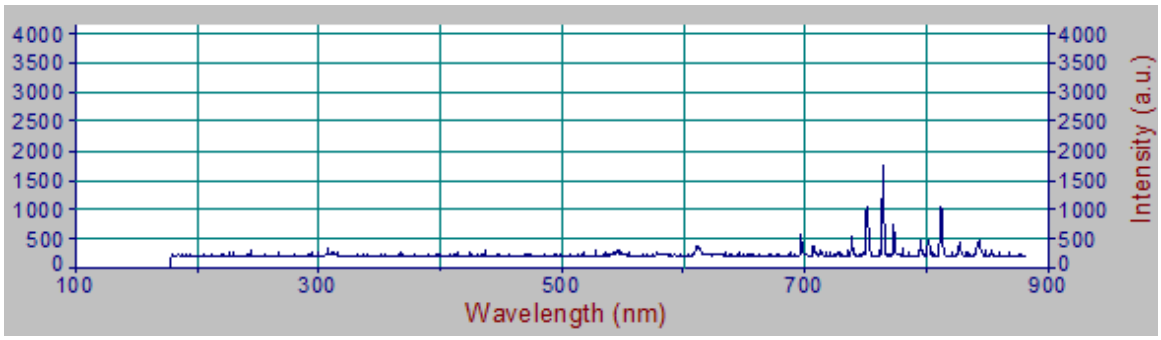

Figure 1. b) Recorded spectrum after 2 minutes.

2. Methodology

A technique based on applying oscillated gas-liquid separator was proposed and examined in this research. The developed system is shown in **Figure 2**. The control strategy of the gas liquid separator has been implemented by assigning a solenoid valve to control the injection of the supporting gas (stream 1) into the GLS (A). The main concept is to supply pulses of the supporting gas through stream (1) which prevents the build-up of high pressure inside the separator and consequently limits the formation of the disturbing factors and facilitates the release of the vapour species without disrupting the bulk. A solenoid valve (Takasago – Japan) with 2 (mm) bore size powered by 12 volt DC was used to implement the injection of the supporting gas pulses. The control strategy of generating the argon gas pulses as well as controlling the other compartments of the proposed system has been accomplished by using a microcontroller (Arduino – Mega) interface which is operated by a PC software. A fibre optic was used to collect the emission spectra which were recorded by (Ocean Optics USB 2000) spectrometer (0.3–1.5 nm FWHM resolution, 600 lines grating density blazed at 300 nm, and 25 µm slit width) and analysed by the Spectra Suite software (Ocean Optics). Other system details are described in our previous paper[1].

In the first instance, several experiments were conducted to investigate the individual detection of single elements. Seven elements were examined individually by applying the continuous gas flow and pulsed gas flow in the GLS includes: Cadmium (288.84 nm), cupper (324.55 nm), tin (326.375 nm), mercury (253.58 nm), arsenic (229.03 nm), nickel (232.06 nm), and lead (220.31 nm). Derivatization of each the elements individually was conducted by applying the optimum reaction conditions which was found applicable for the simultaneous detection of all elements (i.e. acidified water sample (with 1.5 M HCl) contains about 10 ug/L of each examined analyte and using (1.5% m/v) $NaBH_4$ as a reducing agent). The pulsed argon flow experiment was conducted by applying pulses of 75 (mL/min), in a sequence form, for 4 seconds and stopping it for 3 seconds.

Figure 3 illustrates the signals recorded for cadmium by applying the continuous and pulsed flow, respectively. Cadmium was considered very critical when applying the derivatization reaction because a spontaneous generation of cadmium free atoms is occurred from the hydride without any external effect (e.g. plasma).

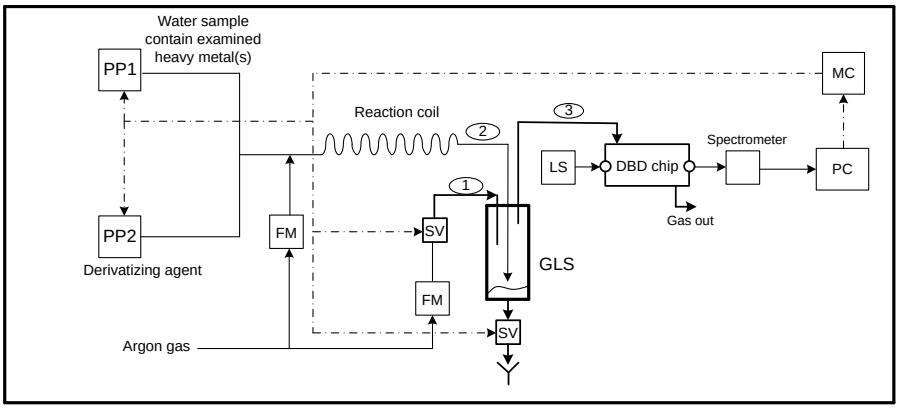

Figure 2. Automated system for determination of individual and multi heavy metals by applying oscillated gas-liquid separator. Note: PP: peristaltic pump, FM: flow meter, SV: solenoid valve, LS: light source, PC: Computer, MC: microcontroller interface, dotted line: signal transfer path, Experimental investigations for assessing the oscillated GLS performance.

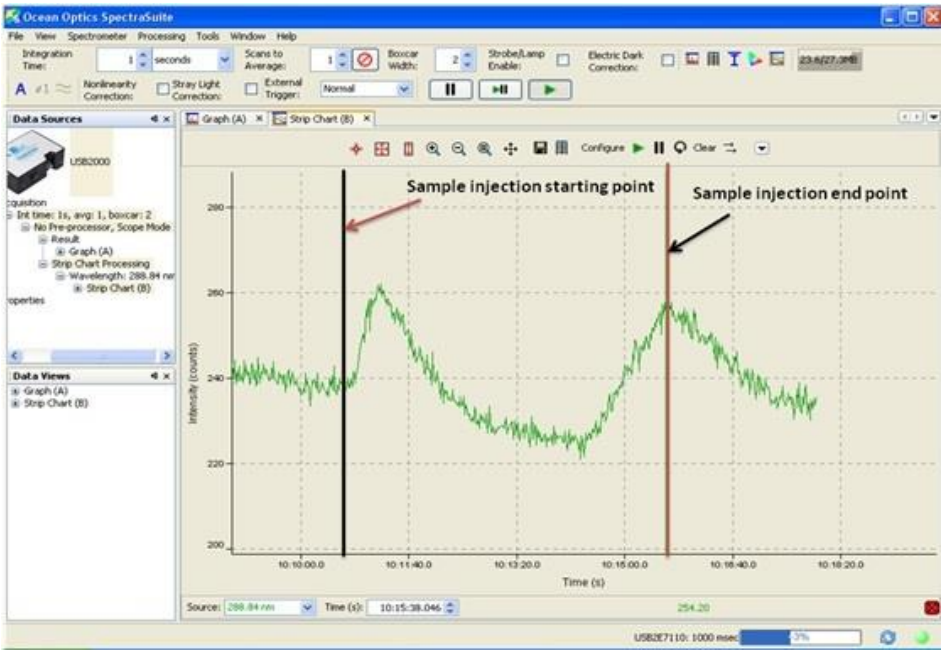

Figure 3. a) Cd derivatization, continuous gas flow 75 mL/min (without pulsing).

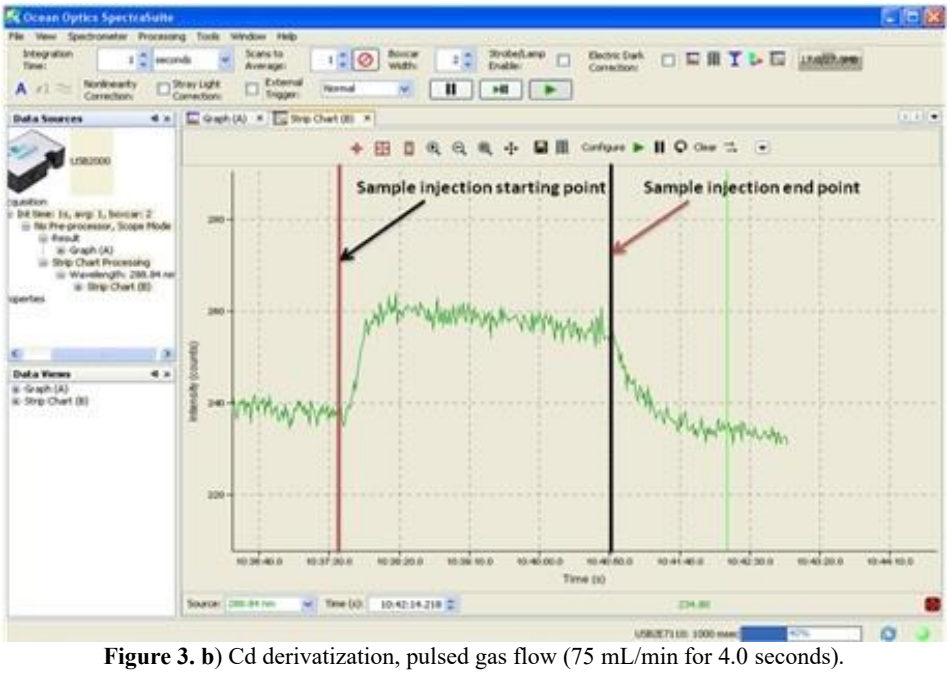

Figure 3. b) Cd derivatization, pulsed gas flow (75 mL/min for 4.0 seconds).

The signals recorded for cadmium has also been observed for the cases of tin and cupper, whereas the rest of the examined elements (Hg, As, Ni, Pb) have shown more stable performance in the cases of continuous and pulsed flow. Accordingly, three elements in the examined set were identified as critical (i.e. Cd, Sn, Cu).

On the other hand, approximately similar trend was observed when using lower gas flow rate (60 mL/min) in the continuous mode; nonetheless, the intensity became lower. In contrast, the disturbance became more obvious when applying higher flow rate in the continuous mode (90 mL/min). In any case, any kind of disturbance in the signal is not preferable and could lead to misleading when applying the quantitative determination.

The performance of GLS has also been investigated when applying the simultaneous detection of analytes. In the first experimental set, the critical elements were detected simultaneously by applying both modes of continuous and pulsed flow. **Figure 4** represents the signals recorded for the examined analytes in both cases by applying same reaction conditions (i.e. acidified water sample with 1.5 M HCl contains about 10 ug/L of each examined analyte and using 1.5% m/v $NaBH_4$ as a reducing agent). Green, pink, and black colored lines represents cadmium, cupper and tin respectively.

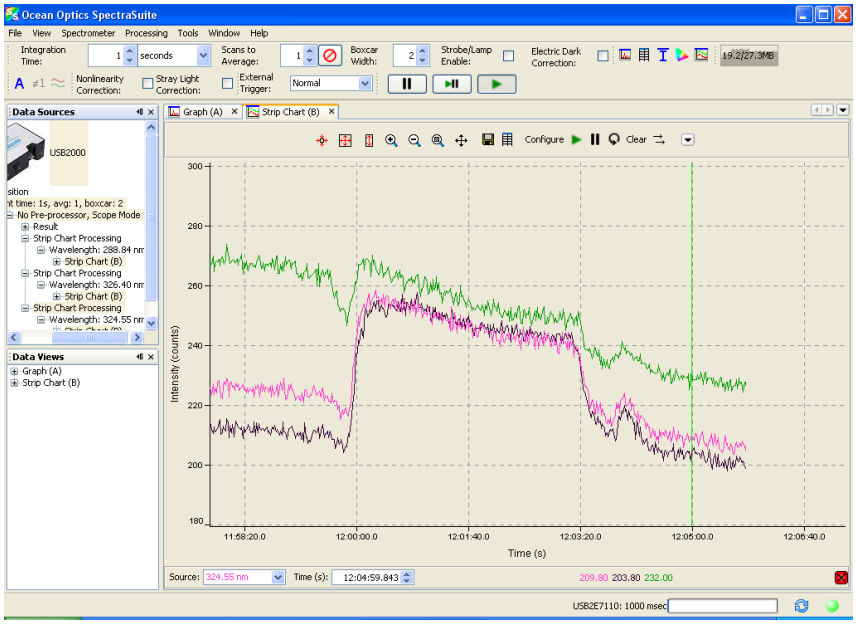

Figure 4. a) derivatization of Cd, Cu, Sn using 1.5% m/v $NaBH_4$ and applying continuous gas flow 75 mL/min (without pulsing).

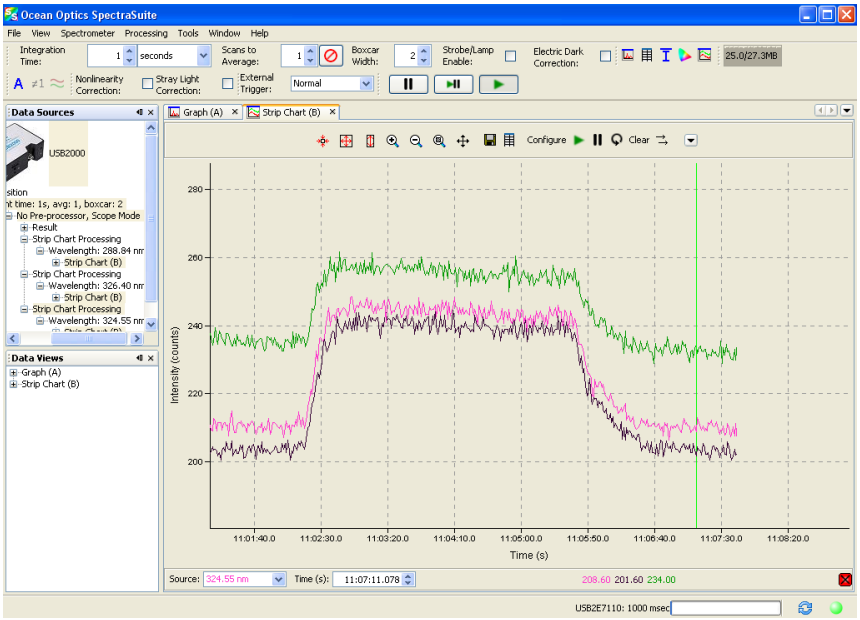

Figure 4. b) derivatization of Cd, Cu, Sn using 1.5% m/v $NaBH_4$ and applying pulsed gas flow (75 mL/min for 4.0 seconds).

Furthermore, the pulsed flow experiment was repeated by applying higher concentration of $NaBH_4$ (2% $NaBH_4$) as shown in **Figure 5**; this was to explore whether applying the pulsed flow is still beneficial or not when using higher concentrations of $NaBH_4$. It should be mentioned that the recorded signals for the case of using (2% $NaBH_4$) in the continuous flow mode have shown more discrepancy.

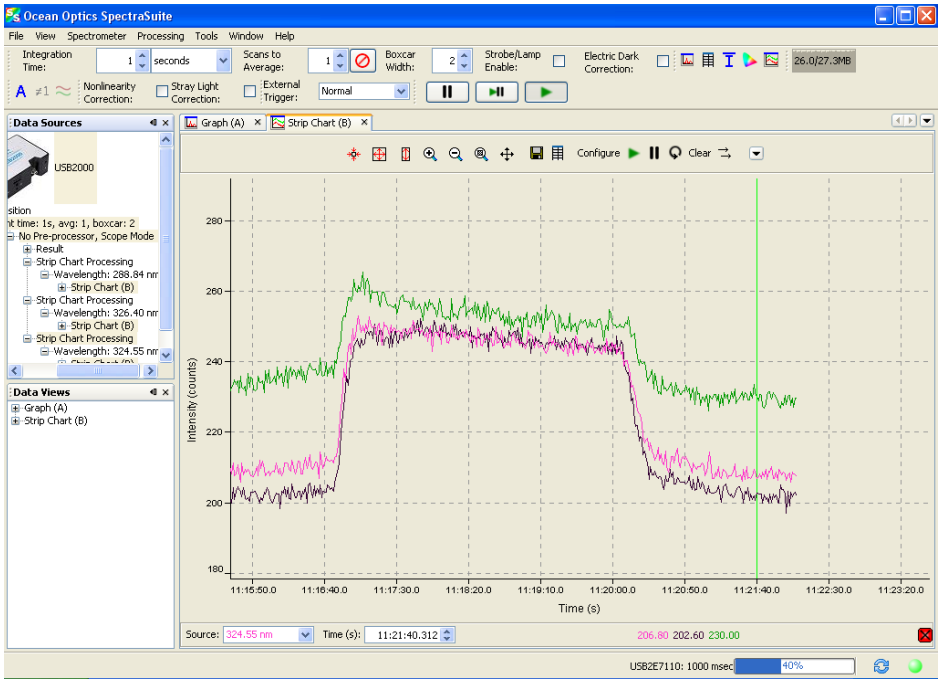

Figure 5. Derivatization of Cd, Cu, Sn using 2.0% m/v $NaBH_4$ and applying pulsed gas flow (75 mL/min for 4.0 seconds).

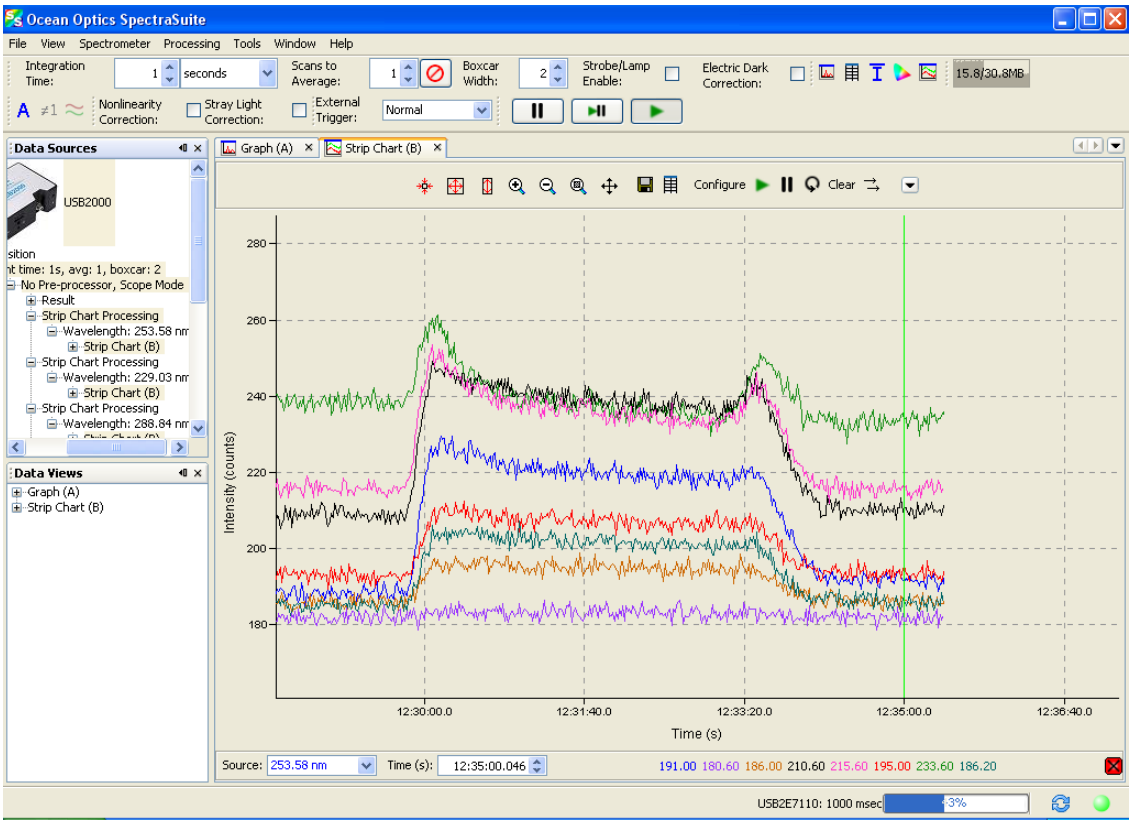

Figure 6. a) 7 elements detection - continuous gas flow 75 mL/min (without pulsing).

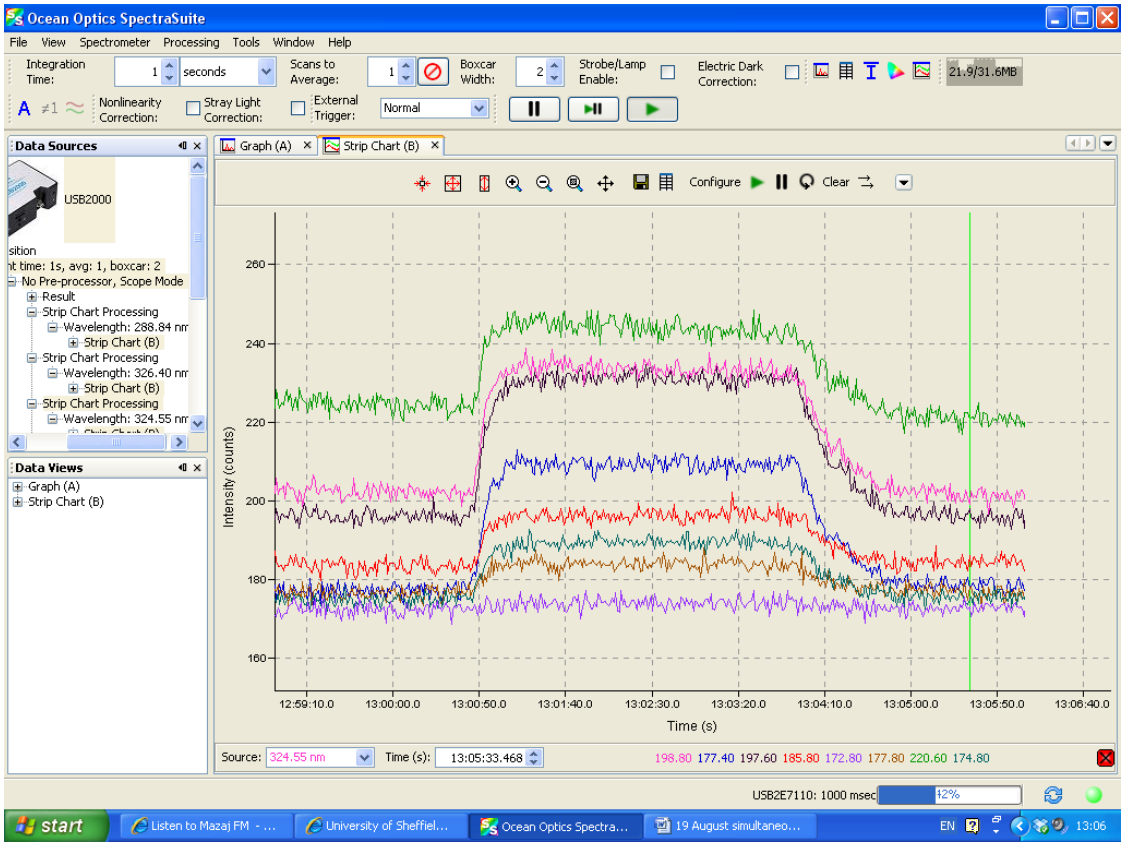

Figure 6. b) 7 elements detection - pulsed gas flow (75 mL/min for 4.0 seconds).

The simultaneous detection of seven heavy metals was implemented by applying the hydride generation reaction for an acidified water sample with 1.5 M HCl contains about 10 ug/L of each examined analyte and using 1.5% m/v $NaBH_4$ as a reducing agent. The gas liquid separator was operated by applying both continuous flow mode (75 mL/min) and pulsed flow mode (sequence form, 4 seconds with injection followed by 3 seconds without injection).

Figure 6 illustrates the recorded signals in both cases where the blue, red, olive and brown colored lines represent mercury, arsenic, nickel, and lead respectively. A violet line at (195.96 nm) was added to represent the stability of background signal.

3. Discussion

The main role of the GLS is to separate the gaseous phase from the liquid matrix upon completion of the reduction reaction. Therefore, design of the GLS should provide optimal separation of the aerosol droplets created by the bubbling action of the evolving gases, which results in signal disruption in the cases of poor separation. In order to understand the function of the gas pulsing on GLS performance, we should consider the massive disturbance which occurred to the whole spectrum upon being affected by extra quantity of hydrogen, as shown in **Figure 1**. It's worth noting that a tendency for aerosol and foam formation is highly possible in any kind of gas liquid separator especially when a huge amount of hydrogen is released to the GLS bulk. Thus, some researchers have considered the foam formation as highly effective on GLS performance; and hence, they used anti-foam agents with the injected samples to reduce this tendency[5]. Nevertheless, those anti foam chemicals could lead to signals interferences especially in the case of conducting simultaneous detection of multi heavy metals.

A probable reason for the improved signal result that obtained from applying the pulsed argon flow could be attributed to a lower hydrogen release rate from the liquid residues which are settled at the base of GLS. It was reported in the literature that extra hydrogen could be released from the liquid residues in the gas-liquid separator due to the instability of these residues. If a forced continuous stream of argon gas is injected toward the liquid surface, which is the case in the current GLS, then hydrogen stripping from the liquid residues would become easier.

Accordingly, the pulses of argon gas result in a gentle argon flow as well as a stable gas bulk inside the GLS, and consequently facilitate the transportation of the generated hydrides from GLS bulk to the DBD atomizer without further hydrogen generation from the liquid residues.

In general, and according to the recorded signals, three elements (Cd, Cu, and Sn) were found more vulnerable to the effect of hydrogen compared to other elements and defined as "critical". The reason could be interpreted from the spectrum shown in **Figure 1** where the top section shows the full spectrum before being subjected to the disturbance from the generated hydrogen. It can be observed in **Figures 4 and 5** that the emission lines of the critical elements [Cd (288.84 nm), Cu (324.55 nm), and Sn (326.375 nm)] are located at positions in the spectrum which were extremely disturbed upon being subjected to the hydrogen effect. The mostly affected area in the spectrum (around 300 nm) has been identified with existence of molecular N_2 in the region (337–380 nm) whereas the bands between (280–285 nm) and (302–317 nm) were defined as OH molecular emission lines. In addition to the abovementioned, the lines at (391.4 and 427 nm) were attributed to the N_2^+ molecular bands[6]. It seems that the identified species in the defined regions above were affected massively due to the hydrogen effect; therefore the signals recorded for the critical elements have shown instability (a gradual increase when the reaction started—a gradual decrease when the hydrogen entered to the atomizer—and finally a gradual increase when the sample injection stopped and the hydrogen become less in the system). Other elements were found more stable due to the positions of their emission lines in the spectrum, which is far from the mostly affected region. Even when the concentration of $NaBH_4$ increased to 2% m/v, the recorded signals of critical elements were found stable in the pulsed mode which indicates the performance of GLS is still reasonable.

4. Conclusions

In conclusions, applying the pulsed argon flow in the gas liquid separator has resulted more stable performance and relatively higher signal intensities even when applying higher concentration of $NaBH_4$. This improvement could be more obvious when applying the quantitative determination of multi heavy metals.

Conflict of interest

No conflict of interest was reported by the author.

References

1. Abdul-Majeed WS, Parada JHL, Zimmerman WB. Optimization of a miniaturized DBD plasma chip for mercury detection in water samples. Analytical and Bioanalytical Chemistry 2011; 401(9): 2713–2722.
2. Dedina J. Hydride generation atomic absorption spectrometry. Chichester: John Wiley &Sons Ltd; 1995.
3. Agterdenbos J, Bax D. Mechanisms in hydride generation AAS. Fresenius' Journal of Analytical Chemistry 1986; 323: 783–787.
4. Chaudhary K, Inomata K, Yoshimoto M, Koinuma H. Open-air silicon etching by H_2–He–CH_4 flowing cold plasma. Materials Letters 2003; 57: 3406–341.
5. Karadjova IB, Lampugnani L, Onor M, *et al.* Continuous flow hydride generation-atomic fluorescence spectrometric determination and speciation of arsenic in wine. Spectrochimica Acta Part B: Atomic Spectroscopy 2005; 60: 816–823.
6. Zhu Z, Chan GCY, Ray SJ, *et al.* Microplasma source based on a dielectric barrier discharge for the determination of mercury by atomic emission spectrometry. Analytical chemistry 2008; 80: 8622–8627.

Applied Chemical Engineering (2021) Volume 4 Issue 1
doi:10.24294/ace.v4i1.802

ORIGINAL RESEARCH ARTICLE

The role of dysprosium ions as a dopant on linear and nonlinear optical dispersion parameters in a-Se thin film

Fathy A. Abdel-Wahab*, Heba Abdel Maksoud

Physics department, Faculty of Science, Ain Shams University, Abbassia, Cairo, Egypt. E-mail: fabdelwahab2003@yahoo.com

ABSTRACT

Thin films of un-doped and doped a-Se with Dysprosium rare-earth ions have been prepared by the thermal evaporation technique. The optical transmission spectra of the investigated films have been measured in a wide spectral range and used to calculate the linear optical constants together with the optical energy gap of studied films. The observed decrease in the values of the energy gap against the increase of the Dysprosium (Dy) content in a-Se films has been explained using Mott and Davis Model and in terms of electronegativity difference of the constituent atoms. Furthermore, the dispersion of nonlinear parameters such as second-order refractive index and nonlinear absorption coefficient (two-photon absorption coefficient) of investigated films are presented and discussed.

***Keywords*:** Selenium Thin Films; Doping of Selenium; Rare Earth; Optical Properties of Doped Selenium

ARTICLE INFO

Received: 7 April 2021
Accepted: 1 June 2021
Available online: 5 June 2021

1. Introduction

Rare-earth (RE)-doped glass fiber amplifiers operating at a 1.3 μm wavelength band have received extensive attention due to the zero-dispersion of the silica fiberglass in the 1.3 μm-wavelength region, and most installed fibers worldwide are optimized at this wavelength[1-4]. In contrast, Dysprosium rare-earth atoms, Dy which have an active unfilled f shell in its electronic configuration ([Xe] $4f^{10}4s^2$), can provide 1.3 μm emission due to the $^6F_{11/2}$, $^6H_{9/2}\rightarrow{}^6H_{15/2}$ transition[5]. In addition, Dy has a good absorption band at approximately 800 nm, at which level a cheap commercial laser diode could be used for excitation. On the other hand, amorphous Selenium (a-Se) is characterized by the existence of localized states in its mobility gap. These states are created due to the presence of structural defects and the absence of long-range order[6–8]. The structural disorder made a-Se and its alloys have high optical transparency in the infra-red (IR) spectral regions up to 10 μm. Besides, it has a large refractive index, thermal stability, and a high degree of covalent bonding. Furthermore, due to high rare-earth solubility, high emission quantum efficiency[9], and the low phonon energy (~ 250 cm^{-1}) of amorphous selenides compared with fluorides (~ 550 cm^{-1}), or oxide glasses (~ 1100 cm^{-1})[10], it could be used as a suitable host medium for Dy ions to enhance its mid-IR laser emission. It should be noted that the low phonon energy of a-Se decreases the multi phonon relaxation which enables an active transition between rare-earth atom levels in the middle IR spectral region. Consequently, the exploration of the optical properties of doped a-Se with Dy ions is very important to improve the performance of Laser emission[11].

In the previous work[12], the study of Selenium films was intended to have a comprehensive understanding of the influence of Dysprosium (Dy) ion dopant on the ac conductivity and dielectric parameters of a-Se films. The present aims to gain a better investigation on the effect of doping with Dy on the optical dispersion relations of the complex dielectric constant, optical energy gap, and material dispersion. Furthermore, the effect of doping of a-Se with Dy ions on second-order refractive index and two-photon absorption is calculated and discussed.

2. Experimental details

Bulk selenium doped with Dysprosium with ratios 0.008 and 0.01 at. % were prepared by mixing suitable proportions of Se and Dy, of purity 5 N, in a silica tube sealed at 10-5 Torr. The mixture was heated in an electric furnace up to 950 °C and kept at that temperature for 9 h. The obtained bulk ingots are used as source material to prepare thin films by the thermal evaporation technique. More details about bulk and thin films preparation of Se doped Dy are given elsewhere[12]. After evaporation, the thickness of the fresh films was accurately determined by an optical interference method and is found to be in the range of 750-804 nm.

The structural phase of as-prepared thin film samples has been identified using an X-ray diffraction pattern (XRD) computerized system (model: Philips EXPERT-MPDUG PW-3040 diffractometer with Cu Ka radiation source). The computer-aided two-beam spectrophotometer of type Shimadzu-3101PC UV-VIS-NIR, is used to record the optical transmittance (T) as a function of wavelength (λ) for the investigated films. A resolution limit of 0.2 nm and a sampling interval of 2 nm was utilized for recording the different measuring points. The accuracy of measuring $T(\lambda)$ is 0.003 with the incident beam at normal incidence to the film surface. The optical measurements were carried out at room temperature in the spectral region of 500-2500 nm.

3. Results and discussion

The recorded XRD patterns for the studied as-prepared a-Se, previous work of $SeDy_{0.008}$ films[12], and the present work [p. w.] of Se films doped with 0.01 at. % with Dy is shown in **Figure 1**. In this figure, the XRD pattern of the fresh Se films reflects its amorphous nature. The observed diffraction peaks in case of Se doped with 0.008 at. % Dy[12] means the growth of the crystalline phase at the expense of an amorphous state. This crystalline phase consists of mixed phases of elemental Se, Dy, and tetragonal and orthorhombic structures of SeDy as shown in **Figure 1**. Furthermore, increasing the Dy content in a-Se up to 0.01 at. % increased the intensity of the diffraction peaks for (102) of Dy and (002), (003), and (112) phases for SeDy which means that increasing the growth of crystalline zones in $SeDy_{0.01}$ as shown in **Figure 1**.

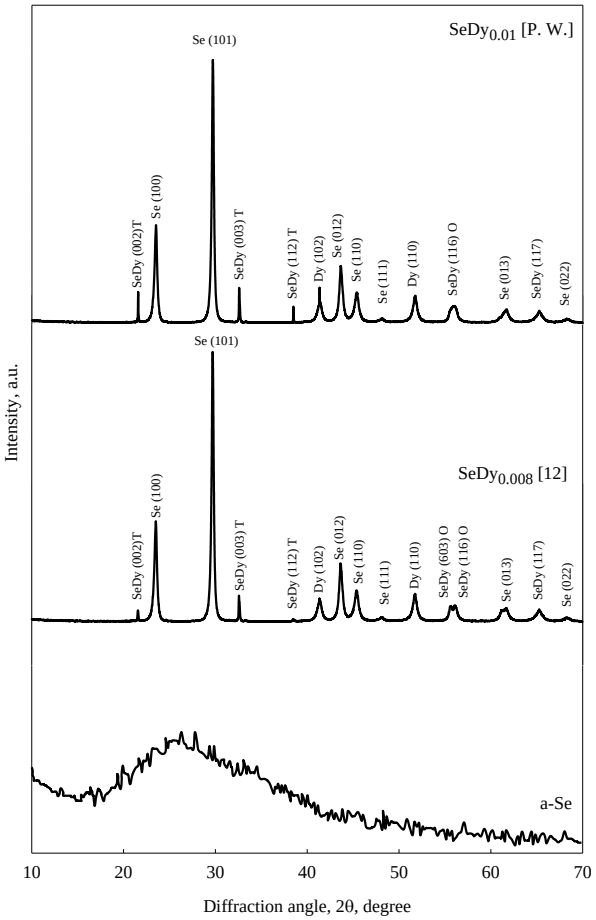

Figure 1. XRD pattern for a-Se, previous work of $SeDy_{0.008}$[12] and the present work [P.W.] of $SeDy_{0.01}$ thin films. It should be noted that the diffraction pattern of $SeDy_{0.008}$[12] is added to the figure for the sake of comparison.

3.1 Linear optical dispersion

The linear (weak field) optical constants such as refractive index (n), extinction coefficient (k), and optical energy gap, E_g, are considered as key parameter for optimizing the optical properties of a given optical application[13]. The measured optical transmission against wavelength is used to evaluate the

linear constant *n* and *k* for un-doped and Dy-doped Se-films using the Swanepoel method[14–16].

The dependence of the calculated linear optical constants *n* and *k*, on the applied wavelength for the studied samples is shown in **Figure 2**. In **Figure 2a** the Cauchy fitted values of *n* show a decrease against wavelength and an increase in the magnitude as the doping level of Dy increase in the structural network of a-Se. The dependence of the extinction coefficient (*k*) on λ shown in **Figure 2b** illustrates a decrease in exponential trend as λ increases and an increase against the doping content with Dy in a-Se films.

Figure 3 shows the refractive index as a function of composition for the investigated a-Se doped with Dy rare-earth ions films together with those published in literature at λ = 1.3 μm using different preparation techniques. The general trend of the function is the increase of *n* against Dy content ratio in at. %. However, the discrepancy among the data published by assorted authors is attributed to the variation in the preparation techniques used in formulating the studied materials in each reference besides the dependence of the properties of chalcogenides on its thermal history. In reference[17] bulk samples are prepared by conventional melt quenching technique for the mixture of the constituent elements. The obtained ingots are annealed at their glass transition temperature before any measurements. Furthermore, in reference[18] the obtained melt quenched ingots are used as source material to prepare thin film samples using KrF excimer laser operating at 248 nm.

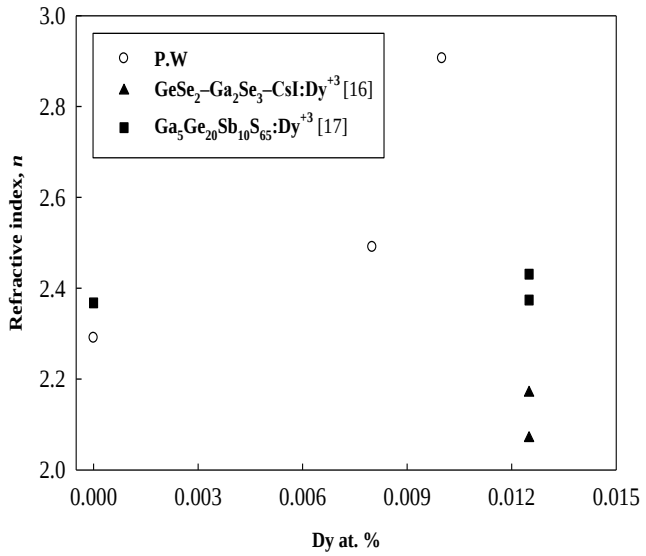

Figure 3. The variation of refractive index as a function of the doped Dy rare-earth ions in at. % for the present work [P. W.].

with those published in the literature[17,18].

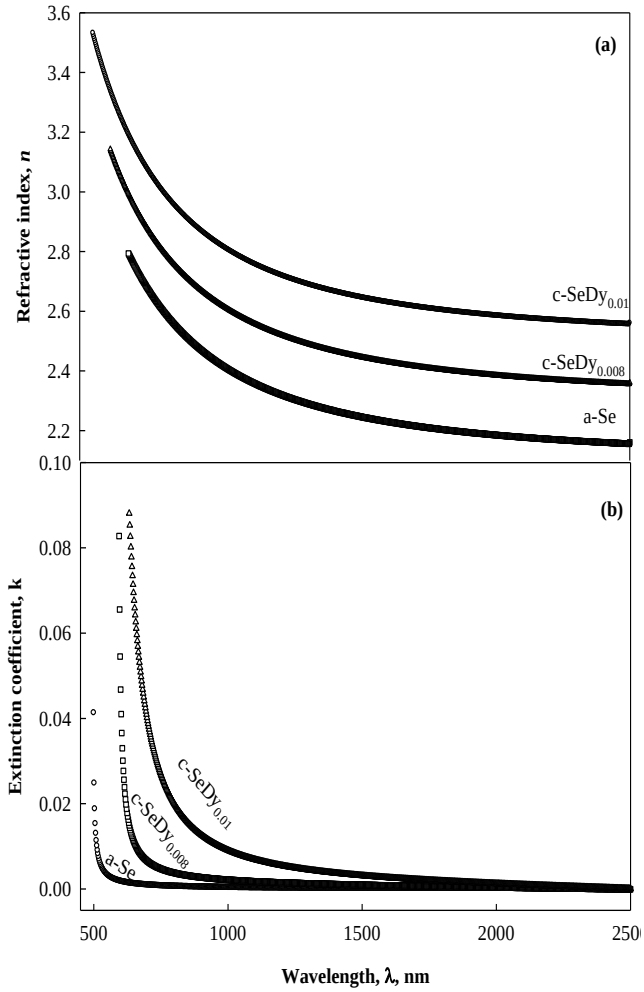

Figure 2. Variation of refractive index (*n*) (**a**) and extinction coefficient (*k*) (**b**) with wavelength (λ) for studied amorphous Se, c-SeDy$_{0.008}$ and c-SeDy$_{0.01}$ thin films.

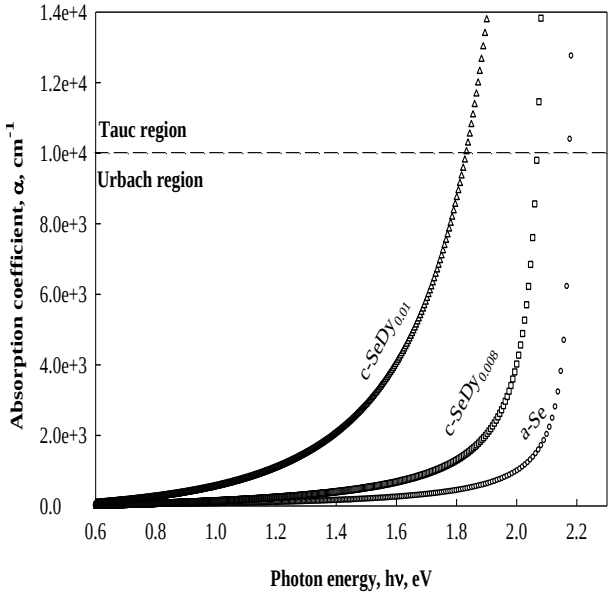

Figure 4. The calculated absorption coefficient (*α*) as a function of photon energy (*hv*) for the studied films. The dashed horizontal line differentiates between the Tauc and Urbach regions.

The dependence of the optical absorption coefficient (α) calculated using values of the extinction coefficient in **Figure 2b** on the incident photon energy of the investigated films is shown in **Figure 4**. This figure confirms that for all studied samples the value of α increases against photon energy in an exponential trend and shifted towards lower energy as doping rate increases in the structural network of a-Se films. This shift indicates that the absorption edge decreases in energy (redshift in wavelength) against the increase of doping level of Dy.

Each curve recognized in **Figure 4** could be divided into two different regions[19,20]:

The first region is for the high absorption, namely for $\alpha(h\nu) > 10^4$ cm^{-1} (Tauc region). The optical absorption in this region could be described by Tauc's relation[19]:

$$\alpha(h\nu) = A(h\nu - E_g)^r \quad (1)$$

where A is constant, E_g the optical band gap and r = 1/2 as well as 2 for direct and indirect transitions in sequence. According to Eq. (1), the dependence of $(\alpha h\nu)^{1/r}$ versus $h\nu$ is shown in **Figure 5** for both values of r. For each composition, the energy gap E_g is calculated by fitting the function $(\alpha h\nu)^{1/r} = f(h\nu)$, locally point by point to the linear regression line and extrapolating to $y = 0$ yields the value of E_g. The results are given in **Table 1** as a function of the film's composition. According to **Table 1**, it is observed that the value of optical band gap E_g decreases against an increase of Dy content through the considered range of doping 0.008-0.01 at. % of Dy.

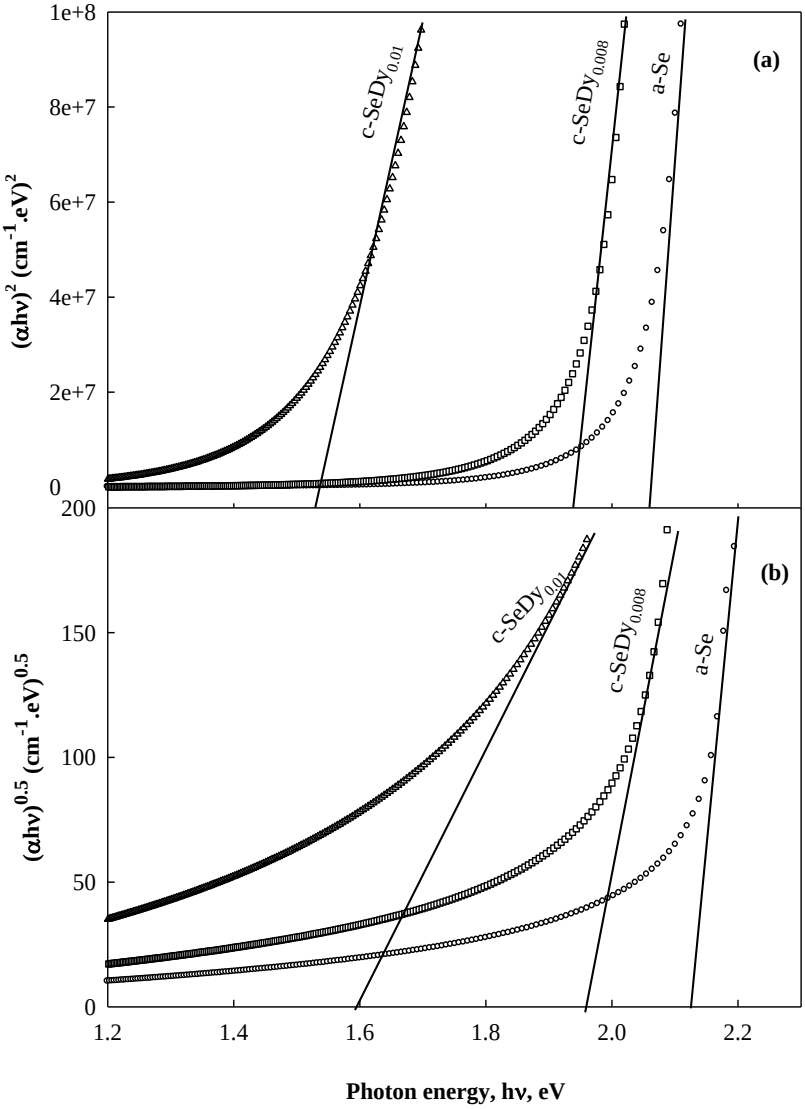

Figure 5. Tauc's plots for determining the optical energy gap of direct (**a**) and indirect (**b**) transitions for films investigated.

The decrease E_g against the increase of Dy content in the structure network of a-Se can be explained using the electronegativity of the elements involved. The electronegativity of Se and Dy are 2.55 and 1.22

respectively and Dy has a lower electronegativity than Se. The valance band of a-Se contains the lone pair p-electrons and the addition of an element with lower electronegativity (Dy) to a higher electronegative element (Se) may raise the energy of lone pair states, which is further responsible for the broadening of the valance band inside the forbidden gap and leads to band tailing and hence bandgap shrinkage[18].

The second region in **Figure 4** with $\alpha(h\nu) < 10^4$ cm^{-1} (Urbach region), where the absorption coefficient presents a roughly exponential behavior:

$$\alpha(h\nu) = \alpha_e \exp\left(\frac{h\nu}{E_u}\right) \quad (2)$$

Where α_e is a constant and E_u is an energy that is often interpreted as the width of the tail of localized states in the gap region. This relation was first proposed by Urbach[21]. The inverse slope or width of the exponential edge E_u reflects the width of the localized band tail[22] which is called Urbach energy. It determines the degree of disorder in the semiconductor which is responsible for internal potential fluctuations giving rise to tails of localized states at the band edges. The Urbach energy depends strongly on deposition conditions and annealing, which are likely to influence the disorder and therefore the band tailing[23]. The calculated values of E_u are given in **Table 1** as a function of film composition. These values show a decrease from 0.30 eV for the un-doped a-Se film to 0.25 and 0.21 eV for doping with 0.008 and 0.01 at. % in sequence. Such a decrease in the value of E_u indicates a decrease in the disordered character of a-Se due to the introduction of Dy which is consistent with the obtained structure using XRD for the studied samples shown in **Figure 1**. consequently, a decrease of E_u is attributed to the crystallized character of the thermally deposited films. Also, the existence of a band tail (E_u) that accompanied the localized states in the gap reflects some degree of disorder in the considered semiconductor film.

The complex dielectric constant $\varepsilon^* = \varepsilon_1 - i\varepsilon_2$ of a martial in terms of the linear optical constants, n, and, k, could be written as $\varepsilon_1 = n^2 - k^2$, $\varepsilon_2 = 2nk$ where ε_1 is the real part, while ε_2 is the imaginary part. **Figure 6** shows the calculated values of ε_1 and ε_2 of the complex dielectric constant versus the photon energy ($h\nu$)

Table 1. The calculated values of the optical energy gap, E_g, Urbach energy, E_u, high-frequency dielectric constant, ε_∞, the ratio of the free carriers density to the free carrier effective mass, N/m^* and plasma resonance frequency, ω_P, as a function of the studied film's composition

Film Composition	E_g, eV	E_u, eV	ε_∞	(N/m^*) x 10^{50} (cm^{-3} kg^{-1})	ω_p x 10^{14} Hz
a-Se	2.10	0.30	4.91	5.710	1.94
c-$SeDy_{0.008}$	1.96	0.25	5.54	6.079	2.48
c-$SeDy_{0.01}$	1.59	0.21	6.77	6.250	2.87

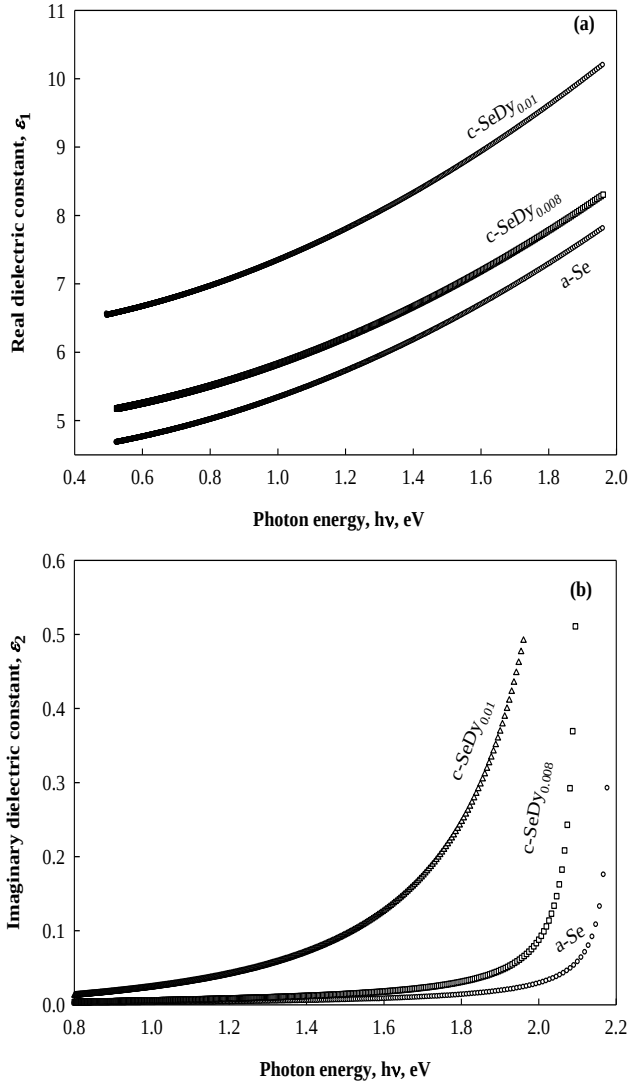

Figure 6. Real (**a**) and imaginary (**b**) parts of the dielectric constant versus photon energy for the films investigated.

for the present film's composition. **Figure 6a** shows a nearly exponential increase with photon energy for all investigated samples and nearly has the same trend as $n = f(\lambda)$. On the other hand, ε_2 illustrates a clear exponential increase of ε_2 against ($h\nu$) which has the same behavior as $k = f(h\nu)$. For a better

understanding of the optical behavior of the investigated films, it is necessary to determine some optical parameters such as dispersion of high-frequency dielectric constant and the lattice vibration modes as follows:

In the near-infrared spectral region, where the frequency is relatively low, the real ε_1 and imaginary ε_2 parts of the complex dielectric constant can be written as[24]:

$$\varepsilon_1 = \varepsilon_\infty - \frac{e^2}{4\pi^2 c^2 \varepsilon_0}\frac{N}{m^*}\lambda^2, \quad \varepsilon_2 = \frac{\varepsilon_\infty \omega_p^2}{8\pi^3 c^3 \tau}\lambda^3 \tag{3}$$

where ω_p is the plasma resonance frequency $\omega_p = \left(\frac{e^2 N}{\varepsilon_0 \varepsilon_\infty m^*}\right)^{\frac{1}{2}}$ of all the valence electrons involved in the optical transitions, ε_∞ the high-frequency dielectric constant, e electronic charge, c speed of light, ε_0 free space dielectric constant, N/m^* is the ratio of free carriers density to the free carrier effective mass and τ relaxation time. According to Eq. (3) plot of ε_1 versus λ^2 and extrapolating the linear part of the plot in the high wavelength region to zero wavelength gives the value of ε_∞ and the slope of this line is used to calculate values of (N/m^*) for the investigated films. The calculated ε_∞, (N/m^*) and ω_p are given in **Table 1** as a function of investigated film compositions. The value of N/m^* reflects an increase in the free carrier density with the increase of Dy-content which is argued to be the metal character of Dysprosium rare earth.

According to the single-effective oscillator model suggested by Wemple and DiDomenico[25], the refractive index could be described by the following relation:

$$n^2 - 1 = \frac{E_0 E_d}{E_0^2 - E^2} \tag{4}$$

where E is the photon energy in eV, E_0 is the single oscillator energy (average oscillator energy for electrons) and E_d is the dispersion energy parameter of the material. For the magnetic chalcogenides such as the present case of Dy doped Se films, Eq. (4) could be rewritten as[25]:

$$n^2 - 1 = \frac{\hat{E}_d \hat{E}_0}{\hat{E}_0^2 - E^2} + \frac{E_d E_0}{E_0^2 - E^2} \tag{5}$$

where $\hat{E}_d$, $\hat{E}_0$ applies to $f \rightarrow d$ transitions and E_d, E_0 applies to $s, p \rightarrow d$ transitions. It is straightforward to combine terms in Eq. (5) and get the following expressions for the equivalent single oscillator parameters $\bar{E}_0$ and $\bar{E}_d$[25]:

$$\bar{E}_0^2 = \hat{E}_0^2\left(\frac{1+\left(E_d/\hat{E}_d\right)\left(\hat{E}_0/E_0\right)}{1+\left(E_d/\hat{E}_d\right)\left(\hat{E}_0/E_0\right)^3}\right) \tag{6}$$

and

$$\bar{E}_d^2 = \hat{E}_d^2\left(\frac{\left[1+\left(E_d/\hat{E}_d\right)\left(\hat{E}_0/E_0\right)\right]^3}{1+\left(E_d/\hat{E}_d\right)\left(\hat{E}_0/E_0\right)^3}\right) \tag{7}$$

$\bar{E}_0$ is the dispersion energy parameter of the material and is a measure of the strength of interband optical transitions and $\bar{E}_d$ is related to the nearest neighbor cation coordination, anion valency, ionicity, and the effective number of dispersion electrons. According to Eq. (5) Plotting $(n^2\text{-}1)^{-1}$ versus the photon energy $(h\nu)^2$ as shown in **Figure 7** and fitting the straight part of the curve in the high energy region allows to obtain from the slope and the intercept values of E_0 and E_d. In the low energy region, the slope and intercept of the straight yields the values of $\hat{E}_d$ and $\hat{E}_0$. The calculated values of these dispersion parameters are listed in **Table 2**.

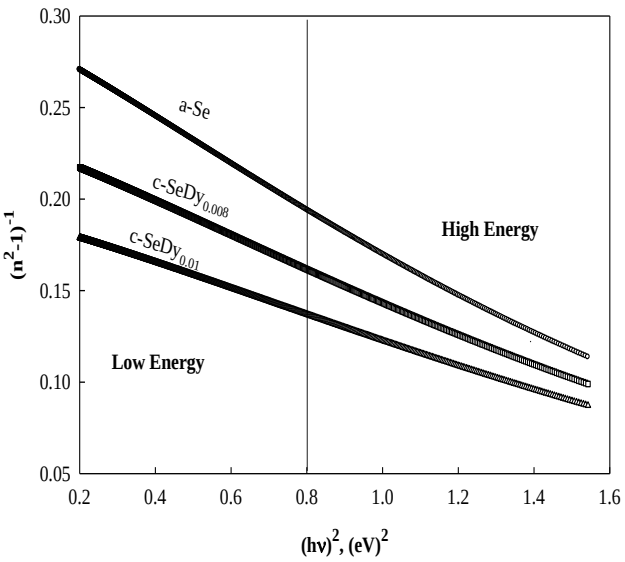

Figure 7. Plots of $(n^2\text{-}1)^{-1}$ versus $(h\nu)^2$ for the films investigated.

The estimated value of E_0 for a-Se (4.5 eV) is in good agreement with that reported by Wemple[26]. The results indicated that the average value of the single oscillator energy ($\bar{E}_0$) changed to 3.79 eV for c-$SeDy_{0.008}$ and 4 eV for c-$SeDy_{0.01}$. Such behavior of $\bar{E}_0$ could be attributed to the splitting of the sub-bands $5d(t_{2g}\text{-}e_g)$ by the crystal field and the

decrease of this splitting as well as the crystallized nature with increasing Dy-content.

If the wavelengths are much shorter than the phonon resonance, the lattice contribution is given by:

$$n^2 - 1 = \frac{\hat{E}_d \hat{E}_0}{\hat{E}_0^2 - E^2} + \frac{E_d E_0}{E_0^2 - E^2} - \frac{E_l^2}{E^2}, \quad (8)$$

where E_l is the lattice oscillator strength. Poignant[27] has shown that at a long wavelength, where $E^2 << \hat{E}_0^2$ and $E^2 << E_0^2$, a plot of $(n^2\text{-}1)$ versus $1/E^2$ approaches a straight line and Eq. (8) has the following form:

$$n^2 - 1 = \left(\frac{\hat{E}_d}{\hat{E}_0} + \frac{E_d}{E_0}\right) - \frac{E_l^2}{E^2} \quad (9)$$

The intercept of this line yield the ratio E_d/E_0 at high energy, and $\hat{E}_d/\hat{E}_0$ at low energy, while the slope is $-E_l^2$. The obtained values of E_l are given in **Table 2**. The tabulated values of E_l shows variation from 0.54 eV for a-Se to 0.36 eV for c-$SeDy_{0.008}$, and 0.38 eV for c-$SeDy_{0.01}$ respectively.

Table 2. Values of single oscillator energy (E_0, $\bar{E}_0$), dispersion energy (E_d, $\bar{E}_d$) lattice oscillator strength (E_l), and wavelength at zero material dispersion (λ_c) for investigated films composition

Film Composition	E_0, eV	E_d, eV	$\hat{E}_0$, eV	$\hat{E}_d$, eV	$\bar{E}_0$, eV	$\bar{E}_d$, eV	E_l, eV	λ_c, µm
a-Se	4.50	24.25	-----	-----	------	-----	0.54	1.60
c-$SeDy_{0.008}$	3.74	12.62	2.49	6.34	3.97	8.36	0.36	1.66
c-$SeDy_{0.01}$	3.18	11.66	2.17	5.45	4.00	12.65	0.38	1.74

The material dispersion $M(\lambda)$ could be expressed in terms of the refractive index, n, as:

$$M(\lambda) = \frac{\lambda}{c}\left(\frac{d^2 n}{d\lambda^2}\right) \quad (10)$$

Differentiating Eq. (8) w.r.t λ yields the material's dispersion as a function of $\bar{E}_0$ and $\bar{E}_d$ as follows[26]:

$$M(\lambda) = 1.54\times10^4 \frac{\bar{E}_d / \bar{E}_0^3}{n\lambda^3} - 2.17\times10^3 E_l^2 \frac{\lambda}{n} \quad (ps\,nm^{-1}km^{-1}) \quad (11)$$

Figure 8 shows the graphical relation of the calculated $M(\lambda)$ versus wavelength. The wavelength at which $M = 0$, and the obtained results are given in **Table 2** as a function of films composition. Similarly, the value of λ_c can be calculated from Wemple's three-parameter formula[26]:

$$\lambda_c = 1.63\left(\frac{\bar{E}_d}{\bar{E}_0^3 \bar{E}_l^2}\right)^{\frac{1}{4}} \quad (12)$$

Nevertheless, the observed variation of λ_c indicates that the introduction of Dy atoms in a-Se causes a shift of the material dispersion $M(\lambda)$ towards higher wavelengths. Such a redshift represents an important parameter to improve the operational conditions and performance of optical fibers[28,29]. Indeed, the listed values of material dispersion in **Table 2** show that

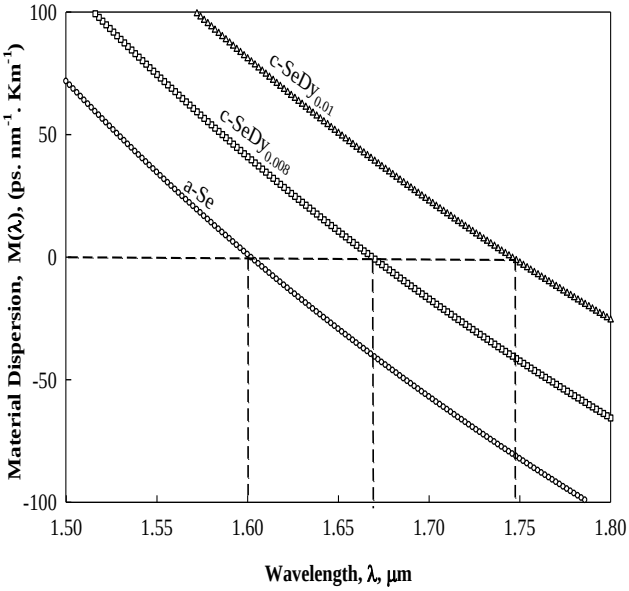

Figure 8. Variation of the material dispersion versus wavelength for the films investigated.

the pumping of optical signals in the Selenium chalcogenide fibers at zero dispersion wavelength (ZMD) could be tuned by increasing the doping ratio of Dy[30,31].

3.2 Non-Linear optical dispersion

The microscopic nonlinear properties of the chalcogenide semiconductors have been investigated through the determination of second-order refraction index, n_2 and nonlinear absorption coefficient β,

where n_2 and β are expressed as

$$n_t = n + n_2 I \quad (13)$$

and

$$\alpha(I) = \alpha + \beta I,$$

where I is the incident intensity, n_t is the total refractive index and n represents the weak-field refractive index (linear refractive index). The second-order index of refraction, n_2 is required for soliton propagation in the optical telecommunication fibers and used in all-optical switching schemes.

Boling *et al.*[32] derived a semi-empirical relation for predicting the second-order index of refraction, n_2, for semiconductors from the linear refractive index, n which has the simplest form:

$$n_2(\times 10^{-13} esu) = G\frac{n-1}{\nu_d^{5/4}} \quad (14)$$

where G is an empirical constant and G = 391[32]. Here ν_d is the Abbe dispersion number and is given by:

$$\nu_d = \frac{n_d - 1}{n_F - n_C} \quad (15)$$

where n_d, n_F, and n_C refer to refractive indices at 589.0, 486.1, and 656.3 nm respectively.

The two-photon absorption coefficient β is given by[33]:

$$\beta = \frac{KE_p^{1/2}F(2h\nu/E_g)}{n^2E_g^3} \quad (16)$$

where K is the material-independent constant given by

$$K = \frac{2^9\pi}{5}\frac{e^4}{c^2\sqrt{m_o^*}} \quad (17)$$

Here e and m_o^* are the electron charge and its effective mass, respectively. In our calculations, K = 3100 and E_p is related to the Kane momentum parameter, p, where $E_p = 2p^2m/h^2$ and m is the electron mass. F is a function that represents the dispersion of β with respect to the incident photon energy $h\nu$. This function depends upon the band structure and determines the energy states that are coupled. The function F can be evaluated from the relation[33]:

$$F(2h\nu/E_g) = \frac{[(2h\nu/E_g)-1]^{3/2}}{(2h\nu/E_g)^5} \quad (18)$$

The overall dispersion behavior of β, as shown in **Figure 9b** a ratio between the maximum nonlinear absorption coefficients of the two-photon absorption (TPA) to the optical bandgap energy equals 1.4 is observed for different chalcogenide compositions[34–40]. The maximum nonlinear absorption coefficient β for investigated films is given in **Table 3**. The dispersion of $n_2 = f(h\nu)$ is be plotted as shown in **Figure 9a**.

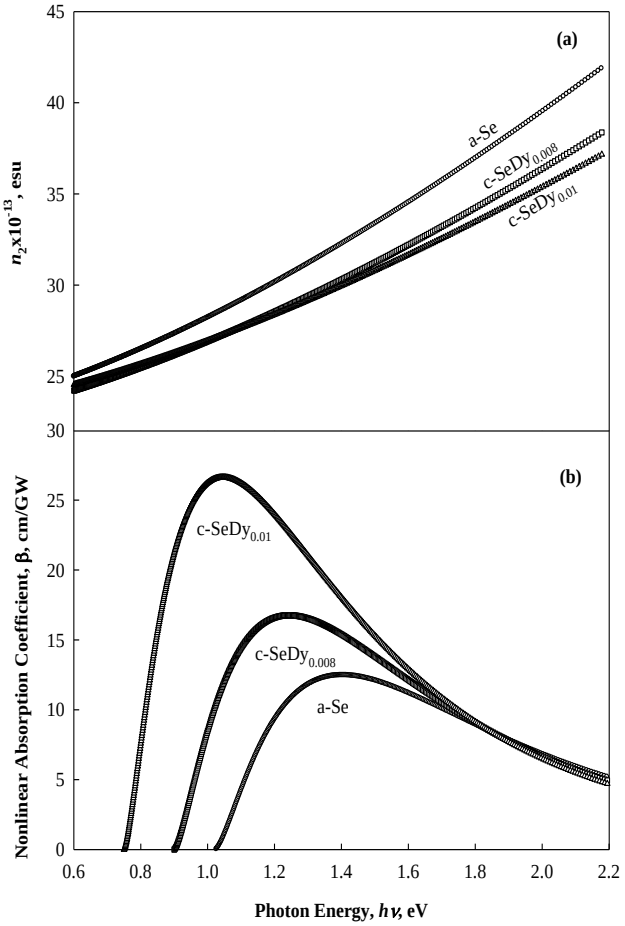

Figure 9. Dependence of second-order refractive index, n_2 (**a**) and nonlinear absorption coefficient, β (**b**) on the incident photon energy, $h\nu$ for the studied films.

Table 3. The nonlinear absorption coefficient, β_{max}, values of the energy corresponding to β_{max}, $E_{\beta = max}$, the ratio of $E_g/E_{\beta = max}$ for the studied samples

Film Composition	β_{max} cm/GW	$E_{\beta = max}$ eV	$E_g/E_{\beta = max}$
a-Se	13.6006	1.4739	1.42
c-SeDy$_{0.008}$	16.7625	1.3805	1.42
c-SeDy$_{0.01}$	26.631	1.1197	1.42

4. Conclusion

The study of the role played by dysprosium ions as a dopant in the structural network of a-Se on optical dispersion leads to draw the main following concluding remarks:

The optical band gap (E_g) decreases with an increase of the Dy content which is argued to be the difference in electronegativity between Se and Dy.

The variance between the values of the optical energy gaps of the studied samples and previously published data for other chalcogenide compositions doped also with Dy are attributed to the sensitivity of chalcogenides to its thermal history and preparation conditions.

The single oscillator energy, E_o, showed a decrease accompanied by an increase in the values of E_d. This trend of E_o and E_d shifted the material dispersion $M(\lambda)$ towards longer wavelengths from 1.6 to 1.74 nm against the increase in the Dy-content. This shift means that the material dispersion of chalcogenide fiber could be tuned by controlling the doping ratio of Dy.

A ratio between the maximum nonlinear absorption coefficients of TPA to the optical bandgap energy equals 1.4 is observed for different chalcogenide semiconductors.

Conflict of interest

The authors declare that they have no conflict of interest.

References

1. Yang Z, Chen W, Luo L. Dy^{3+}-doped Ge-Ga-Sb-Se glasses for 1.3 μm optical fiber amplifiers. Journal of Non-Crystalline Solids 2005; 351(30-32): 2513–2518.
2. Heo J. 1.3 μm-emission properties and local structure of Dy^{3+} in chalcohalide glasses. Comptes. Rendus Chimie 2002; 5(11): 739–749.
3. Hewak DW, Samson BN, Medeiros Neto JA, *et al*. Emission at 1.3 μm from dysprosium-doped Ga:La:S glass. Electronics Letters 1994; 30(12): 968–970.
4. Wei K, Machewirth DP, Wenzel J, *et al*. Spectroscopy of Dy^{3+} in Ge-Ga-S glass and its suitability for 1.3 μm fiber-optical amplifier applications. Optics. Letters 1994; 19(12): 904–906.
5. Tang G, Yang Z, Luo L, *et al*. Dy^{3+}-doped chalcohalide glass for 1.3-μm optical fiber amplifiers. Journal of Materials Research 2008; 23(4): 954–961.
6. Mott NF, Davis EA. Electronic Processes in Non-Crystalline Materials, 2nd ed. Oxford, New York: Oxford University Press; 1979.
7. Elliott SR. Physics of Amorphous Materials. 2nd ed. New York: Longmann Scientific & Technical; 1990.
8. Zakery A, Elliott SR. Optical Nonlinearities in chalcogenide glasses and their applications. NY: Springer Berlin Heidelberg; 2007.
9. Park BJ, Seo HS, Ahn JT, *et al*. Dy^{3+} doped Ge-Ga-Sb-Se glasses and optical fiber for the mid-IR gain media. Journal of the Ceramic Society of Japan 2008; 116(1358): 1087–1091.
10. Heo J. Rare-earth doped chalcogenide glasses for fiber-optic amplifiers. Journal of Non-Crystalline Solids 2003; 326 & 327: 410–415.
11. Shen Z, Li Y, Hu Q, *et al*. Dielectric properties of B–site charge balanced Dy–doped SrTiO ceramics for energy storage. Journal of Electroceramics 2015; 34: 236–240.
12. Abdel-Wahab FA, Maksoud HA. Electrical conduction and dielectric relaxation in selenium films doped with dysprosium rare earth. American Journal of Condensed Matter Physics 2017; 7(2): 41–49.
13. Pamuckchieva V, Szekeres A. Optical properties of $Ge_xSb_{20-x}Te_{80}$ thin films and their changes by light illumination. Optical Mater. 2008; 30(7): 1088–1092.
14. Boycheva S, Sytchkova AK, Bulir J, *et al*. Optical constants of As_2Se_3–Ag_4SSe–SnTe amorphous thin films. Journal of Non- Crystalline Solids 2007; 353: 1618–1623.
15. Swanepoel R. Determination of the thickness and optical constants of amorphous silicon. Journal of Physics. E: Scientific Instruments 1983; 16(12): 1214.
16. Swanepoel R. Determination of surface roughness and optical constants of inhomogeneous amorphous silicon films. Journal of Physics E: Scientific Instruments 1984; 17(10): 896.
17. Tang G, Yang ZY. Dy^{3+}-doped chalcohalide glass for 1.3-μm optical fiber amplifiers. Journal of Materials Research. 2008; 23(4): 954–961.
18. Nazabal V, Němec P, Jedelský J, *et al*. Dysprosium doped amorphous chalcogenide films prepared by pulsed laser deposition. Optical Materials 2006; 29(2-3): 273–278.
19. Tauc J, Grigorovici R, Vacu A. Optical Properties and Electronic Structure of Amorphous Germanium. Physica Status Solidi 1996; 15(2): 627–637.
20. Tauc J. Amorphous and Liquid Semiconductors. Plenum, New York; 1974.
21. Urbach F. The Long-Wavelength Edge of Photographic Sensitivity and of the Electronic Absorption of Solids. Physical Review 1953; 92: 1324–1325.
22. Redfield D. Energy-band tails and the optical absorption edge; the case of a-Si:H. Solid State Communications 1982; 44(9): 1347–1349.
23. Theye ML. Non-Crystalline semiconductor. Vol. 2, M. Pollak. CRC Press: 1987.
24. Moss TS, Burrell GJ, Ellis E. Semiconductor Opt-Electronics. London: Butterworths-Heinemann; 1973.
25. Wemple SH, DiDomenico M. Behavior of the electronic dielectric constant in covalent and ionic materials. Physical Review B 1971; 3(4): 1338–1351.
26. Wemple SH. Material dispersion in optical fibers.

Applied Optics 1979; 18(1): 31–35.
27. Poignant H. Dispersive and scattering properties of a ZrF4 based glass. Electronics Letters 1981; 17(25-26): 973–974.
28. Nassau K, Wemple SH. Material dispersion slope in optical fiber waveguides Electron. Electronics Letters 1982; 18(11): 450–451.
29. Boyd RW. Nonlinear Optics. 4th ed. Academic Press; 1992.
30. Klimczak M, Siwicki B, Skibinski P, *et al*. Coherent supercontinuum generation up to 2.3 μm in all-solid soft-glass photonic crystal fibers with flat all-normal dispersion. Optics Express 2014; 22(15): 18824–18832.
31. Lui L, Cheng T, Nagasaka K, *et al*. Coherent mid-infrared supercontinuum generation in all-solid chalcogenide microstructured fibers with all-normal dispersion. Optics Letters 2016; 41(2): 392–395.
32. Boling NL, Glass AJ, Owyoung A. Empirical relationships for predicting nonlinear refractive index changes in optical solids. IEEE Journal of Quantum. Electronics 1978; 14(8): 601–608.
33. Abdel-Wahab FA, El-Diasty F, Abdel-Baki M. Dispersion dependence of second-order refractive index and complex third-order optical susceptibility in oxide glasses. Physics Letters A 2009; 373(42): 3855–3860.
34. Quémarda C, Smektala F, Couderc V, *et al*. Chalcogenide glasses with high nonlinear optical properties for telecommunications. Journal of Physics and Chemistry of Solids 2001; 62(8): 1435–1440.
35. Smektala F, Quemard C, Leneindre L, *et al*. Chalcogenide glasses with large non-linear refractive indices. Journal of Non-Crystalline Solids 1998; 239(1-3): 139–142.
36. Rangel-Rojo R. Kimura K, Matsuda H, *et al*. Dispersion of the third-order nonlinearity of a metallo-organic compound. Optics Communications 2003; 228(1-3): 181–186.
37. Petit L, Carlie N, Villeneuve R, *et al*. Effect of the substitution of S for Se on the structure and non-linear optical properties of the glasses in the system $Ge_{0.18}Ga_{0.05}Sb_{0.07}S_{0.70-x}Se_x$. Journal of Non-Crystalline Solids 2006; 352(50-51): 5413–5420.
38. Zakery A, Elliott SR. Optical properties and applications of chalcogenide glasses: A review. Journal of Non-Crystalline Solids 2003; 330(1-3): 1–12.
39. Petkov K, Ewen PJS. Photoinduced changes in the linear and non-linear optical properties of chalcogenide glasses. Journal of Non-Crystalline Solids 1999; 249(2-3): 150–159.
40. Requejo-Isidro J, Mairaj AK, Pruneri V, *et al*. Selfrefractive non-linearities in chalcogenide based glasses. Journal of Non-Crystalline Solids 2003; 317(3): 241–246.

Applied Chemical Engineering (2021) Volume 4 Issue 1
doi:10.24294/ace.v4i1.735

ORIGINAL RESEARCH ARTICLE

Synthesis and characterization of polyurethane and its nanocomposite adhesive derived from biobased isocyanate and polyol

Swarnalata Sahoo[1,2*], Smita Mohanty[1,2], Sanjay Kumar Nayak[1,2]

[1] *Laboratory for Advanced research in polymeric materials (LARPM), CIPET, Bhubaneswar 751024, India. E-mail: sahoo.swarnalata@gmail.com*

[2] *Central institute of Plastic Engineering and Technology, Chennai 600032, India*

ABSTRACT

In the current research, the vegetable oil based polyurethane nanocomposite (PUNC) adhesive was prepared using transesterified castor oil (CO) based polyol, partially biobased aliphatic isocyanate (PBAI) and organically modified montmorillonite nanoclay (Closite 30B). The transesterified CO was synthesized by reacting CO with ethylene glycol, which was confirmed using proton nuclear magnetic resonance (^{1}HNMR) analysis. Further, the prepared polyurethane (PU) and its nanocomposite adhesive with specific NCO: OH molar ratio 1.3:1 was confirmed by Fourier transform infrared spectroscopy (FTIR) analysis. The increasing of wt% of nanoclay loading level up to 3% into PU matrix increased the lap shear strength of the adhesive systems. Subsequently, the effect of polyurethane nanocomposite adhesives on the bonding strength of wood-to-wood and aluminum-to-aluminum substrate was studied using lap shear strength test. The nanoclay was observed to effectively intercalate into the polymer matrix. Moreover, the phase separation in PU and PUNC adhesive was studied using atomic force microscope (AFM) and differential scanning calorimetry (DSC) analysis.

***Keywords*:** Castor Oil; Biobased Isocyanate; Nanoclay; AFM

ARTICLE INFO

Received: 17 April 2021
Accepted: 10 June 2021
Available online: 15 June 2021

1. Introduction

Polyurethane adhesive synthesis from renewable sources has been one of the major efforts recently being practised worldwide as an alternative to the petrochemical feedstock[1–7]. The vegetable oils such as castor oil, soybean oil[6], palm oil[7], sunflower oil, corn oil and linseed oil[8-10] have been used for the fabrication of polyurethane adhesive due to its cost effectiveness, low toxicity and health concern. Among these, castor oil (CO) offers a wide range of advantages for the formulation of polyurethane adhesive. Hence recent focus has been diverted to the castor oil based polyurethane adhesive due to the presence of a high percentage of ricinoleic acid, a monounsaturated, and 18carbon fatty acid in CO. Prior to the advantages of CO such as high reactivity, easy availability and non-toxicity, it was found to be a suitable backbone towards the development of PU adhesive. In general, castor oil contains 85–95% ricinoleic acid, 2–6% oleic acid, 1–5% linoleic acid, 0.5–1% alpha-lonoleic acid, 0.5–1% stearic acid, 0.5–1% palmitic acid, 0.3–0.5% dihydroxystearic acid and 0.2–0.5% other component. The direct utilization of CO in PU adhesive gives limited hardness and structural irregularity due to the presence of secondary hydroxyl groups in CO, which exhibits low rate of curing due to the steric hindrance formation during polyurethane formation. To overcome these limitations, chemical modifications on active sides via transesterification or transamidification has been adopted to utilize the double bond of unsaturated fatty acid and carboxylic group,

to increase its hydroxyl value for improving the cross linking density and rigidity of the polyurethane network. Now a day's moisture-cured polyurethane adhesive has been synthesized from castor oil because it has many potential advantages including shear strength, flexibility and reactivity, etc., which allows polymer materials to adhere on various moist substrates through the development of strong chemical bonds[9]. The performance of an adhesive is interrelated to its adhesion properties like viscoelastic properties, surface free energy and the adhered substrate[10].

Generally, polyurethane consists of macrodiol which may be polyester or polyether, isocyanate, catalyst and other chain extender[11]. Polyurethane is a two segmental structure based polymer, where a soft and hard domain produces phase separation. The phase separation is obtained due to low molecular weight of the polyol (soft domain)[12]. The isocyanate (hard domain) is the essential part required for PU synthesis. The isocyanates containing may be two or more–NCO groups per molecule. For the formulation of polyurethane adhesive, the used isocyanates can be synthetic (aliphatic, aromatic or cycloaliphatic) or biobased in nature[13]. To improve the limitations such as shorter gel time, low durability, deterioration in mechanical and thermal properties, methods have been analyzed with the incorporation of nanoclay within the PU matrix. Thus, the development of polyurethane adhesive with the incorporation of nanoclay has gained strong demand as these fillers are able to enhance physiochemical properties such as high adhesion strength as well as thermal stability of polyurethane nanocomposite adhesive[14]. However, very few literatures have been explained about the synthesis and utilization of polyurethane clay nanocomposite in adhesive technology[15–17].

The novelty of this work is the development of newly polyurethane-clay nanocomposite adhesive derived from the combination of biobased isocyanate and vegetable oil based polyol with the incorporation nanoclay (Closite 30B), which can be utilized as wood-wood bonding adhesive. However, several literatures have been reported for the development of petrobased polyurethane-clay nanocomposite adhesive[16,17].

Hence, in the current research work, the present investigation focused on the development of biobased polyurethane nanocomposite adhesive with the incorporation of nanoclay into the PU matrix. The authors have initiated to synthesize biobased polyurethane using biobased polyol and partially biobased aliphatic isocyanate. To observe the improved adhesion strength of PU adhesive on wood and aluminum substrate and their utilization in adhesive technology, lap shear test has been carried out. The phase separation structure in PU matrix has been studied in AFM analysis. Further, the phase separation in polyurethane adhesive was confirmed by DSC analysis.

2. Experimental procedure

2.1 Materials and methods

Ethylene glycol and castor oil were procured from M/s SD Fine chemicals, Kolkata. Partially biobased hexamethylene diisocyanate (Tolonate TM X FLO 100) was supplied by M/s Vencorex chemical, France. Dibutyl tin dialurate (DBTDL) was procured from M/s Sigma Aldrich, Germany. Analytical grade acetone and tetrahydrofuran (THF) were procured from M/s Fischer Scientific, USA. Closite 30B was supplied by Southern Clay Products, USA.

2.2 Polyurethane and its nanocomposite adhesive synthesis

The polyester polyol based polyurethane nanocomposite adhesive was prepared by two step method. In the first step, polyurethane adhesive was synthesized from modified castor oil with the addition of partially biobased aliphatic isocyanate. The castor oil was modified to obtain the polyester polyol using castor oil and ethylene glycol (EG) in the presence of lead oxide catalyst. The transesterification process of CO was performed to modify the CO under the nitrogen atmosphere to avoid oxidation reaction produced at the time of reaction. This process was carried out in a three necked round bottom flask of 250ml equipped with a magnetic stirrer, thermometer and reflux condenser with continuous stirring for 3 hr at 230 °C. The acid value of transesterified polyol was measured periodically using acetic anhydride method as described earlier[1]. Further, the synthesized polyol was dried under vacuum at 70 °C[12]. In the second step, the polyurethane nanocomposite

adhesive was prepared with the incorporation of nanoclay. Initially, the organically modified clay was dried for 5hr and the clay was separately mixed in THF solution with constant stirring. Then the clay was sonicated for 50min to minimize the agglomeration. After that, the solution was gradually added to the PU solution with continuous stirring of 15 min in the presence of N_2 gas environments. Then the formulated mixture was poured into the glass plate. The complete reaction mechanism is shown in **Figure 1.**

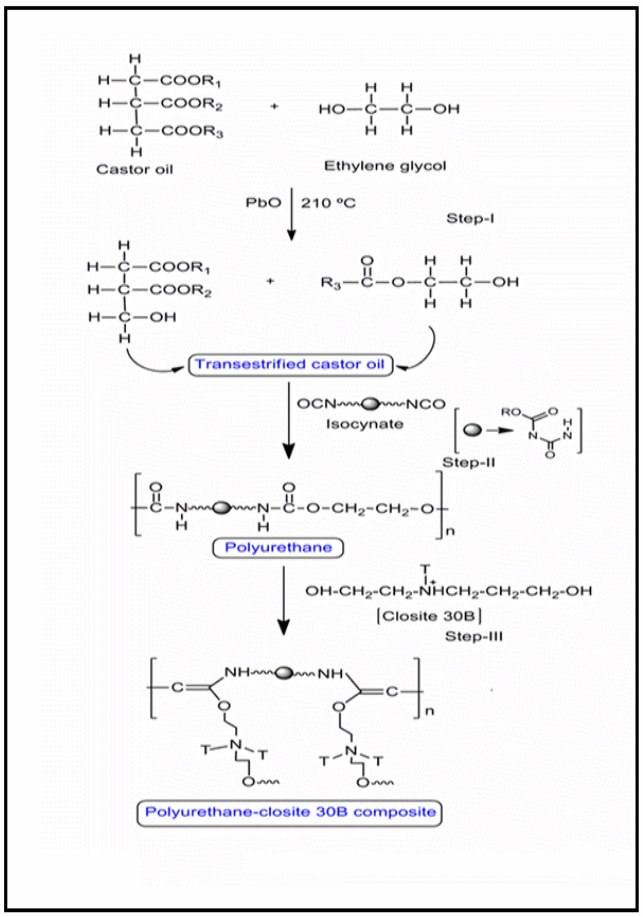

Figure 1. Synthesis mechanism of PU and PUNC adhesive.

3. Characterization

3.1 Proton nuclear magnetic resonance (^{1}HNMR) study

The ^{1}HNMR spectra of CO and transestrified castor oil based polyol were recorded by using JEOL DELTA2 500 MHz FX-1000 spectrometers (INSTROM). All measurements of chemical shift value were made using deuterated $CDCl_3$ solvent.

3.2 Fourier-transform infrared (FTIR) analysis

The spectra of polyurethane (PU) and polyurethane clay nanocomposite adhesive (PUNC) samples were analyzed by FTIR (Nicolet 6700, Thermo Scientific, USA) spectra. The FTIR analysis was carried out on each sample with 64 scans with the wavelength range of 400–4000 to cm^{-1}.

3.3 Lap shear test

The required specimen for lap shear test was prepared according to the standard ASTM D 906. The substrates were dried and polished with sandpaper of grit no. 60. The prepared adhesive solution (thickness 0.1mm) was applied on both pieces of the wood and aluminum substrates by using a brush on 25x30 mm^2 area of overlap. Over the contact area of wood pieces, a load having 2–3 kg has been applied and left overnight. After that, the specimen joints were kept at room temperature for 10 days. Then joint substrates were tested for measuring bonding strength by lap shear strength[18]. The shear strength bonded substrate joints were tested using a universal testing machine as per the standard ASTMD 906-82.

3.4 Wide angle X-ray diffraction (WAXD) analysis

Wide angle X-ray diffraction (WAXD) analysis was used to analyze the interlayer gallery spacing of nanoclays in the nanocomposites, using Philips X'Pert MPD (Japan), with graphite monochromator and a Cu Kα radiation source operated at 40 kv and 30 mA.

3.5 Atomic force microscope (AFM) analysis

Surface morphology and phase separation of PU and PUNC adhesive sample were recorded by using AFM (M/s. Park scientific instrument, XE-100, USA) in contact mode and a commercial probe was used at room temperature and moderate pressure.

3.6 Differential scanning calorimetry (DSC) analysis

The phase separation in PU and PUNC adhesive surface and the change in T_g values were evaluated using (DSC) Q20, M/s, TA Instrument, USA) at a temperature range of -100 °C to 100 °C at a heating 10 °C/min under N_2 atmosphere and a flow rate of 50 mL/min.

4. Result and discussions

4.1 Proton nuclear magnetic resonance (^{1}HNMR) study

^{1}HNMR spectra of castor oil (CO) and modified CO are represented in **Figure 2** which was described in our earlier research paper[1]. It is observed that the chemical shift δ values corresponding to 0.9 ppm and 2.3 ppm, is primarily due to methyl protons and the fatty acid proportion, respectively. Along with the above peak, the peak value δ at 4.0 attributed due to methylene protons of glycerol. The above peaks are always assumed as the reference because throughout the whole reaction the intensity of the above peak does not change. It is also observed that in CO and modified CO, the chemical shift δ values corresponding to 2.1-1.9, 1.5-1.75, 1.2-1.4 ppm, are mainly due to $–CH_2–CH=$, $CH_2–CH_2–O$ and aliphatic backbone respectively. The peaks at 3.6 and 4.1 ppm correspond to $–CH_2$ adjacent to secondary C, and $CH_2–O–C=O–$, respectively. The modification of CO is confirmed by the presence of chemical shift at δ values 3.7 and 3.8 ppm, which correspond to $–CH_2OH$ and –CHOH. Hence the modified polyol is confirmed through ^{1}HNMR.

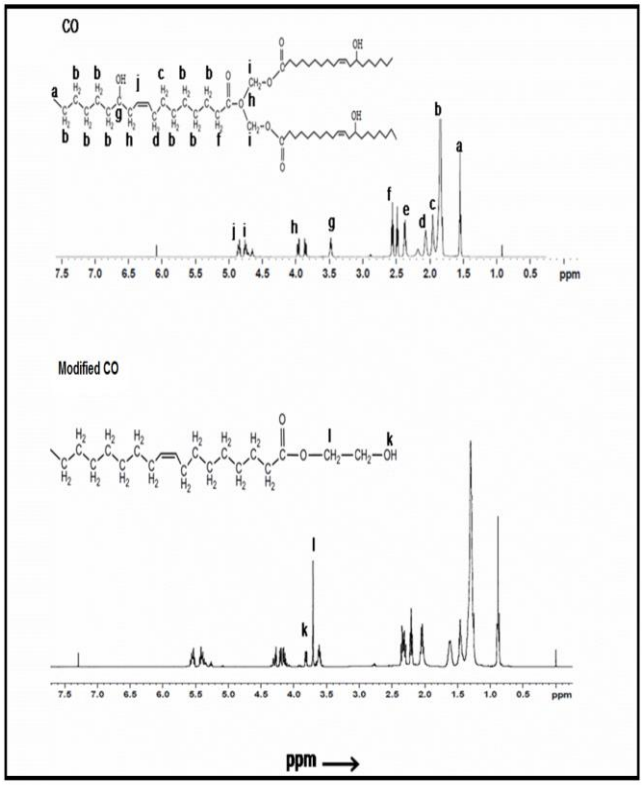

Figure 2. ^{1}HNMR spectra of CO and modified CO.

4.2 Fourier-transform infrared (FTIR) analysis

The IR spectra of PU and PUNC adhesive containing 3 wt% nanoclay were recorded in **Figure 3**. As evidenced from **Figure 3**, the characteristic absorption peaks were observed at 1050 cm^{-1} due to Si-O stretching vibration. However, marginal shifting of the peaks in PU was observed in presence of Closite 30B nanoclay due to strong intermolecular H-bonding between the hydroxyl group of C 30B and hard segment (-NH-) of polyurethane matrix[21]. The absorption peaks were observed at 3334 cm^{-1} due to the presence of urethane stretching. The absence of isocyanate peak at 2260 cm^{-1} indicated the completion of reaction between soft segment (OH group) and hard segment (NCO group) in both PU and PUNC adhesive. The band observed at 2923-2839 cm^{-1}, 1735 cm^{-1} and at 1237 cm^{-1} attributed due to $–CH_2$ stretching frequencies, carbonyl urethane stretching and coupled C-N and C-O stretching respectively. Hence, the above analysis showed similar IR spectra in PU and PUNC adhesive. No such differences in position of band assignments were observed in PU and PUNC adhesive, except only change in band intensity. This fact was obtained in accordance with the preparation of PUNC adhesive by other groups. But the band position of distinct functional group of the PU was identical to those of PUNC. This fact has also been reported by other researcher, which confirmed that the presence of silicate layers does not change the chemical structure of polyurethane[19]. To assure the chemical interaction between nanoclay and the individual components of polyurethane, the FTIR study confirmed the complete reaction obtained in PUNC surface.

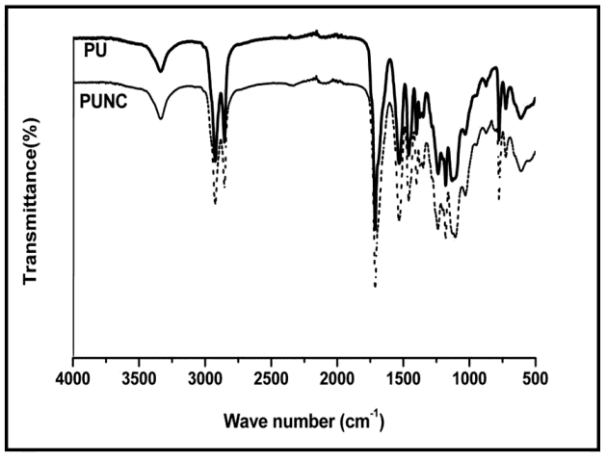

Figure 3. FTIR studies of PU and PUNC adhesive sample.

4.3 Lap shear test

The effect of PU matrix after the incorporation of 0 to 5wt % of nanoclay is depicted in **Figure 4** and the corresponding shear strength values are summarized in **Table 1**. The result showed the improvement of bonding strength with the increase in clay content. It is found that the integration of 3 wt % of nanoclay throughout the PU matrix showed higher bonding strength, which was taken as optimum composition. After that, the lap shear strengths of optimize PU and PUNC adhesive with respect to the substrates such as wood and aluminum (Al) respectively are depicted in **Table 2**. From the analytical observation, it has been found that the shear strength of PU adhesive for both the substrates increases with the increase in a span of days. The PU adhesive exhibited 40.23, 50.41, 69.20 and 69.22 (N/m^2x10^5) lap shear strength of wood-wood substrate after the period of 10, 20, 30 and 40 days respectively. Similarly, the lap shear strength of PU adhesive with respect to Al-Al substrate bonding exhibited 32.15, 44.32, 65.01 and 65.03 (N/m^2x10^5) after the period of 10, 20, 30 and 40 days. In the meantime, after the incorporation nanoclay throughout the PU matrix, the developed PUNC adhesive exhibited 72, 85, 103.07 and 103.09 (N/m^2x10^5) lap shear strength of wood-wood substrate after 10, 20, 30, and 40 days respectively, and 32.15, 44.32, 65.03 and 65.04 (N/m^2x10^5) lap shear strength of Al-Al substrate after the duration of 10 days, 20 days, 30 days and 40 days respectively. Hence it can be concluded that addition of 3wt % of clay content in PU matrix showed better adhesion strength over the neat PU. This might be due to the strong interfacial adhesion between the substrate and the adhesive. The failure process of joint bonding substrate was a cohesive failure, which confirmed the strong interfacial interaction between the adhesive and substrate[20,21]. This trend was in accordance with the strong interfacial interaction between the OH group of OMMT clay with the OH group in Al and OH group on wood substrate respectively. Further, it is noticed that, the shear strength of PU adhesive to hold the substrates increase up to 30 days, after that the shear strength for both substrates gradually leveled off. This result also indicated that higher shear strength in wood-wood substrate as compared to Al-Al substrate is due to the presence of high amount of polar hydroxyl group in wood substrate that produced strong interaction between wood substrate and adhesive. Hence, in the current study of view, wood substrates were chosen as the suitable substrate for PU and PUNC adhesive.

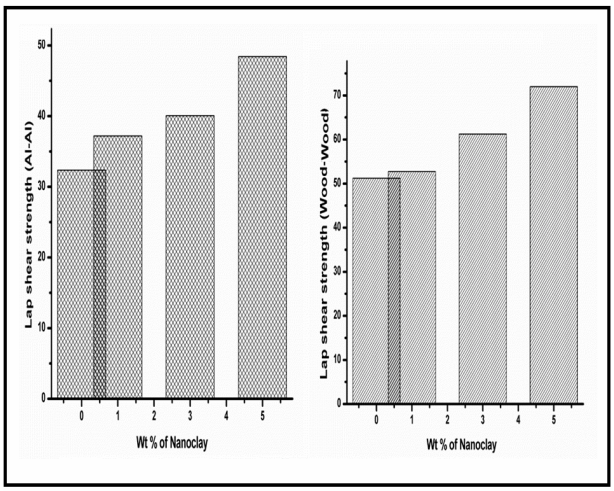

Figure 4. Lap shear strength of wood-wood bonding and Al-Al bonding substrate**.**

Table 1. Lap shear strength of substrates upon incorporation of different wt% of nanoclay

Sample code	Wood-Wood bonding strength of PUNC after 10 days (N/m^2x10^5)	Al-Al bonding strength of PUNC after 10 days (N/m^2x10^5)
0 wt% nanoclay	51.23	32.33
1 wt% nanoclay	52.75	37.21
3 wt% nanoclay	61.23	40.05
5 wt% nanoclay	72	48.44

Table 2. Comparison of lap shear strength between the substrates with PU and PUNC adhesive

No. of days	Wood-Wood Lap shear strength ($N/m^2x\ 10^5$)		Al-Al Lap shear strength ($N/m^2x\ 10^5$)	
	PU	PUNC	PU	PUNC
10 days	40.23	72	32.15	48.45
20 days	50.41	85	44.32	52.16
30 days	69.20	103.07	65.03	71.23
40 days	69.22	103.09	65.04	71.23

4.4 Wide angle X-ray diffractometer (WAXD) analysis

WAXD diffraction pattern was carried out in order to investigate the dispersion of OMMT clay throughout the PU matrix as represented in **Figure 5**. A strong diffraction peak was appeared at 2θ = 5.09º for OMMT nanoclay. The disappearance of this peak at 2θ = 5.09º in PUNC adhesive film confirming the strong interaction of clay and PU matrix. This indicated the increase in distance from a certain plane in one layer corresponding to another layer of the plane. Hence the diffraction was observed and the basal of the polymer can be calculated by using brags law d sin Θ = nλ. The diffraction peaks of all synthesized PU and PUNC adhesive films were found to be 20º whereas the corresponding basal spacing were 4.23 and 4.43 Å respectively, thereby indicating the increase in gallery height in PUNC adhesive film from PU adhesive film by 0.20 Å. Thus the higher value of basal spacing indicates that the silicate layers in polyurethane molecular chains are intercalated without exfoliation in the system. This indicated that the galleries of clay layers expanded in the PUNC sample[18]. In addition, the peak intensity of nanocomposite is lowered with the addition of nanoclay, which reveals that there is a homogenous dispersion of nanoclay within the PU matrix.

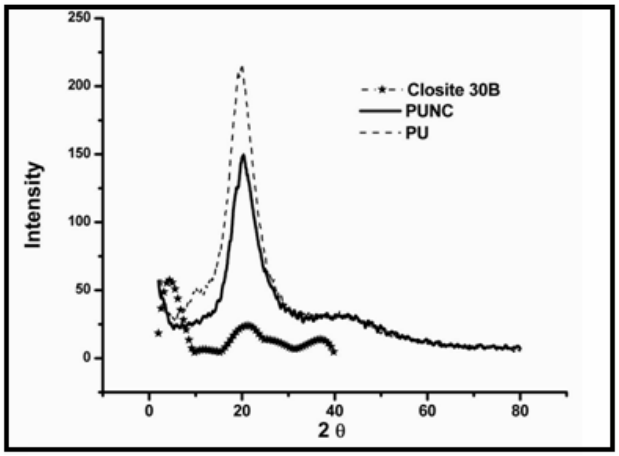

Figure 5. XRD analysis of PU and PUNC adhesive film.

4.5 Atomic force microscopy (AFM) analysis

The surface roughness at the nanometer level and phase morphology of PU and PUNC adhesive were studied using AFM non-contact mode represented in **Figure 6**. From the topographical images, it was observed that the phase separation obtained in the polyurethane due to the incompatibility of hard and soft domain. The higher degree of phase segregation was obtained after the incorporation of nanoclay (3 wt%) into the PU matrix. This can be attributed to the good interaction, such as H-bonding, polar-polar, etc. between the clay and hard domains of polyurethane (PU) adhesive film. Moreover, the degree of phase segregation was found to be 0.9° and 0.56° of PUNC and PU adhesive film respectively. Further, the brighter region indicates the isocyanate rich dispersed hard phase and the darker region indicates the polyol rich dispersed soft phase. Whereas, after the incorporation of nanoclay, it has been revealed the diameter of the hard segments was expanded[18]. From the topographical image in **Figure 6**, the average roughness (R_a) of PU and PUNC has been obtained to observe the structural changes in the surface. The surface roughness R_a of PU was found to be 19.42 nm whereas PUNC adhesive film exhibited 17.09 nm. The decrease in roughness and inhomogeneity in PUNC adhesive film was due to the addition of NC on PU matrix as a result of the good interaction between clay and PU[22–24].

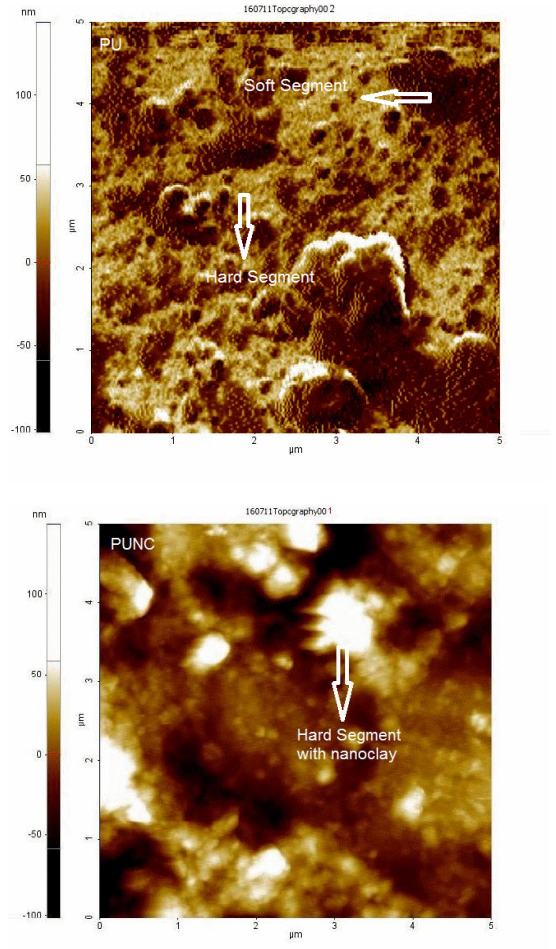

Figure 6. AFM analysis of PU and PUNC adhesive film.

4.6 Differential scanning calorimetry analysis (DSC)

Differential scanning calorimetry analysis (DSC) was performed to investigate the effect upon the addition of nanoclay into the PU adhesive reported in **Figure 7**. The analysis showed two step transitions due to the presence of two T_g values corresponding to the soft and hard segment. This indicates the occurrence of phase segregation on the structure of PU and PUNC adhesive. Hence, in phase segregation structure, the higher T_g value in PUNC restricts the polymer chain motion which induced due to higher crosslink density and an increase in free volume of the nanocomposites. The similar results have also been reported on the earlier research[25,26]. In addition, it has been observed that the T_g of soft segment and hard segment was shifted to higher temperature upon the loading of nanoclay on the PU matrix. The T_g values of soft segment corresponding to PU and PUNC were found to be -37.8 °C and -27.3 °C respectively. In the meantime, the T_g of hard segment corresponding to PU and PUNC was found to be 70 °C and 74.2 °C respectively. The above result indicated that, the PUNC exhibits higher T_g and cross linking density upon the incorporation of 3 wt% of nanoclay within the PU matrix. Further, in PUNC, the marginal increase in T_g value in hard segment and soft segment indicates the good interaction between the H-H bonding of PU and nanoclay.

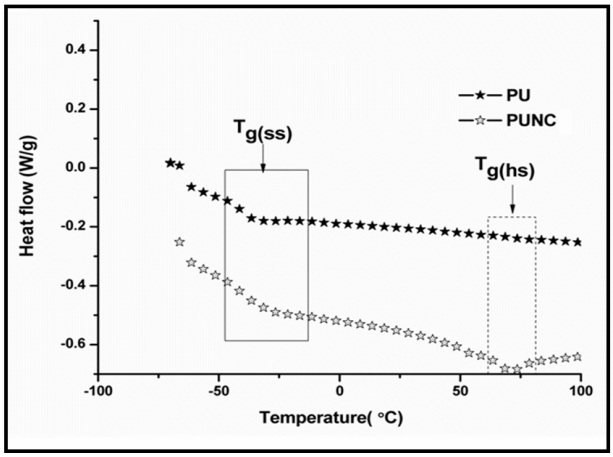

Figure 7. DSC analysis of PU and PUNC adhesive.

5. Conclusions

In the present work, a simple approach for the development of vegetable oil based PU and PUNC adhesive with the incorporation of nanoclay loading using in-situ polymerization method via ultrasonication technique have been reported. The developed adhesives were confirmed using FTIR analysis. The adhesive samples containing 3 wt% of nanoclay showed higher adhesion shear strength over the PU adhesive. Further, the adhesion strength of adhesive with respect to the wood substrate showed higher shear strength compared to Aluminum (Al) substrate. The dispersive characteristics of nanoclay into the PU matrix were confirmed by WAXD analysis and subsequently the formation of the phase separation structure was verified by AFM analysis. The analysis resulted that the nanoclay layers were well dispersed and the phase separation was prominently appeared on the surface of polyurethane. Further confirmation of phase separation was studied using DSC analysis. In the meanwhile, the shifting of peak temperature towards higher temperature was observed upon the incorporation of nanoclay within the PU matrix. From the above discussions, it can be concluded that the biobased PUNC adhesive synthesized from bio raw materials can be suitably used as a bioadhesive.

Conflict of interest

The authors declare that they have no conflict of interest.

References

1. Sahoo S, Kalita H, Mohanty S, *et al*. Synthesis of vegetable oil-based polyurethane: A study on curing kinetics behavior. International Journal Chemical Kinetics 2016; 48(10): 622–634.
2. Modesti M, Lorenzetti A, Simioni F, *et al*. Expandable graphite as an intumescent flame retardant in polyisocyanurate–polyurethane foams. Polymer Degradation and Stability 2002; 77(2): 195–202.
3. Weiss KD. Paint and coatings: A mature industry in transition. Progress in Polymer Science 1997; 22(2): 203–245.
4. Liu L, Qi Z, Zhu X. Studies on nylon 6/clay nanocomposites by melt-intercalation process. Journal of Applied Polymer Science 1999; 71: 1133–1138.
5. Campanella L, Bonnaillie M, Wool RP. Polyurethane foams from soyoil-based polyols. Journal of Applied Polymer Science 2009; 112(4): 2567–2578.
6. Miao S, Sun L, Wang P, *et al*. Soybean oil-based polyurethane networks as candidate biomaterials: Synthesis and biocompatibility. European Journal of Lipid Science and Technology (Special Issue: European Fed Lipid Highlights) 2012; 114(10): 1165–1174.

7. Kong XH, Yue J, Narine SS. Fatty acid-derived diisocyanate and biobased polyurethane produced from vegetable oil: Synthesis, polymerization, and characterization. Biomacromolecules 2009; 10(4): 884–891.
8. Chian KS, Gan LH. Development of a rigid polyurethane foam from palm oil. Journal of Applied Polymer Science 1998; 68(3): 509–515.
9. Tanaka R, Hirose S, Hatakeyama H, *et al*. Preparation and characterization of polyurethane foams using a palm oil-based polyol. Bioresource Technology2008; 99(9): 3810–3816.
10. Somani KP, Kansara SS, Patel NK, *et al*. Castor oil based polyurethane adhesives for wood-to-wood bonding. International Journal of Adhesion and Adhesives 2003; 23(4): 269–275.
11. Berezkin Y, Urick M. Modern polyurethanes: overview of structure property relationship. ACS Symposium Series 2013; 1148: 65–81.
12. Pratheep KA, Raghunatha RK, Sravendra R, *et al*. Synthesis, characterization, and performance evaluation of novel stabilized TDI-based polyurethane coatings under accelerated weathering. Journal of Vinyl & Additive Technology 2005; 11(1): 13–20.
13. El-Fattaha MA, El Saeed AM, Dardira MM, *et al*. Studying the effect of organo-modified nanoclay loading on the thermal stability, flame retardant, anti-corrosive and mechanical properties of polyurethane nanocomposite for surface coating. Progress in Organic Coatings 2015; 89: 212–219.
14. Hu Y, Song L, Xu J. Synthesis of polyurethane/clay intercalated nanocomposites. Colloid and Polymer Science 2001; 279: 819–822.
15. Nik Pauzi NNP, Majid RA, Dzulkifli MH, *et al*. Development of rigid bio-based polyurethane foam reinforced with nanoclay. Composites Part B: Engineering, 2014; 67: 521–526.
16. Zeng Q, Yu A, Lu G. Interfacial interactions and structure of polyurethane intercalated nanocomposite. Nanotechnology 2005; 16(12): 2757–2763.
17. Swain S, Sharma RA, Bhattacharya S, *et al*. Pegular papers: Effects of nano-silica/nano-alumina on mechanical and physical properties of polyurethane composites and coatings. Transactions on Electrical and Electronic Materials 2013; 14(1): 1–8.
18. Verma G, Kaushik A, Ghosh AK. Nano-interfaces between clay platelets and polyurethane hard segments in spray coated automotive nanocomposites. Progress in Organic Coatings 2016; 99: 282–294.
19. Patel S, Bandyopadhyay A, Ganguly A, *et al*. Synthesis and properties of nanocomposite adhesives. Journal of Adhesion Science and Technology 2006; 20(4): 371–385.
20. Chethana M, Madhukar BS, Siddaramaiah SR. Structure–property relationship of biobased polyurethanes obtained from mixture of naturally occurring vegetable oils. Advances in Polymer Technology 2014; 33(1): 21390.
21. Kong X, Narine SS. Physical properties of polyurethane plastic sheets produced from polyols from canola oil. Biomacromolecules 2007; 8(7): 2203–2209.
22. Lan Q, Haugstad G. Characterization of polymer morphology in polyurethane foams using atomic force microscopy. Journal of Applied Polymer Science 2011; 121(5): 2644–2651.
23. Dekaa H, Karak N. Bio-based hyperbranched polyurethane/clay nanocomposites: adhesive, mechanical, and thermal properties. Polymers for Advanced Technologies 2011; 22(6): 973–980.
24. Maiti M, Bhowmick AK. New insights into rubber–clay nanocomposites by AFM imaging. Polymer 2006; 47(17): 6156–6166.
25. Pedrazzoli D, Manas-Zloczower I. Understanding phase separation and morphology in thermoplastic polyurethanes nanocomposites. Polymer 2016; 90: 256–263.
26. Wang L, He X, Wilkie CA. The utility of nanocomposites in fire retardancy. Materials 2010; 3(9): 4580–4606.

Applied Chemical Engineering (2021) Volume 4 Issue 1
doi:10.24294/ace.v4i1.747

ORIGINAL RESEARCH ARTICLE

Polyaniline modified silica gel coupled with green solvent as eco favourable mobile phase in thin layer chromatographic analysis of organic dyes

Mahfoozurrahman Khan[1*], Ali Mohammad[2], Qasim Ullah[2], Faiz Mohammad[1]

[1] *Department of Applied Chemistry, Faculty of Engineering and Technology, Aligarh Muslim University, Aligarh 202002, India. E-mail: mahfooz55@gmail.com*

[2] *Department of Chemistry, School of Sciences, Maulana Azad National Urdu University, Hyderabad 500032, India*

ABSTRACT

This article studies a new green eco-friendly TLC (thin layer chromatography) using silica gel and polyaniline modified silica gel as stationary phase in combination with ethyl acetate (EA), n-butyl acetate (BA) and butane-1-ol (BO) solutions as mobile phase for the comparative study of migration behaviour of organic dyes to identify the most suitable thin layer chromatographic system for the resolution of co-existing dyes. Better separation efficiency was observed by modifying silica gel with polyaniline as compared to pure silica stationary phase. Densitogrpahic presentation of separations achieved on polyaniline modified silica gel Pani@SG-EB1 was also presented. The thin layer chromatographic system comprising of polyaniline modified silica gel Pani@SG-EB1 as stationary phase and n-butyl acetate:DDW, 5:5 as green mobile phase was observed to be the most favourable for the separation of various combinations of three or four-component mixtures of organic dyes viz. methyl thymol blue, tartrazine, carmoisine, rose bengal, amidoblack 10B, bromopyrogallol red and 4-nitrobenzene dizonium tetrafluoroborate. The effect of presence of cations and anions on separation trend was also examined and the limits of detection of the separated organic dyes were estimated. Fourier transform infrared spectroscopy (FTIR), x-ray diffraction (XRD), scanning electron microscopy (SEM) and transmission electron micrograph (TEM) studies were undertaken to characterize silica gel and modified silica gel (stationary phase). The developed method has been successfully applied for the identification of carmoisine in Solvin cold DS syrup and tartrazine in MefastTM syrup.

Keywords: Organic Dyes; Modified Silica Gel; Densitometry; Pharmaceutical Syrup; Thin Layer Chromatography

ARTICLE INFO

Received: 15 April 2019
Accepted: 16 May 2019
Available online: 23 May 2019

1. Introduction

Organic dye is a colour substance that has always attracted the person due to its attractiveness. Food colours are usually added to various commercial food products in order to make them more attractive and to achieve the desired colour. Food colours can be divided into four categories: natural, nature-identical, inorganic and synthetic[1]. For safety reasons there have been recent reductions in the number of permitted food colours but they are still being used all over the world because of their low price, effectiveness and stability. Moreover, the food processing industry uses all types of food colours, but to minimise potential toxicity the amounts of permitted synthetic colours used are strictly limited[2,3].

Synthetic dyes are widely used for improving the colour and enhancing the visual aesthetic appeal of some foods, and this effect is maintained throughout the production process and during storage. They present high stability to light, oxygen, and pH changes, and have lower

prices compared to natural dyes[4,5]. Synthetic dyes can be classified into water soluble and fat soluble. Only water soluble dyes are permitted in foods. Some of the most commonly used are sunset yellow (E110), allura red (E129), brilliant blue (E133), erythrosine (E127), tartrazine (E102), amaranth red (E123), carmoisine, ponceau 4R (E124), and others. They are present in soft drinks, gelatins, snacks, yoghurts, ice cream, candies, puddings, chips, pickles, honey, mustard, gum, baked goods etc.

However, these dyes must be controlled because many of them have been related to health problems. It was observed that synthetic dyes present in foods may cause overactive behaviour in children, especially if they are consumed in excess. On the other hand, some dyes in the presence of analgesics like aspirin can induce allergic or asthmatic problems. Tartrazine and sunset yellow second and third most widely used food dyes, added to many food[6-8].

Dyes are very important in so many areas such as printings, paintings, textiles, cosmetics, pictures, food and screens[9–12]. Food dye additives are defined as dyes, pigments, or substances that impart colors into foods, drugs, or cosmetics. Originally, natural dyes present in foods are unstable and altered rapidly during food processing and storage. Hence, synthetic dyes that outperform natural ones at various aspects such as low price, high effectiveness, and excellent stability are widely used by food companies all over the world[13,14].

Many analytical methods for the determination of dyes have been reported, such as thin layer chromatography (TLC)[15–17], titrimetry[18], voltammetry[19,20], polarography[21], spectrophotometry, 12[22,23] high-performance liquid chromatography (HPLC) [24–26], capillary electrophoresis (CE)[27–29], ion chromatography[30], voltammetry, polarography, spectrophotometry and thin layer chromatography are simple and time saving methods been proposed.

Among all these techniques, thin layer chromatography (TLC) is one of the most cheapest, quickest and most versatile for the separation and identification of organics and inorganics chemical compounds for many applications like bio-medical and pharmaceutical field including dyes industries[31–33].

In the current study, silica gel and polyaniline modified silica gel layer has been used as stationary phase in combination of DDW, ethyl acetate (EA), n-butyl acetate (BA) and butane-1-ol (BO) as green mobile phase. Polymer modified silica gel enhances the selectivity and chemical stability of the stationary phases. Ethyl acetate, n-butyl acetate and butane-1-ol solvent have been used in TLC as a green solvent due to their versatility and environmental benefits[34]. The coupling of favourable properties of polyaniline (Pani) (e.g. good environmental stability, high electrical conductivity, electrochromism, reversible transformation of various oxidation states, catalytic, antistatic and anticorrosion activity) and silica gel (good heat resistance, high tensile strength, and hardness) together provide new stationary phase of improved structural and chromatographic characteristics[35,36].

In the current study, the polyaniline modified silica gel stationary phase Pani@SG-EB_1 = S_2 has been prepared by in situ oxidative polymerization of aniline to be used as stationary phase with several mobile phase for thin layer chromatographic analysis of seven organic dyes viz. tartrazine; carmoisine; rose bengal; amidoblack 10B; methyl thymol blue; bromopyrogallol red and 4-nitrobenzene dizonium tetrafluoroborate. Chromatographic parameters have been calculated for quaternary separations of organic dyes on Pani@SG-EB_1 = S_2 stationary phase in the presence of M_6 (n-butyl acetate:DDW, 5:5 by volume) as mobile phase. The use of green mobile phase as well as polyaniline modified silica gel as stationary phase is a novel approach to develop environmental friendly green TLC method. Thus prepared Pani@(SG)EB_1 = S_2 stationary phase has also been characterized by Fourier transform infrared (FTIR), X-ray diffraction (XRD), scanning electron microscopy (SEM) and transmission electron micrograph (TEM).

2. Materials and method

2.1 Apparatus

Glass plates (20 cm × 3.5 cm) coated with silica gel and polyaniline modified silica gel using TLC applicator (Toshniwal, India) were used as stationary phase. The micropipette (Tripette, Germany) was used for spotting of analytes and glass jars (24 cm × 6 cm) were used to perform TLC.

2.2 Experimental temperature

All the experiments were performed at 25 ± 2 ^{o}C.

2.3 Chemicals and instrumentation

Silica gel (Fischer Scientific, India), methanol, ethanol, propanol-1, potassium persulphate, copper sulphate, zinc sulphate, manganese sulphate, nickel nitrate, HCl, n-butyl acetate and sodium salts of bromide, chloride, carbonate, acetate and nitrate (CDH, India); ethyl acetate, butane-1-ol (Fisher Scientific) and aniline (E-Merck India Ltd.) were used as received. All chemicals were of Analytical Reagent grade. The water used in these experiments was double distilled.

The fourier transform infrared spectra (FTIR) was recorded using Perkin-Elmer 1725 spectrometer operating in the 400-4000 cm^{-1} range. X-ray diffraction (XRD) data were recorded by using Bruker D8 diffractometer with Cu Kα radiation at 1.540 Å in the range of $5^{o} \leq 2\theta \leq 70^{o}$ at 40 kV. The morphology was observed by a JSM-6510LV system with a JEOL scanning electron microscope (SEM). Transmission electron micrograph (TEM) was done with the help of JEM 2100, JEOL.

2.4 Dyes studied

Tartrazine and carmoisine (Roha Dyechem Pvt. Ltd., Mumbai, India), rose bengal (SD fine chemical), amidoblack 10B (CDH, India), methyl thymol blue (Merck), bromopyrogallol red (CDH, India) and 4-nitrobenzene dizonium tetrafluoroborate (Spectrochem, Pvt. Ltd. Bombay, India) were used.

2.5 Test solutions

Solutions 5 % (w/v, g/mL) of dyes were prepared in double distilled water (DDW).

2.6 Stationary phase

SG = S_1, Pani@SG-EB_1 = S_2 and Pani@SG-EB_2 = S_3 were used as stationary phase.

2.7 Mobile phase

Solvent systems used as mobile phase are listed in **Table 1**.

2.8 Composition of Mefast™ P syrup and Solvin cold DS syrup

The Mefast™ P syrup from Zuventus Health Care Ltd. (A joint venture of Emcure® Chandival Andheri (E), Mumbai, India) and Solvin cold DS syrup from Ipca Laboratories Ltd. (Selaqui, Dehradun; Regd. Off. 48 Kandivali, Mumbai, India) were studies to identify tartrazine and carmoisine organic dyes respectively. The pharmaceutical formulation of Mefast™ P syrup contains mafenamic acid suspension IP 50 mg, paracetamol IP 125 mg and colouring agent tartrazine. The pharmaceutical formulation of Solvin cold DS contains paracetamol IP 250 mg, phenylephrine hydrochloride IP 5 mg, chlorpheniramine maleate IP 2 mg and colouring agent carmoisine.

Table 1. The composition details of mobile phases

Mobile Phase Code	Mobile Phase
M_1	Double distilled water (DDW)
M_2	Ethyl acetate (EA)
M_3	n-Butyl acetate (BA)
M_4	Butane-1-ol (BO)
M_5	Ethyl acetate : DDW (5:5)
M_6	n-Butyl acetate : DDW (5:5)
M_7	Butane-1-ol : DDW (5:5)
M_8	Ethyl acetate : DDW (6:4)
M_9	n-Butyl acetate : DDW (6:4)
M_{10}	Butane-1-ol : DDW (6:4)
M_{11}	Ethyl acetate : DDW (4:6)
M_{12}	n-Butyl acetate : DDW (4:6)
M_{13}	Butane-1-ol : DDW (4:6)

2.9 Characterization

2.9.1 FTIR spectroscopic studies

The FTIR spectra of silica gel (SG) and Pani@SG-EB_1 stationary phases are shown in **Figure 1**. The main characteristic peaks of silica gel in curve are broad absorption band around 3462 cm^{-1} corresponds to Si-OH stretching vibrations, 1636 cm^{-1} for the Si-OH bending mode of vibration, the strong absorption band at 1099 cm^{-1} due to the asymmetric

stretching vibration of Si–O–Si bond because of the formation of SiO_2 network, the absorption peak at 795 cm^{-1} represents Si-O-Si bending vibration[37-39].

In the case of Pani@SG-EB_1 stationary phases apart from the peaks of SG, the characteristic peak of 3454 cm^{-1} due to the free (non-hydrogen bonded) N-H stretching vibration is present, confirming the presence of Pani in Pani@SG[40,41]. 1643 cm^{-1} for the Si-OH bending mode of vibration, the strong absorption band at around 1087 cm^{-1} due to the asymmetric stretching vibration of Si–O–Si bond. Thus, it can be inferred that the incorporation of SG does not damage the backbone of Pani. It was observed that aromatic groups grafted onto the silica gel surface can be identified by their characteristic bands, which are distinguishable from those of the linear chain intermediate. A qualitative analysis of the organic groups immobilized on the silica gel surface can be carried out based on the very similar spectra of pure and supported aromatic groups.

2.9.2 X-Ray diffraction (XRD) studies

The x-ray diffraction patterns of silica gel and Pani@SG-EB_1 stationary phases are presented in **Figure 2**. It can be seen clearly that the silica retains a broad diffraction peak at about 22.3°, indicating that the silica is amorphous nature. Likewise, the diffraction peak of Pani@SG-EB_1 did not have an apparent shift[42–44]. However, there is no diffraction peak of Pani emerging in the patterns of Pani@SG-EB_1, confirming that the Pani is also amorphous and has been encapsulated in the pores and channels of the silica.

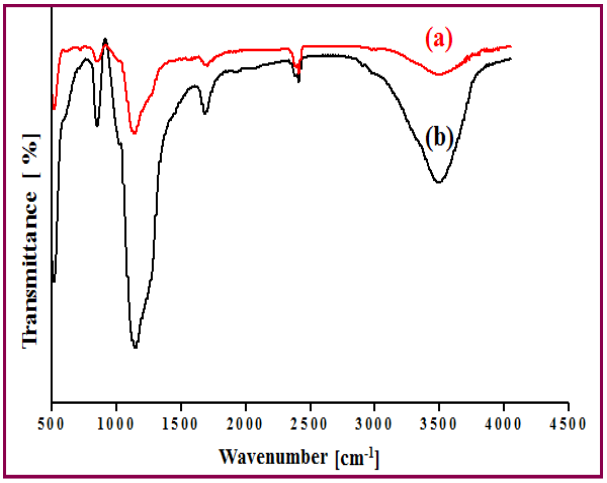

Figure 1. FTIR spectra of: (a) Pani@SG-EB_1 = S_2 and (b) silica gel = S_1 stationary phases.

2.9.3 Scanning electron micrographic (SEM) studies

The shape and surface morphologies of silica gel and Pani@SG-EB_1 stationary phases have been demonstrated in **Figure 3** (a-b). SEM images of silica nanoparticles shown in **Figure 3** (a) are irregular, porous and few are spheroidal shape with relatively smooth surface. In **Figure 3** (b), Pani@SG-EB_1 show rougher surface probably due to the polymerization of aniline on the surface of silica gel and porosity may increase due to presence of polyaniline[45,46]. However, both the micrographs are relatively similar and SiO_2 are mechanically very strong and not very distinct. The aniline has polymerized on the surface of silica gelas is evident from the FTIR analysis.

2.9.4 Transmission electron micrographic (TEM) studies

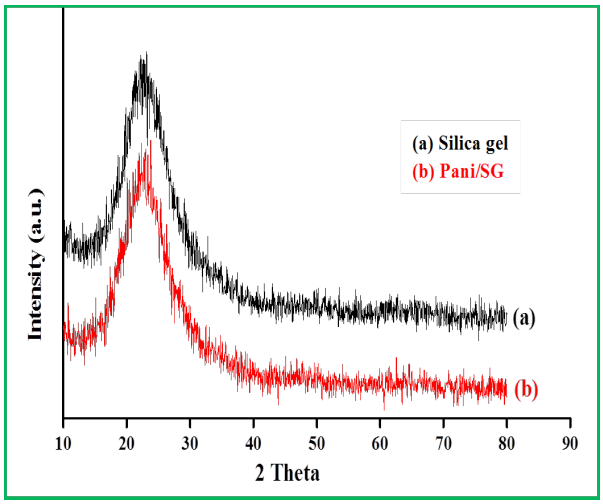

Figure 2. XRD spectra of: (a) silica gel = S_1 and (b) Pani@SG-EB_1 = S_2 stationary phases.

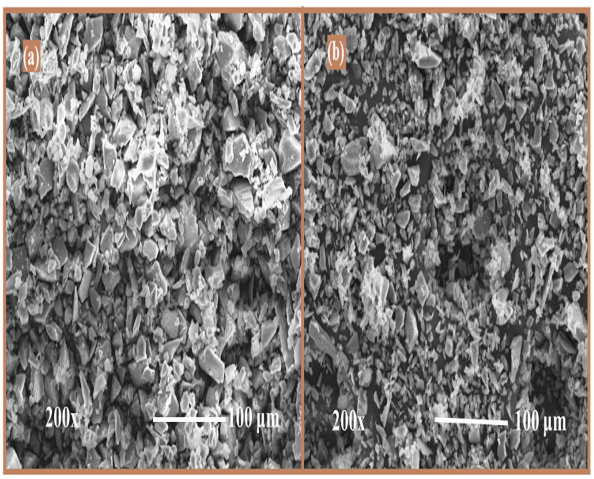

Figure 3. SEM micrographs of (a) silica gel = S_1 and (b) Pani@SG-EB_1 = S_2 stationary phases.

Silica gel and Pani@SG-EB_1 stationary phase were characterized to identify size and shape of their particles by TEM studies as shown in **Figure 4**. Most of the silica gel particles were spheroidal or ellipsoidal with particle size ranging between 8–13 nm. However, some irregular particles were also observed[47]. In case of Pani@SG-EB_1 stationary phases, it appears that the Pani undergoes polymerization on the surface of silica gel leading to the formation of interconnected tubular and fibrous nanostructures containing silica gel in the core. However, the SG surfaces became rough and a large amount of amorphous films or particles were observed, indicating the formation of Pani over SG and thickness size range was 18-35 nm. Thus, the material particles belong to the nano size. The Pani is tightly bound to silica gel which is beneficial for its use in electronic and separation technique[48].

2.10 Preparation of polyaniline modified silica gel stationary phase

Polyaniline modified silica gel stationary phases were prepared by simple in-situ oxidative polymerization of aniline using potassium persulfate as an oxidizing agent in presence of different amounts of SG. Aniline (1 mL) was dissolved in 200 mL of aqueous solution of HCl (1M). Different amounts of silica gel were added in aniline solution. Later, potassium persulphate (5 g), dissolved in HCl (1M) was added drop-wise in the aniline solution for the polymerization. The reaction mixture was put under continuous stirring for 22 h. The resultant mixture containing emeraldine salt turned slowly into greenish black slurry which was filtered, washed thoroughly with DDW and undoped with 500 mL of 1M ammonia solution for making Pani@SG-EB. The resultant product washed with DDW and methanol to remove the impurities until filtrate became neutral and colourless. The prepared nanocomposites were dried at 70–80°C for 12 h in an air oven, converted into fine powders and were stored in a desiccator for further investigations as shown in **Table 2**.

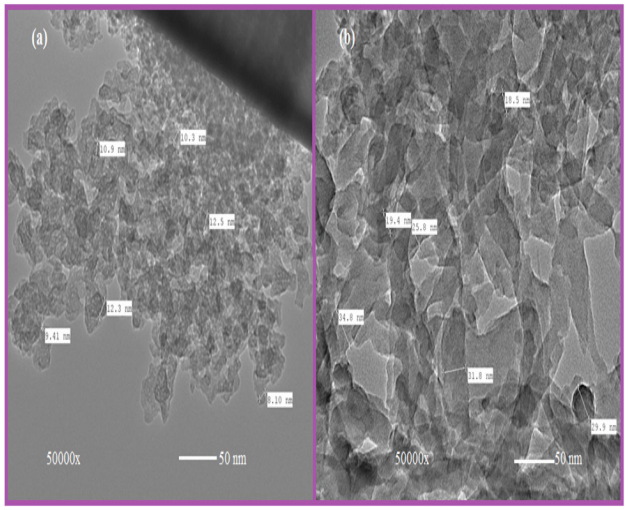

Figure 4. TEM micrographs of (a) silica gel = S_1 and (b) Pani@SG-EB_1 = S_2 stationary phases.

2.11 Thin layer chromatography

The preparation of TLC plates and chromatographic procedure were followed as reported earlier[49]. Aliquots (0.1 µL) of dyes were spotted on prepared TLC plates (S_1, S_2 and S_3) and the plates were developed with different mobile phases (M_1-M_{13}). After development, spots were visualised and the R_F values were calculated for individual dyes. For mutual separations of dyes, equal volumes (1 mL each) of dyes (Tartrazine, carmoisine, rose Bengal, amidoblack 10B, methyl thymol blue, bromopyrogallol red and 4-nitrobenzene dizonium tetrafluoroborate) were mixed and 0.1 µL of the resultant mixture was spotted on the TLC plates. The plates were developed with selected mobile phase (M_6) and static phase (S_2), and the spots were detected and the R_F values of the separated dyes were determined. The R_F values were calculated from the R_L (R_F of leading front) and R_T (R_F of trailing front) values of the spot as given below.

$$R_F = 0.5\ (R_L - R_T) \quad (1)$$

For the separation of dyes mixture, an equal volume of each dye were mixed and 0.1 µL of the resultant mixture was applied onto the TLC plates of silica gel or polyaniline modified silica gel. The TLC plates were developed with different mobile phases, the spots were detected, the R_F values were

Table 2. Preparation details of Pani@SG stationary phases

Mobile Phase Code	Volume of Aniline (mL)	Weight of $K_2S_2O_8$ (g)	Weight of Silica Gel (SG) (g)
Pani@SG-EB_1 = S_1	1.0	5.0	30.0
Pani@SG-EB_2 = S_2	1.0	5.0	60.0

determined and other studies were carried out on the separated spots of the dyes.

2.12 Separation

For the separation of the organic dyes mixtures, an equal volume of each organic dyes were mixed and 1 µL of the resultant mixture was applied onto TLC plate. The plate was developed with M_6 (n-butyl acetate, DDW, 5:5) by volume), the spots were detected and the R_F values of the separated spots of the organic dyes were calculated.

2.13 Ageing effect of mobile phase

To examine the ageing effect (stability) of mobile phase (M_6) on the separation of organic acids, the sample mixture was spotted on the activated Pani@SG-EB_1 TLC plates, developed with freshly prepared mobile phase (M_6) and the R_F values were calculated. The same process was repeated using previously prepared mobile phase (M_6) at different intervals of time for 24 h. Later on the R_F values were calculated and compared with the values obtained with the use of freshly prepared mobile phase.

2.14 Effect of foreign substances

For investigating the interference of metal cations and inorganic anions as impurities on the separation of the mixture, 0.1 µL of the standard test mixture of dyes solutions were spotted on the S_2 TLC plate followed by spotting of 0.1 µL of the metal cations or inorganic anions being considered as impurities. The plates were developed with M_6, detected and the R_F values of the separated dyes were calculated.

2.15 Limits of detection

The detection limits of the dyes were determined by spotting 0.1 µL of tartrazine, carmoisine, rose bengal, amidoblack 10B, methyl thymol blue, bromopyrogallol red and 4-nitrobenzene dizonium tetrafluoroborate of different concentrations on the S_2 stationary phase. TLC plates which were developed with the selected mobile phase M_6 and the spots were visualized. This process was repeated by successive reduction of the concentration of dye until the detection of dye was not possible anymore. The amount of dye just detectable was taken as the detection limit.

3 Results and discussion

SG was modified by in-situ oxidative polymerization of aniline. Separations of mixture of organic dyes (tartrazine; carmoisine; rose bengal; amidoblack 10B; methyl thymol blue; bromopyrogallol red and 4-nitrobenzene dizonium tetrafluoroborate was performed on three different stationary phases silica gel = S_1, Pani@SG-EB_1 = S_2 and Pani@SG-EB_2 = S_3 with thirteen different mobile phases of eco-friendly green organic solvent for obtaining a novel TLC system for the separation of dyes from their mixtures. Polyaniline modifies silica gel show more proficiently separation in comparison to SG. It can be understood that on modification of silica surface, there is a partial conversion of surface silanol groups to new organo-functional groups imparting considerably different set of properties to the surface than the original matrix[50].

3.1 Pani@SG stationary phases

SG was modified by in-situ oxidative polymerization of aniline over it. Separations of mixture of organic dyes were more efficiently achieved on Pani@SG in comparison to SG. It may be understood that on modification of silica gel surface, there is a partial conversion of surface silanol groups to new organo-functional groups imparting considerably different set of properties to the SG surface[50] (**Figure 5**).

Thus, after modification of SG with Pani, both the positive and negative centers are developed on the stationary phases which are capable to selectively interact with the dyes in the mixture. The polarons of Pani interact with the oxygen atoms of the silanol groups via electrostatic interaction giving rise to a new organo-functional group with both positive and negative centers[51]. In aqueous medium, dyes molecule bears both positively and negatively charged centers along with other groups and hence can interact with the organo-functional groups of the stationary phase via electrostatic interaction. However, different dyes interact differently depending on their molecular structure. This difference in mobility due to different types of interactions of different dyes with organo-functional group of sta-

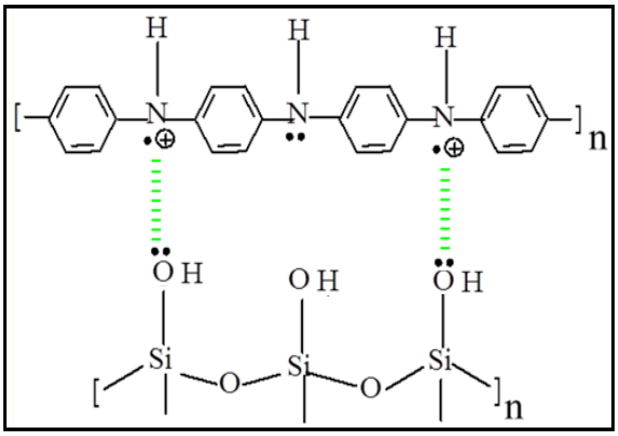

Figure 5. Schematic presentation of interaction between Pani and silica gel Pani@SG stationary phase.

tionary phase eventually leads to their separation.

Due to the polar nature of stationary phase, mobile phase and dyes molecules, electrostatic interactions between the anionic dye and the polymer, hydrogen bonding (between H, O and N atoms in dye molecule and N and H atoms in polymer), van der Waals forces (between the aromatic nature of polymeric matrix and the aromatic rings of the dye) are responsible for differential migration of dyes which eventually led to their separations. In the present case, 4-nitrobenzene dizonium tetrafluoroborate and methyl thymol blue are strongly retained by the stationary phase exhibiting very low R_F value (R_F ranges 0.05–0.06). It appears that steric hindrance due their bulkiness plays dominant role in case of MT to reduce the mobility of the dyes besides the strong electrostatic interaction between the dyes and stationary phase S_2.

In case of bromopyrogallol red, the steric hindrance is lesser than that in NT and MT therefore the mobility (R_F = 0.22) of this dye, while in case of rose bengal dye the steric hindrance and electrostatic interactions are less and therefore its R_F (0.40) is greater than other four dyes leading to a very good separation from others.

But in case of tartrazine and carmoisine dyes, the steric hindrance and electrostatic interactions are minimal and therefore R_F values are 0.95 and 0.70 respectively, which are greater than all other dyes leading to a very good separation from others. The chemical structures of dyes under study are illustrated in **Figure 6**.

Thin layer chromatography of dyes (tartrazine, carmoisine, rose bengal, amidoblack 10B, methyl

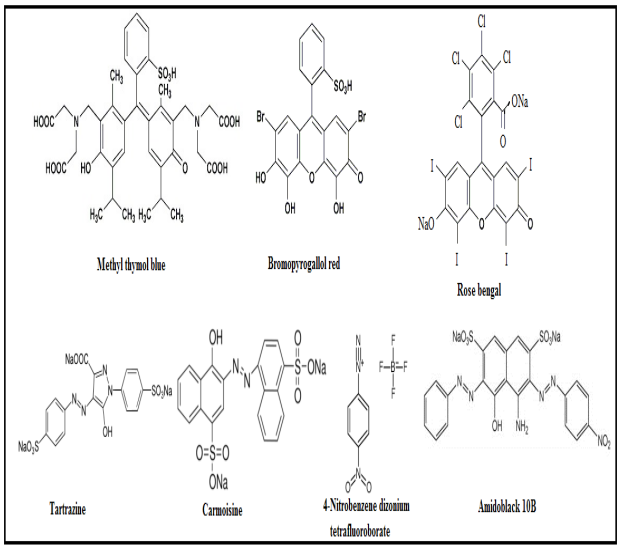

Figure 6. Structures of dyes: methyl thymol blue, bromopyrogallol red, rose bengal, tartrazine, carmoisine, 4-nitrobenzene dizonium tetrafluoroborate and amidoblack 10B.

thymol blue, bromopyrogallol red and 4-nitrobenzene dizonium tetrafluoroborate) was performed on three different stationary phases viz. (i) silica gel = S_1, (ii) Pani@SG-EB_1 = S_2 and (iii) Pani@SG-EB_1 = S_3 with thirteen different mobile phases of green solvent for obtaining a novel TLC system for the separation of dyes from their mixtures. Obtained results tabulated in Tables 3–7 and presented in Figures 5–9 are discussed below.

3.2 Silica gel (S_1) system

Using double distilled water (M_1), on pure silica static phase (S_1), binary separation of carmoisine (CS) from Tartrazine (TZ), rose Bengal (RB), amidoblack 10B (AB) and methyl thymol blue (MT) from the mixture of azo dyes has been observed while bromopyrogallol red (BG) and 4-nitrobenzene dizonium tetrafluoroborate (NT) are not detected.

With ethyl acetate (M_2) and n-butyl acetate (M_3) on S_1 static phase TZ, CS, AB, MT and BG organic dyes shows strong interaction with silica static phase all are shows at the point of application exhibiting R_F values 0.01 and RB dyes shows broad (R_F = 0.22-0.25) spot on both M_2 and M_3 mobile phases while NT dyes shows double spot on M2 and in case of M_3 mobile phase at point of application. Hence, none of the organic dyes can be well separated from their mixture.

In M_4 (Butane-1-ol) mobile phase the selective binary separation of RB (R_F = 0.75) from TZ, CS,

AB, MT, BG and NT (R_F = 0.01-0.12) on pure SG stationary phase.

In M_5-M_7 equal volume ratio (5:5) of two component mobile phase system using with the hope of better separation possibilities were used. In M_5 mobile phase TZ can be separated from CS, RB and AB dyes while MT and BG are tailed spot and NT having double spot. In M_6 binary separations were achieved (NT/TZ-CS-AB) while M_7 mobile phase (MT-BG/TZ-CS-RB-AB) occur.

With increasing volume ratio of organic solvent in DDW (M_8-M_{10}) in M_8 mobile phase TZ, CS, RB and AB (R_F = 0.82-0.87) exhibit high mobility and tailing in MT, BZ. In mobile phase M_9 and M_{10} consisting of TZ, CS, AB and MT shows strong interaction with silica gel static phase remain near the point of application (R_F = 0.01-0.09) while RB exhibit tailing spot and BG and NT dyes shows double spot, hence no separation were achieved.

In case of M_{11}-M_{13} mobile phase system on pure SG static phase the M_{11} mobile phase all spot near the point of application with broader range (R_F = 0.01-0.20) hence no good separation was achieved. In M_{12} mobile phase binary separation occur from TZ (R_F = 0.82) high mobility and CS, RB, AB and MT near the point of application (R_F = 0.02-0.25) while BG and NT not detected. With butanol:DDW ratio (4:6) v/v, in which M_{13} mobile phase occur binary separations occur TZ (R_F = 0.54), CS (R_F = 0.53) and AB (R_F = 0.48) exhibit high mobility and NT (R_F = 0.01) organic dyes remain the point of application as shown in **Table 3**.

3.3 Pani@SG-EB$_1$ (S_2) system

When pure double distilled water (M_1) is used as a mobile phase for examining migration behaviour of organic dyes on modified silica gel Pani@SG-EB$_1$, as stationary phase CS (R_F = 0.55) has high mobility, selected binary separation were occur TZ, RB, AB and MT remain at the point of application.

Using ethyl acetate (M_2) and n-butyl acetate (M_3) as the mobile phase on Pani@SG-EB$_1$) as stationary phase NT reach the maximum allowed distance (R_F = 0.91-0.92), while other near the point of application except RB which shows tailed spot binary separation achieved. In case of M_4 mobile phase RB (R_F = 0.77) separate out from all other organic dyes having low R_F values (RB/TZ-CS-AB-MT-BG-NT) binary separations were obtained with compact spots. Using M5 mobile phase all were found near the point of application except RB and NT. However RB produced tailed spot and NT was not detected.

With the use of equal volume ratio n-butyl acetate: DDW, (M_6) mobile phase on Pani@SG-

Table 3. Mobility of dyes in terms of R_F values on S_1 (silica gel) stationary phase with different mobile phases

Mobile Phase	R_F Value						
	TZ	CS	RB	AB	MT	BG	NT
M_1	0.18	0.55	0.01	0.04	0.04	ND	ND
M_2	0.01	0.01	0.22	0.01	0.01	0.01	0.10 and 0.94 DS
M_3	0.01	0.01	0.25	0.01	0.01	0.01	0.02
M_4	0.01	0.12	0.75	0.12	0.05	0.01	0.02
M_5	0.05	0.62	0.50	0.58	0.31T	0.32T	0.03 or 0.78 DS
M_6	0.94	0.82	0.35T	0.80	0.31T	0.38T	0.03
M_7	0.85	0.70	0.82	0.95	0.25	0.02	ND
M_8	0.87	0.83	0.85	0.82	0.41T	0.40T	0.03 or 0.63 DS
M_9	0.01	0.01	0.34T	0.01	0.01	0.02 or 0.86 DS	0.03 or 0.88 DS
M_{10}	0.01	0.03	0.31T	0.08	0.09	0.04	0.01 or 0.66 DS
M_{11}	0.18	0.20	0.19	0.19	0.18	0.20	0.01
M_{12}	0.82	0.10	0.25	0.02	0.12	ND	ND
M_{13}	0.54	0.53	0.35T	0.48	0.22	0.28	0.01

TZ, CS, RB, AB, MT, BG, and NT represent tartrazine, carmoisine, rose bengal, amidoblack 10B, methyl thymol blue, bromopyrogallol red and 4-nitrobenzene dizonium tetrafluoroborate respectively. DS, ND and T stand for double spot, not detected and tailed spots respectively.

T=tailed spot, (R_L - $R_T \geq 0.3$)

EB_1 stationary phase showed differential migration behaviour TZ (R_F = 0.95), CS (R_F = 0.70), RB (R_F = 0.40), AB (R_F = 0.78), MT (R_F = 0.06) BG (R_F = 0.22) and NT (R_F = 0.05) and hence this TLC system was considered most favourable for quaternary separations such as TZ-CS-RB-MT, TZ-CS-RB-NT and ternary separation RB-AB-MT and RB-AB-NT; good separation was obtained hence this mobile phase most efficient for the separation of these organic dyes (**Table 4**). This system was selected for further detailed studies.

On S_2 stationary phase, the mobility of RB dyes with mobile phases M_7 (R_F = 0.70) can be separated from CS, AB, MT and BG R_F (0.02, 0.10, 0.10 0.02 and 0.02 respectively), hence binary separation achieved while NT and TZ organic dyes was not detected.

When TLC plates were developed with M_8, M_9 mobile phases, with M_8 mobile phase all are found near the point of application (R_F = 0.01-0.11) except, RB tailing spot and NT, TZ were not detected on Pani@SG-EB_1 stationary phase. On M_9 binary separation (TZ-CS/MT) of these organic dyes achieved. And other dyes were not detected.

In M_{10}-M_{13} mobile phase with S_2 static phase with M_{10} mobile phase RB (R_F = 0.44) dyes separated from all other dyes which are near the point of application, thus binary separation was achieved. With mobile phase M_{11}, M_{12} and $M_{13,}$ some could not detected on the use of Pani@SG-B_1 and other remain at the point of application, thus no any separation was achieved; so this system was not favourable.

3.4 Pani@SG-EB_2 (S_3) system

On Pani@SG-EB_2 stationary phase using double distilled water (M_1) mobile binary separation of CS (R_F = 0.55) from TZ, RB, AB and MT their R_F = 0.18, 0.01, 0.04, 0.04 respectively while BG and NT were not detected.

With S_3 static phase with ethyl acetate (M_2) and n-butyl acetate (M_3) mobile phase NT organic dyes reach the maximum allowed distance, showed RF in the range of 0.91-0.92. Other organic dyes near the point of application except RB which showed tailed spot. Thus binary separation achieved (NT/TZ-CS-AB-MT-BG) in both mobile phase M_2 and M_3 as shown in **Table 5**.

RB (R_F = 0.70) exhibit high mobility and all organic dyes (TZ, CS, AB, MT, BG, NT) remain at the point of application (R_F = 0.01-0.10) as S_3 stationary phase. Binary separations of these organic dyes were achieved.

With equal volume of two component mobile

Table 4. Mobility of dyes in terms of R_F values on Pani@SG-EB_1 = S_2 stationary phase with different mobile phases

Mobile Phase	R_F Value						
	TZ	CS	RB	AB	MT	BG	NT
M_1	0.18	0.55	0.01	0.04	0.04	ND	ND
M_2	0.01	0.01	0.45T	0.01	0.01	0.01	0.92
M_3	0.01	0.01	0.46T	0.01	0.01	0.01	0.91
M_4	0.01	0.05	0.77	0.06	0.01	0.01	0.01
M_5	0.12	0.12	0.45T	0.01	0.05	0.02	ND
M_6	0.95	0.70	0.40	0.78	0.06	0.22	0.05
M_7	ND	0.10	0.70	0.10	0.02	0.01	ND
M_8	ND	0.10	0.40T	0.10	0.08	0.01	ND
M_9	0.36	0.30	ND	ND	0.01	ND	ND
M_{10}	0.02	0.10	0.44	0.10	0.03	0.02	0.01
M_{11}	0.17	0.10	ND	ND	ND	0.20	ND
M_{12}	ND	ND	ND	ND	0.08	ND	ND
M_{13}	0.13	0.21	ND	ND	0.05	ND	ND

TZ, CS, RB, AB, MT, BG, and NT represent tartrazine, carmoisine, rose bengal, amidoblack 10B, methyl thymol blue, bromopyrogallol red and 4-nitrobenzene dizonium tetrafluoroborate respectively. DS, ND and T stand for double spot, not detected and tailed spots respectively.

T = tailed spot, (R_L - $R_T \geq 0.3$)

phase ethyl acetate:DDW. In M_5 mobile phase TZ (R_F = 0.45) and CS (R_F = 0.40) can be separated from BG and NT dyes. In case of AB and MT lack of clarity of coloured spot and RB shows tailing spot.

In M_6 mobile phase TZ, CS and AB showed high mobility, their R_F values in the range of (0.75-0.93), other RB, MT and NT dyes show strong interaction with stationary phase so low R_F value detected, hence binary separations were achieved (TZ-CS-AB/RB-MT-NT) while BG dye not detected. On M_7 mobile phase binary separation occur (RB-AB-MT/TZ-BG-NT). CS showed broader and not clear spot.

With M_8 mobile phase of organic solvent, the analysis of organic dyes on Pani@SG-EB_2 stationary phase all are exhibited near the mid point of application, thus no any good separation was achieved due to broadness of spot. In case of M_9 mobile phase, the strong interaction occur between static phase and TZ, CS organic dyes. Hence, it shows high RF values near mid and above the mid point of application, hence mutual binary separation of these dyes TZ (R_F = 0.70), CS (R_F = 0.50), RB (R_F = 0.05), AB (R_F = 0.01) and NT (R_F = 0.02) while BG not detected.

RB and AB (R_F = 0.82-0.87) exhibit high mobility and tailing in MT, BZ. In mobile phase, M_9 and M_{10} consisting of TZ, CS, AB and MT showed strong interaction with silica gel static phase remained near the point of application (R_F = 0.01-0.09), while RB exhibit tailing spot along with BG and NT dyes showed double spot. Hence, no separation was achieved.

In case of M_{10} mobile phase system on S_3, none of the analyte move along the mobile phase all organic dyes remained near the point of application (R_F = 0.01-0.10). Hence, no separation was found. While in M_{11} mobile phase, mutual binary separation was achieved (TZ-CS-AB/NT) on S_3 static phase while RB showed tailed spot and MT broader spot not compact. In M_{12} mobile phase RB, MT, BG and NT (R_F = 0.01-0.05) at the point of application and other not detected in this case no separation occur while M13 mobile phase TZ, CS, AB, RB and MT shows broader spot near the point of application and other organic dyes BG, NT were not detected, thus no good separation could be achieved hence mobile system M_{12} and M_{13} are not suitable for separation of dyes as shown in **Table 5**.

An important quaternary and ternary separation mixture of organic dyes consisting of Tartrazine (R_F =0.95), carmoisine (R_F = 0.70), rose Bengal (R_F = 0.40), amidoblack 10B (R_F = 0.78), methyl thymol blue (R_F = 0.06), bromopyrogallol red (R_F = 0.22) and 4-nitrobenzene dizonium tetrafluoroborate (R_F

Table 5. Mobility of dyes in terms of R_F values on Pani@SG-EB_2 stationary phase with different mobile phases

Mobile Phase	R_F Value						
	TZ	**CS**	**RB**	**AB**	**MT**	**BG**	**NT**
M_1	0.18	0.55	0.01	0.04	0.04	ND	ND
M_2	0.01	0.01	0.40T	0.01	0.01	0.01	0.91
M_3	0.01	0.01	0.45T	0.01	0.01	0.01	0.90
M_4	0.01	0.10	0.70	0.10	0.01	0.01	0.02
M_5	0.45	0.40	0.55T	0.22	0.12	0.05	0.02
M_6	0.93	0.75	0.15	0.80	0.25	ND	0.02
M_7	0.13	0.21	0.60	0.43	0.53	0.02	0.02
M_8	0.60	0.57	0.76	0.45	0.60	0.38	0.03 or 0.76 DS
M_9	0.70	0.50	0.05	0.01	0.40T	ND	0.02
M_{10}	0.07	0.06	0.10	0.06	0.10	0.01	0.01
M_{11}	0.42	0.41	0.55T	0.34	0.20	ND	0.02
M_{12}	ND	ND	0.05	ND	0.01	0.05	0.01
M_{13}	0.26	0.25	0.25	0.17	0.10	ND	ND

TZ, CS, RB, AB, MT, BG, and NT represent tartrazine, carmoisine, rose bengal, amidoblack 10B, methyl thymol blue, bromopyrogallol red and 4-nitrobenzene dizonium tetrafluoroborate respectively. DS, ND and T stand for double spot, not detected and tailed spots respectively.

T = tailed spot, (R_L - $R_T \geq 0.3$)

= 0.05) has been achieved on S_2 with M_6 (**Figure 7**). Hence, TLC system comprising of Pani@SG-EB_1 as stationary phase and [n-butyl acetate:DDW, 5:5] (M_6) as mobile phase has been most favourable for resolution of multi-component mixtures of organic dyes (two-three or four component mixtures).

3.5 Effect of modification of silica gel with polyaniline as a stationary phase

Silica gel was replaced by modified silica gel with the hope of getting improved separations. It was observed that in case of silica gel, separations of rose Bengal, methyl thymol blue and bromopyrogallol red was not obtained with silica gel due to tailing of spots. The chromatographic performance of the stationary phases was in the order: Pani@SG-EB_1 > Pani@SG-EB_2> silica gel. Thus, better performance of Pani@SG-EB_1 as stationary phase is probably due to its large surface area as compared to other stationary phases.

3.6 Aging effect of mobile phase

Stability (aging effect) of mobile phase M_6 on the separation was insignificant since slight variation in their R_F values was observed during the separation of organic dyes from their quaternary mixture with the use of freshly prepared mobile phase and the use of the same mobile phase after storing it to 24 h. Hence, it can be concluded that the composition of eluent M_6 remains unaltered for several hours and suitable for chromatographic analysis.

3.7 Effect of foreign substances

Effect of metal cations, anions on the magnitude of separation factor (α) and resolution parameter (Rs) and ΔR_F values for separation of four-component mixtures consisting of tartrazine, carmoisine, rose bengal and methyl thymol blue has been examined and the results are presented in **Table 6**. From the results, it is clear that magnitude of these parameters is marginally influenced (increases or decreases) in the presence of these foreign substances, but separation was always possible in each case. The minor change in the value of these parameters was due to the slight increase in spot size of the analyte because of certain interactions of organic dyes with these foreign substances.

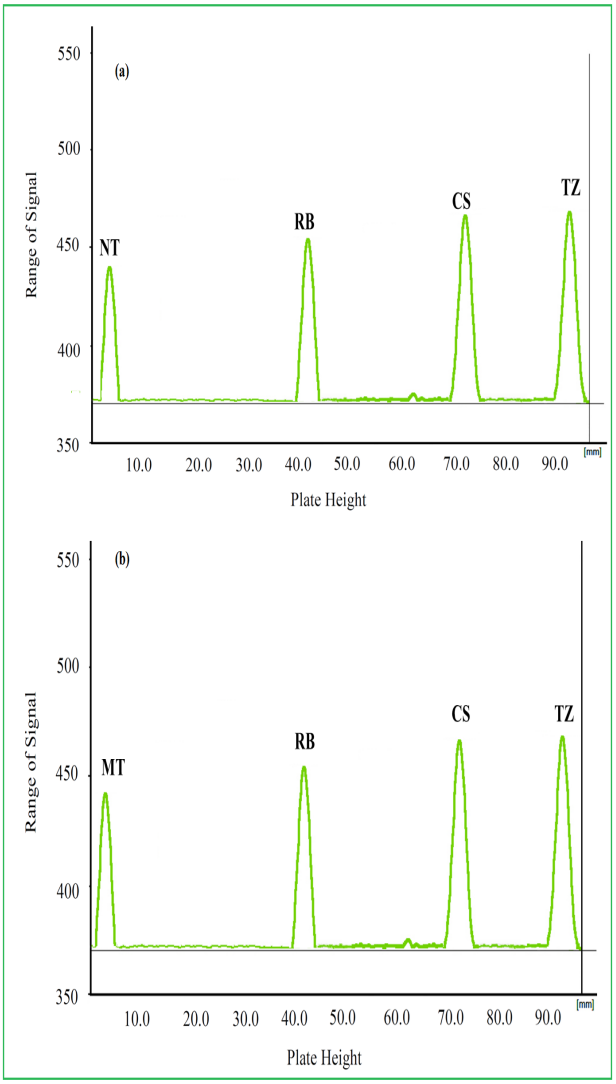

Figure7. Densitographic presentation of representative separations of four- component mixtures of dyes achieved with M_6 mobile phase on S_2 stationary phase (a) (NT-RB-CS-TZ) and (b) (MT-RB-CS-TZ).

3.8 Limits of detection

The lowest possible detectable amounts (µg $spot^{-1}$) of rose bengal (1.0), amidoblack 10B (1.3), carmoisine (0.75), tartrazine (1.0), methyl thymol blue (1.25), bromopyrogallol red (0.90) and 4-nitrobenzene dizonium tetrafluoroborate (1.0) showing reasonable sensitivity of the proposed method for on spot detection of these organic dyes of different concentrations on the Pani@SG-EB_1. TLC plates which were developed with the selected mobile phase M_6 and the spots were visualized. This process was repeated by successive reduction of the concentration of organic dyes until the detection of organic dyes was not possible anymore.

4. Applications

The proposed thin layer chromatographic method, comprising of polyaniline modified silica gel Pani@SG-EB_1 as stationary phase and aqueous M_6 (n-butyl acetate:DDW, 5:5) by volume as mobile phase, is applicable for the identification of carmoisine in Solvin cold DS syrup and tartrazine in Mefast™ P syrup (**Table 7** and **Figures 8–9**).

5. Conclusions

It may also be concluded from this work that the use of thin layer chromatographic system consisting of polyaniline modified silica gel as stationary phase with aqueous M_6 (n-butyl acetate:DDW, 5:5) as eco-friendly mobile phase is most favourable for the identification and separation of four-component mixtures of rose bengal, tartrazine, carmoisine,

Table 6. Effect of interference on ΔR_F, separation (α) and resolution (R_S) factors of the separated ternary mixtures of amino acids

Foreign Substance	Quaternary Separations								
	Tartrazine (TZ), Carmoisine (CS), Rose bengal (RB) and Methyl thymol blue (MT)								
	TZ and CS			CS and RB			RB and MT		
	ΔR_F	α	R_S	ΔR_F	α	R_S	ΔR_F	α	R_S
	(0.23)	(6.394)	(65.74)	(0.31)	(3.676)	(56.363)	(0.34)	(10.444)	(56.666)
Cations									
Cu^{2+}	0.23	5.693	51.111	0.31	3.649	47.692	0.34	12.148	48.571
Zn^{2+}	0.22	6.091	55.00	0.32	3.858	53.333	0.34	10.444	52.307
Mn^{2+}	0.17	3.552	37.777	0.32	3.928	53.333	0.35	9.626	53.846
Ni^{+}	0.21	6.674	46.666	0.35	4.452	46.666	0.31	7.352	36.470
Li^{+}	0.21	5.793	46.666	0.32	3.891	45.714	0.35	10.886	46.666
Mg^{2+}	0.21	5.165	46.666	0.33	4.022	50.769	0.32	8.494	45.714
Anions									
CO_3^{2-}	0.21	5.165	46.666	0.31	3.701	47.692	0.35	10.886	46.666
NO_3^{-}	0.22	7.026	44.00	0.30	3.583	42.857	0.35	8.679	46.666
Br^{-}	0.21	5.793	60.00	0.30	3.583	50.00	0.34	7.639	42.50
Cl^{-}	0.18	4.428	36.00	0.34	4.317	48.571	0.34	9.232	42.50
CH_2COO^{-}	0.20	6.332	40.00	0.36	4.692	51.428	0.32	8.494	45.714

Table 7. Identification of carmoisine (in Solvin cold DS syrup) and tartrazine (in Mefast™ P syrup) according to their R_F values

Organic Dyes	R_F Value	
	Standard Sample	Drug Sample
Carmoisine	0.70	0.67
Tartrazine	0.95	0.90

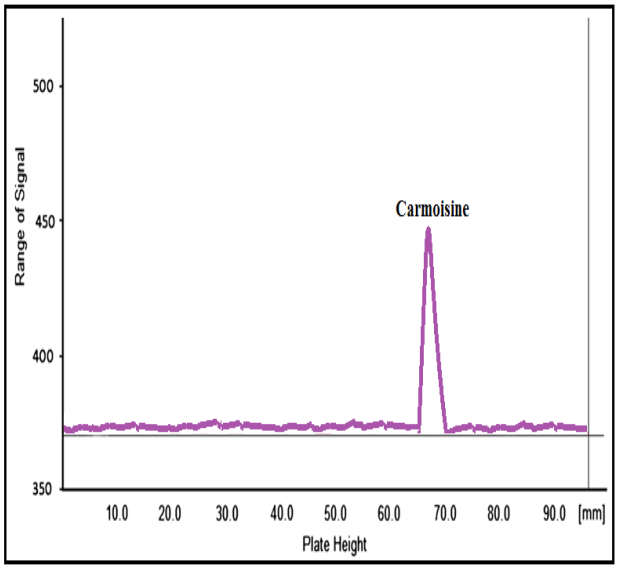

Figure 8. Densitographic illustration of identification of carmoisine in Solvin cold DS syrup on S_2 with M_6.

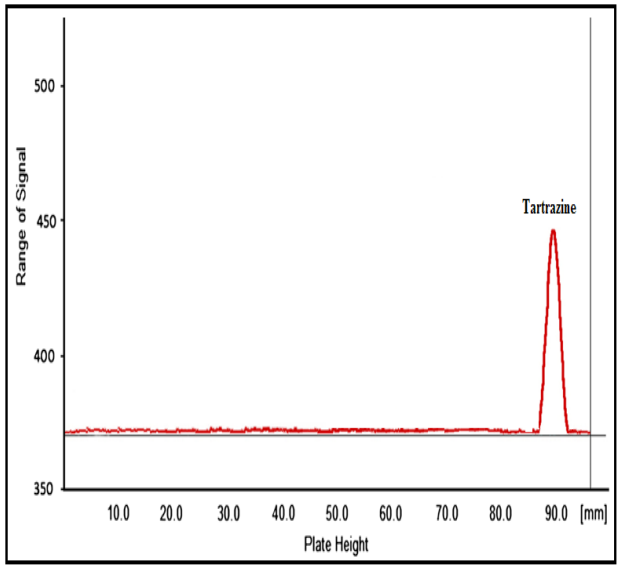

Figure 9. Densitographic illustration of identification of Tartrazine in Mefast™ P syrup on S_2 with M_6.

methyl thymol blue or 4-nitrobenzene dizonium tetrafluoroborate. The chosen TLC system is also applicable for the identification of these food dyes in pharmaceutical products (Solvin cold DS syrup and Mefast™ P syrup). The use of aqueous solutions of n-butyl acetate as green mobile phase system makes the proposed TLC system as environment friendly and paves the way for the development of green chromatography.

Conflict of interest

The authors declare that they have no conflict of interest.

References

1. Aberoumand A. A review article on edible pigments properties and sources as natural biocolorants in foodstuff and food industry. World Journal of Dairy & Food Sciences 2011; 6: 71–78.
2. Huang D, Ou B, Prior RL. Journal of Agricultural and Food Chemistry 2005; 53: 1841–1856.
3. Hajimahmoodi M, Afsharimanesh M, Moghaddam G, *et al.* Determination of eight synthetic dyes in foodstuffs by green liquid chromatography. Food Additives & Contaminants: Part A 2013; 30: 780–785.
4. Alves SP, Brum DM, de Andrade e CM, *et al.* Determination of Synthetic Dyes in Selected Foodstuffs by High Performance Liquid Chromatography with UV-DAD Detection. Food Chemistry 2008; 107: 489–496.
5. Llamas NE, Garrido M, Di Nezio MS, *et al.* Second order advantage in the determination of amaranth, sunset yellow FCF and tartrazine by UV–vis and multivariate curve resolution-alternating least squares. Analytica Chimica Acta 2009; 655: 38–42.
6. Larsen JC. Legal and illegal colours. Trends in Food Science & Technology 2008; 19: S64–S69.
7. Nevado J, Flores JR, Llerena MJV. Adsoptive stripping voltammetry of Tartrazine at the hanging mercury drop electrode in soft drinks. Fresenius' Journal of Analytical Chemistry 1997; 357: 989–994.
8. Silva MLS, Garcia MBQ, Lima JL, *et al.* Voltammetric determination of food colorants using a polyallylamine modified tubular electrode in a multicommutated flow system. Talanta 2007; 72: 282–288.
9. Amini M, Arami M, Mahmoodi NM, *et al.* Dye removal from colored textile wastewater using acrylic grafted nanomembrane. Desalination 2011; 267: 107–113.
10. Harrelkas F, Azizi A, Yaacoubi A, *et al.* Treatment of textile dye effluents using coagulation–flocculation coupled with membrane processes or adsorption on powdered activated carbon. Desalination 2009; 235: 330–339.
11. Chen AH, Chen SM. Biosorption of azo dyes from aqueous solution by glutaraldehyde-crosslinked chitosans. Journal of Hazardous Materials 2009; 172: 1111–1121.
12. Charumathi D, Das N. Packed bed column studies for the removal of synthetic dyes from textile wastewater using immobilised dead C. tropicalis. Desalination 2012; 285: 22–30.
13. Ma M, Luo X, Chen B, *et al.* Simultaneous determination of water-soluble and fat-soluble synthetic colorants in foodstuff by high-performance liquid chromatography–diode array detection–electrospray mass spectrometry. Journal of Chromatography A 2006; 1103: 170–176.
14. Vachirapatama V, Mahajaroensiri J, Visessanguan W. Identification and determination of seven synthetic dyes in foodstuffs and soft drinks on monolithic C18 column by high performance liquid chromatography. Journal of Food and Drug Analysis 2008; 16: 77–82.
15. Young ML. Rapid identification of color additives, using the C18 cartridge: Collaborative study. Journal of Association of Official Analytical Chemists 1988; 71: 458–461.
16. Steele JA. High performance thin layer chromatographic identification of synthetic food dyes in alcoholic products. Journal of Association of Official Analytical Chemists 1984; 67: 540–541.
17. Oka H, Ikai Y, Kawamura N, *et al.* Simple method for the analysis of food dyes on reversed-phase thin-layer plates. Journal of Chromatography 1987; 411: 437–444.
18. Horwitz W, Chichilo P, Reynolds H. Official Methods of Analysis of the Association of

Official Analytical Chemists. Washington, DC, USA: Association of Official Analytical Chemists; 1970.
19. Fogg AG, Summan AM. Differential-pulse polarographic monitoring of permitted synthetic food colouring matters and ascorbic acid in accelerated light degradation studies and the spectrophotometric determination of the ammonia and simpler amines formed. Analyst 1983; 108: 691–700.
20. Ni Y, Bai J, Jin L. Simultaneous adsorptive voltammetric analysis of mixed colorants by multivariate calibration approach. Analytica Chimica Acta 1996; 329: 65–72.
21. Combeau S, Chatelut M, Vittori O. Identification and simultaneous determination of Azorubin, Allura red and Ponceau 4R by differential pulse polarography: application to soft drinks. Talanta 2002; 56: 115–122.
22. Graichen C. Quantitative determination of FD&C colors in foods. Journal of Association of Official Analytical Chemists 1975; 58: 278–282.
23. Vidotti EC, Cancino JC, Oliveira CC, *et al.* Simultaneous determination of food dyes by first derivative spectrophotometry with sorption onto polyurethane foam. Analytical Sciences 2005; 21: 149–153.
24. Yang Y, Yin J, Shao B. Simultaneous determination of five aluminum lake dyes in chewing gum by HPLC with photodiode array detection. Food Additives & Contaminants: Part A 2011; 28: 1159–1167.
25. Sun S, Wang Y, Yu W, *et al.* Determination of sudan dyes in red wine and fruit juice using ionic liquid-based liquid–liquid microextraction and high-performance liquid chromatography. Journal of Separation Science 2011; 34: 1730–1737.
26. Liu R, Hei W, He P, *et al.* Simultaneous determination of fifteen illegal dyes in animal feeds and poultry products by ultra-high performance liquid chromatography tandem mass spectrometry. Journal of Chromatography B 2011; 879: 2416–2422.
27. Huang HY, Shih YC, Chen YC. Determining eight colorants in milk beverages by capillary electrophoresis. Journal of Chromatography A 2002; 959: 317–325.
28. Ishikawa R, Oishi M, Kimura K, *et al.* Determination of synthetic food dyes in food by capillary electrophoresis. Journal of the Food Hygienic Society of Japan 2004; 45: 150–155.
29. Prado MA, Boas LFV, Bronze MR, *et al.* Validation of methodology for simultaneous determination of synthetic dyes in alcoholic beverages by capillary electrophoresis. Journal of Chromatography A 2006; 1136: 231–236.
30. Chen Q, Mou S, Hou X, *et al.* Determination of eight synthetic food colorants in drinks by high-performance ion chromatography. Journal of Chromatography A 1998; 827: 73–81.
31. Tesic Z, Opsenica DM. Inorganic ion exchangers in paper and thin-layerchromatographic separations. In: Inamuddin, Luqman M (editors). chapter 15, Ion Exchange Technology II: Application, Springer Netherlands. Springer Netherlands; 2012. p. 365–389.
32. Dhote SS, Deshmukh L, Paliwal L. Heavy metal ions separation on thin layer of impregnated carbamideformaldehyde polymer. Journal of Chromatography & Separation Techniques 2012; 3(2): 1–3.
33. Soponar F, Moţ AV, Sarbu C. Quantitative determination of some food dyes using digital processing of images obtained by thin-layer chromatography. Journal of Chromatography A 2008; 1188: 295–300.
34. Mohammad A, Inamuddin, Siddiq A, *et al.* Green solvents in thin-layer chromatography. In: Mohammad A, Inamuddin (editios). Green Solvents I. Springer, Dordrecht; 2012. p. 331–361.
35. Huang S, Xiao Q, Li R, *et al.* A simple and sensitive method for L-cysteine detection based on the fluorescence intensity increment of quantum dots. Analytica Chimica Acta 2009; 645: 73–78.
36. Ge H, Wallace GG. High-performance liquid chromatography on polypyrrole-modified silica. Journal of Chromatography A 1991; 588: 25–31.
37. Behera D, Satapathy H, Bhanthia AK. Synthesis, purification and curing properties of vinyl ester network. Pigment & Resin Technology

2006; 35: 319–325.
38. Kamistos EI, Patsis AP, Kordas G. Infrared-reflectance spectra of heat-treated sol-gel-derived silica. Physical Review B 1993; 48: 12499.
39. Wood DL, Rabinovich EM. Study of alkoxide silica gels by infrared spectroscopy. Applied Spectroscopy 1989; 43: 263–267.
40. Ansari MO, Yadav SK, Cho JW, *et al.* Thermal stability in terms of DC electrical conductivity retention and the efficacy of mixing technique in the preparation of nanocomposites of graphene/polyaniline over the carbon nanotubes/polyaniline. Composites Part B: Engineering 2013; 47: 155–161.
41. Ansari MO, Mohammad F. Thermal stability of HCl-doped-polyaniline and TiO_2 nanoparticles-based nanocomposites. Journal of Applied Polymer Science 2012; 124: 4433–4442.
42. Shan Y, Gao L. Synthesis, characterization and optical properties of CdS nanoparticles confined in SBA-15. Materials Chemistry and Physics 2005; 89: 412–416.
43. Yu MR, Suyambrakasam G, Wu RJ, *et al.* Preparation of organic–inorganic (SWCNT/TWEEN–TEOS) nano hybrids and their NO gas sensing properties. Sensors and Actuators B: Chemical 2012; 161: 938–947.
44. Zheng C, Chen W, Ye X. Study on Au nanoparticles, TiO_2 nanoclusters, and SiO_2 nanoshells coated multi-wall carbon nanotubes/silica gel-glass. Optical Materials 2012; 34: 1042–1047.
45. Goren M, Qi Z, Lennox RB. Selective templated growth of polypyrrole strands on lipid tubule edges. Chemistry of Materials 2000; 12: 1222–1228.
46. Guo J, Gu H, Wei H, *et al.* Magnetite–polypyrrole metacomposites: Dielectric properties and magnetoresistance behavior. The Journal of Physical Chemistry 2013; 117: 10191–10202.
47. Wu CM, Lin SY, Chen HL. Structure of a monolithic silica aerogel prepared from a short-chain ionic liquid. Microporous and Mesoporous Materials 2012; 156: 189–195.
48. Chen M, Du C, Wang L, *et al.* Silicon/graphite/polyaniline nanocomposite with improved lithium-storage capacity and cyclability as anode materials for lithium-ion batteries. International Journal of Electrochemical Science 2012; 7: 819–829.
49. Mohammad A, Mobin R. Resolution of a three-component mixture of methyl group substituted cationic surfactants by use of a green eluent: A thin-layer chromatographic approach. Journal of Planar Chromatography – Modern TLC 2015; 28: 17–23.
50. Shimada T, Aoki K, Shinoda Y, *et al.* Functionalization on silica gel with allylsilanes: A new method of covalent attachment of organic functional groups on silica gel. Journal of the American Chemical Society 2003; 125: 4688–4689.
51. Ahmad S, Sultan A, Raza W, *et al.* Boron nitride based polyaniline nanocomposite: Preparation, property, and application. Journal of Applied Polymer Science 2016; 133.

Applied Chemical Engineering

Focus and Scope

Applied Chemical Engineering (ACE) is an international open-access academic journal dedicated to publishing highly professional research in all fields related to chemical engineering. All manuscripts are subjected to a rigorous double-blind peer review process, to ensure quality and originality. We are interested in original research discoveries. This journal also features a wide range of research in ancillary areas relevant to chemistry.

ACE publishes original research articles, review articles, editorials, case reports, letters, brief commentaries, perspectives, methods, etc.

The research topics of ACE include but are not limited to:

1. Analytical chemistry
2. Chemical engineering
3. Materials chemistry
4. Material synthesis
5. Catalysis
6. Process chemistry and technology
7. Quantum chemistry method
8. Environmental chemical engineering
9. Bio-energy, resources, pollution
10. Reaction kinetics
11. Nanotechnology and bioreactors
12. Surface, coating and film

EnPress Publisher, LLC

EnPress Publisher, LLC, is a scholastic conduit for an assembly of professionals in the domains of science, technology, medicine, engineering, education, social sciences, and many more, as a round table for their intellectual discourse and presentation, and as an instrument to galvanize research designs, policy implementation, and commercial interests, to facilitate the prevailing over their challenges and to encourage to the full advantage of their resources and true potential.

We are the intellectual and academic home for academics, educators, scholars, clinicians, corporate researchers, who all play important roles in a wide range of national and international research organizations, and whose interests, expertise, research approaches, and industry objectives from around the world coalesce together to advance significant contributions in their research and professional fields.

As an instrument of information purveyor, we seek to combine academic rigor and originality with the nuanced development of policy and practice. Via our journals, client database, online campaigns, and social media presence, we offer a platform for industry professionals to interconnect, as well as opening doors towards cost-effective solutions for them to succeed, and we confidently hope to inspire a new generation of multidisciplinary researchers, think-tank experts, policymakers and business entities to innovate and advance their knowledge across fields.

EnPress Publisher, LLC

Add: 14701 Myford Road, Suite B-1, Tustin, CA 92780, United States

Tel: +1 (949) 299 0192

Email: contact@enpress-publisher.com

Web: https://enpress-publisher.com